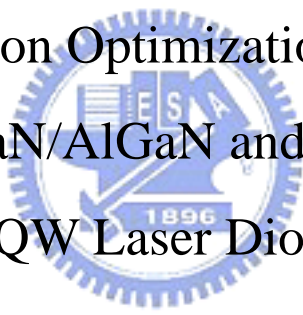# 國 立 交 通 大 學
光 電 工 程 研 究 所

碩士論文

GaN/AlGaN 和 InGaN/AlInGaN 多量子井雷射二極體
之模擬最佳化主動層研究

Numerical Study on Optimization of Active Layer
Structures for GaN/AlGaN and InGaN/AlInGaN
MQW Laser Diodes

研究生：蘇柏源

指導教授：郭浩中 教授

盧廷昌 教授

中 華 民 國 九 十 七 年 六 月

GaN/AlGaN 和 InGaN/AlInGaN 多量子井雷射二極體

之模擬最佳化主動層研究

Numerical Study on Optimization of Active Layer Structures for
GaN/AlGaN and InGaN/AlInGaN MQW Laser Diodes

研究生: 蘇柏源　　　　　　　Student: Po-Yuan Su

指導教授: 郭浩中 教授　　　　Advisor: Prof. Hao-Chung Kuo

　　　　　盧廷昌 教授　　　　　　　　Prof. Tien-Chang Lu

國 立 交 通 大 學
光電工程研究所
碩 士 論 文

A Thesis
Submitted to Institute of Electro-Optical Engineering
College of Electrical Engineering
National Chiao Tung University
in Partial Fulfillment of the Requirements
for the Degree of
Master
In
Electro-Optical Engineering

July 2008
Hsinchu, Taiwan, Republic of China

GaN/AlGaN 和 InGaN/AlInGaN 多量子井雷射二極體

之模擬最佳化主動層研究

研究生：蘇柏源　　　　　　　　　　　指導教授: 郭浩中教授

　　　　　　　　　　　　　　　　　　　　　　　盧廷昌教授

國立交通大學光電工程研究所碩士班

摘要

　　本論文中，我們以理論模擬的方式探討紫外光氮化鎵/氮化鋁鎵半導體雷射的多重量子井主動層結構最佳設計分析以得到較小的臨界電流，並且討論其內部的元件物理機制。在模擬中，我們使用由加拿大Crosslight公司所發表的Lastip商用模擬軟體進行探討。模擬結果發現，當量子井個數是兩個或三個時且位障層使用鋁含量約在10~12%左右可以得到較小的臨界電流。形成最佳化結構的物理機制主要歸因於幾個不同的因素，包括電子溢流、載子分布不均、極化電荷造成的內建電場、以及光場侷限能力。我們研究量子井個數以及在位障層中不同的鋁含量對雷射特性的影響，這些元件內部的物理機制是需要被研究及了解，才能進一步設計出最佳化元件結構。

　　再者，我們也利用此模擬軟體來探究在氮化銦鎵雷射中氮化鋁鎵銦使用於位障層來消除 quantum-confined Stark effect (QCSE)。模擬結果發現，此四元材料的使用可以消除QCSE並且改善雷射的特性。由於四元材料可以經由不同鋁和銦的含量而具有不同組成。因此，我們也針對不同組成的氮化鋁鎵銦材料做最佳化理論分析並且討論其內部的物理機制。模擬結果顯示，氮化銦鎵/氮化鋁鎵銦雷射在位障層的鋁含量是15%及銦含量是18.8%時，會有最佳的主動層結構。同時，我們也討論了影響此元件效能的機制，分別是電子溢流、載子侷限、以及光場侷限的問題。

Numerical Study on Optimization of Active Layer Structures for GaN/AlGaN and InGaN/AlInGaN MQW Laser Diodes

Student : Po-Yuan Su

Advisor: Prof. Hao-Chung Kuo

Prof. Tien-Chang Lu

Institute of Electro-Optical Engineering

National Chiao Tung University

Abstract

In this thesis, theoretical analysis for different active layer structures is performed to minimize the laser threshold current of the ultraviolet GaN/AlGaN multiple-quantum-well laser diodes by using the LASTIP simulation program developed by Crosslight. The simulation results show that the lower threshold current can be obtained when the number of quantum wells is two or three and the aluminum compositions in barrier layer is about 10~12%. This optimal structure is attributed to several different effects including electron leakage current, non-uniform carrier distribution, interface charge density induced by spontaneous and piezoelectric polarization, and optical confinement factor. These internal physical mechanisms are investigated by theoretical calculation to analyze the effects of quantum-well number and different aluminum compositions in barrier layer on laser threshold properties. These internal physical mechanisms should be investigated and understood to obtain the optimal device structure.

Furthermore, we also perform the theoretical simulation to study the elimination of quantum-confined Stark effect (QCSE) on the InGaN/InGaN and InGaN/AlInGaN multiple-quantum-well (MQW) laser performance. The simulation results illustrate that the quaternary alloys used in the quantum-barrier layer can eliminate the QCSE indeed and also improve the performance of the laser diodes. Since different quaternary alloys can be obtained by varying aluminum and indium compositions, we optimize the quaternary AlInGaN barrier layer and investigate the internal physical mechanisms in this study. The InGaN/AlInGaN laser diodes with an active layer of $x = 0.15$ and $y = 0.188$ in the $Al_xIn_yGa_{1-x-y}N$ barrier layer will be the optimized active layer structure due to the competition between three internal physical mechanisms, including the severe electron leakage current, carrier confinement in the quantum well, and optical confinement factor.
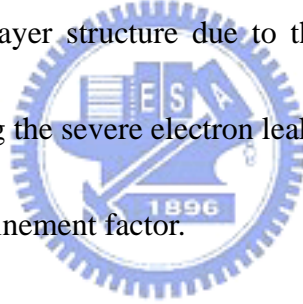
致謝

　　兩年的時間說長不長說短不短，猶記得兩年前才剛加入到半導體雷射實驗室這個大家庭，轉眼間就要從這裡畢業離開。在這裡的兩年內，很感謝實驗室的三位指導老師：王興宗老師、郭浩中老師以及盧廷昌老師，因為有他們的指導使得我可以帶著滿滿的知識去面對未來的挑戰，不只在專業上，在為人處事方面也是同樣的滿載而歸。王老師是個非常有專業素養的學者，時常給予學生具正面性的意見，郭老師是個會照顧學生、替學生未來著想規劃的好老師，盧老師是個年輕有為、具教學熱忱的好老師。有他們指導的實驗室，相信未來會有更好的發展。

　　謝謝俊榮學長，在這兩年內不吝嗇的傾囊相授，使得我在模擬半導體光電元件上得以順利的進行研究，在生活上也是亦師亦友的好伙伴，真的很開心在碩士班生活裡可以遇到這樣一位好學長。謝謝宗憲學長，在我遇到低潮的時候會抽空陪我聊天，儘管現在學長出國了，還是會在網路上關心了解我們的生活，當然在此也祝福學長可以快點學成歸國，能在自己的事業上有一番大的成就。同時也感謝其他博士班學長：小朱、清華、士偉、明華、碩均、輝閔、禮榮等，在 meeting 上的仔細聆聽並給予建議。也感謝已經畢業的家璞及瑞農學長和潤琪學姊陪我度過了碩一的時光，有你們在的實驗室充滿了活力與歡笑。

　　謝謝實驗室的好戰友，伯駿、晁恩、家銘、小恬恬、小麥、子維、承恩、恕帆、士嘉及建達，謝謝你們在這兩年內不吝嗇學業上的討論，我才能完成碩士班的學位。伯駿是個害羞純情的男生，在碩班兩年逐漸的可以看的到他的改變，晁恩是個愛家的男孩，常常回家陪父母吃飯，家銘是個能動能靜的人，跟你一起打球看球真的很開心，還有介紹新竹的美食真的很美味，小恬恬是個很可愛的女生，祝妳工作一切順利、賺大錢。

謝謝實驗室的學弟妹，尚樺、啄木、梅子還有 250 的學弟妹，實驗室有你們的加入，想必會有更好的研究成果，尚樺，祝你出國一切順利，能璺到你想要的知識；啄木，祝你實驗能順順利利，有空在一起打球；梅子，祝你天天能像現在這麼開心，身體健康。

謝謝我的女朋友 Wenny，在這碩士兩年及大學的陪伴以及扶持，在我低潮的時候幫我加油打氣，使我得以有充足的動力完成碩士學位。同時也祝福所有認識我的人都能平安喜樂。最後，謝謝我的家人，爸爸、媽媽以及妹妹，你們是我成長茁壯最大的原動力，在此僅以本篇論文獻給你們。

Contents

List of Figures

List of Tables

Chapter 1 Introduction

Recently, the energy issues and green house effect have been extensively discussed in the whole world. Undoubtedly, these problems must be investigated and solved immediately. For this reason, scientists have researched into the improvement in reduction of energy consumption and CO_2 pollution. On the basis, optoelectronic semiconductor devices, which include solar cells, light-emitting diodes (LEDs), laser diodes (LDs), photodiodes and so on, have received great attractions. Solar cells cause great attention because they can convert the incident sunlight into a useful form of energy. LEDs have been widely used to replace the traditional traffic lights and full-color displays to reduce power consumption. Besides, LEDs also have another application to lighting technology. They will become the mainstream in homes, offices, and public places in the future years. LDs are fascinating due to their coherency and small divergent angle which make them be used in the applications from the writing or readout sources compacts disk players to the light sources in optical fiber communication systems. Moreover, LDs and LEDs can also emit ultraviolet and infrared wavelength. Ultraviolet light emitters can be used in biochemical technology, efficient white lighting, and high-density optical data storage, etc. Infrared light emitters with the emission wavelength of 1.3 μm and 1.5 μm can be used in communication system. The above-mentioned advantages are the reason that researchers aspire to investigate into

optoelectronic semiconductor devices.

As for the development of LDs, semiconductors lasers were successfully demonstrated by several groups in 1962 [1]-[4]. First, a forward-biased gallium arsenide (GaAs) p-n junction was announced and the optical gain was provided by the recombination of electrons and holes in the depletion region of the p-n junction. It was so called gain media in laser theory. Second, the polished facets perpendicular to the junction plane forming a resonant cavity provided the optical feedback. A lot of direct-bandgap materials, such as indium phosphide (InP), indium arsenide (InAs), gallium arsenide phosphide (GaAsP), gallium indium arsenide (GaInAs), and indium arsenide phoside (InAsP) were used to produce semiconductor lasers for the purpose of attaining various wavelength. Nevertheless, these earlier devices performed higher threshold current density ($J_{th} \geqq 50kA/cm^2$) with using p-n junction. In order to reduce the higher threshold current, a new technology called double heterostructure (DH) was introduced. This kind of structure was also called p-i-n structure. A double heterostructure laser consisted of an active layer embedded in two higher bandgap cladding layers. Therefore, the electrons and the holes were able to be well confined in the active region and enhance the recombination possibility of the electrons and the holes at the same time. Moreover, a cladding layer had a lower index of refraction than that of an active layer, which formed an optical waveguide. Hence, a DH laser confined the carriers and photons in the same range simultaneously, which enhanced the rate of stimulated emission.

The first room-temperature operation of a heterostructure laser (GaAs/$Al_xGa_{1-x}As$) was demonstrated by Kressel [5], Hayashi [6], Alferov [7],etc. with the technique of liquid-phase epitaxial (LPE) in 1969. By 1975, the threshold current density of the laser diodes used 0.1 mm thin active layers had been reduced to a half of the magnitude over the first-made simple homostructure lasers in 1962.

As the active region was getting thinner about to nanometer order, the electrons were confined to a small region of space, and it produced discrete energy levels instead of a continuum according to quantum theory. Under this circumstance, the density of state (DOS) in conduction and valence band was able to be diminished, which made the threshold current for the population inversion effectively reduce as compared with DH lasers. This kind of semiconductor lasers was also called quantum-well (QW) lasers. The application of quantum effect in LDs was first generated in the early 1970s, and after that, the QW structures in the active region have been utilized by semiconductor lasers such as LDs, vertical-cavity surface-emitting lasers (VCSELs), and distributed feedback (DFB) lasers until now.

In addition to the structure, the materials used in the semiconductor devices are hot issues to be investigated. Basically, most optoelectronic devices are typically made from Ⅲ-Ⅴ compound semiconductors due to their direct bandgap characteristics. In the early stage, many researchers investigated Ⅲ-Ⅴ compound materials in GaAsP, GaInAs, and InAsP, etc,

and recently, they have focused on nitride based materials because of the wide bandgap of these materials. Moreover, a historical review of the development of Ⅲ-nitride LEDs and LDs, and some important parameters such as the bandgap energy, band-offset ratios, refractive indices of Ⅲ-nitride alloys will be mentioned and summarized in the following sub-sections

1.1   Introduction to Nitride Based Materials

The bandgap energy of Ⅲ-nitride materials, including indium nitride (InN), gallium, nitride (GaN), and aluminum nitride (AlN), can be divided into 0.78 eV, 3.50 eV, and 6.28 eV, respectively.[8] The bandgap types of the Ⅲ-nitride alloys are direct bandgap. Basically, GaN, InN, and AlN can be used to cover a wide region from deep-ultraviolet (DUV) to red by tuning the material composition in these alloys because they can be mixed as a wide continuous emission wavelength of the spectrum. For this reason, these Ⅲ-nitride compounds have gained much attention by several research groups since a couple of decades ago. The optoelectronic devices, LEDs and LDs, are not only able to make the technology of full color displays and high density optical storage (>40Gb) come true, but are able to reduce the consumption of about 10-20% of power energy. In the past few years, conventional 630/650-nm LDs based on AlGaInP had been maturely commercialized in digital versatile disk (DVD) systems for a long time. It is worth saying that the wavelength of the new generation DVD picks based on nitride-based can reach 405 nm. Nowadays, the blue ray

4

DVD has two specifications, HD-DVD and BD-DVD, which have their own supporters. The former is supported by HITACHI and MICROSOFT and the latter is supported by SONY. As long as the wavelength is getting shorter, the DVD players will have larger storage space. Therefore, we expect that UV spectrum will be adopted as read instruments in the optical storage system in the next generation. However, several bottlenecks in the growing techniques of Ⅲ-nitride materials, such as (1) poor crystalline quality, (2) lattice mismatch substrate, and (3) low-resistivity p-type doping claddings, still need to be broken through.

At early stage, the difficulty for growing nitride-based alloys was the lack of lattice-matched substrate, so the crystalline quality was poor. This problem had been solved until 1983 when Dr. Yoshida improved the crystal quality of GaN films with the use of AlN-coted sapphire (Al_2O_3) substrate.[9] After that, high-quality optical flat surfaces of GaN thin films had been successfully grown by using AlN buffer layer with MOVPE technique by Prof. Akasaki *et. al*.[10]. In 1991, S. Nakamura first chose low-temperature growth GaN as the buffer layer and got high quality GaN films. [11] At the moment, the sapphire became the most commonly substrate used to grow the Ⅲ-nitride materials because the sapphire had several advantages, such as high hardness, high heat-resistance and non-absorption for green and blue spectrum. Most importantly, it was cheaper than other substrate! In spite of these advantages, there were still some disadvantages, for instance, the interface between GaN and the sapphire substrate existed a large lattice constant mismatch of 15%[12], resulting in a

highly dislocation density. To reduce the dislocation density, A. Usui *et al*., hence developed a

so-called epitaxially laterally overgrowth GaN (ELOG) method to get much more quality

GaN films in 1997.[13] In addition, the sapphire was an insulator so both n and p contacts

shall be on the top of the devices, and etching techniques were absolutely required. The lower

p-type dopant was another problem which had been solved until Akasaki *et al*. [14]

demonstrated that compensated Mg-doped GaN could be converted into conducting p-type

material by low energy electron beam irradiation (LEEBI) method. Consequently, the hole

concentration and lower-resistivity were $1x10^{17}$ cm^{-3} and 12 $\Omega \cdot$ cm, respectively. In 1991,

high concentration($3x10^{18}$ cm^{-3}) and low-resistivity($0.2 \Omega \cdot$ cm) of the hole were obtained by

S. Nakamura by utilizing the same method, LEEBI, as mentioned before and thermal

annealing technique.[15],[16]
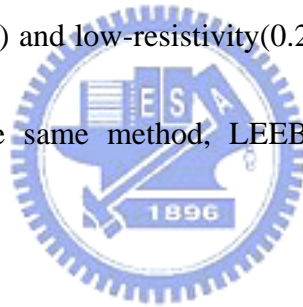
On the whole, the techniques of growing for Ⅲ-nitride materials seemed to be very

good. ELOG sapphire substrate was used to obtain high-quality crystalline GaN films and

reduced the dislocation density. Highly p-type doped and lower-resistivity GaN films had

been announced. Although, these troubles (high dislocation density and high-resistivity)

suppressed the development of Ⅲ-nitride semiconductors to become the leading materials in

the UV and blue region of the spectrum for a time. But many researchers made an effort to

develop the model of Ⅲ-nitride LEDs and LDs continuously. In the following subsections,

some useful parameters for Ⅲ-nitride materials will be introduced.

1.1.1 Bandgap Energy of Ⅲ-nitride Alloys

Band structures and bandgap energy are essential characteristics in the optoelectronic semiconductor materials. The Ⅲ-nitride alloys system is consist of GaN, AlN, and InN which belong to the direct bandgaps. Hence, when they are mixed into ternary or quaternary material, such as indium gallium nitride (InGaN), aluminum gallium nitride (AlGaN), aluminum indium nitride (AlInN), and aluminum indium gallium nitride (AlInGaN), which bandgaps are still direct. It means whatever we change the composition ratio of the compound that the efficiency of the devices does not reduce remarkably. This is one of the reasons why the nitride-based materials can be the highly bright emitting devices in the UV and blue spectrum.

As being mentioned before, nitride-based materials are mainly made up of three binary compounds (GaN, AlN, and InN), so the bandgap energy of these nitride-based compounds is also made up of these binary materials. Besides, the bandgap energy of these three binary materials is related to the temperature. Therefore, we will extend this discussion to ternary nitride-based compound in the next paragraph.

The bandgap energy of GaN, AlN, and InN at temperature T can be expressed by the *Varshni* formula (1.1).[17]

$$E_g(T) = E_g(0) - \frac{\alpha T^2}{T + \beta} , \tag{1. 1}$$

where $E_g(T)$ is the bandgap energy at trmperature T, $E_g(0)$ is the bandgap energy at zero Kelvin, α and β are material-related constants. The values of α, β, and $E_g(T = 0)$ of the binary alloys are listed in Table 1.1 and Table 1.2. The value of β is approximately equal to the Debye temperature at 0 K. These constants were measured by several methods i.e., photoluminescence (PL), optical absorption, and photoreflectance. The bandgap energy of wurtzite GaN on sapphire substrate at the room temperature is 3.42 eV which is announced by Morkoc [18], Maruska [19] *et al.*. Report results of other groups are listed in Table 1.1.

Table 1.1 Bandgap energy of GaN and related-temperature parameters
(a：optical absorption ; b：photoluminescence (PL))

Reference	$E_g(0)$ (eV)	α (meV/K)	β (K)	*note*
[20]	3.48	0.939	772	MBE、epitaxial layer (a)
[20]	3.57	1.08	745	MBE、bulk (a)
[21]	3.512	0.566	737.9	MOCVD (a)
[21]	3.458	1.156	1187.4	MBE (a)
[22]	3.503	0.508	996	VPE (b)
[23]	3.510	0.856	700	MBE (b)

The bandgap energy and the related-temperature parameters of wurtzite AlN and InN binary alloys described with *Varshni* formula by Q. Guo and A. Yoshida [24]-[26] are listed in

Table 1.2.

Table 1.2 Bandgap energy of AlN and InN and related-temperature parameters

Reference	$E_g(0)$ (eV)	α (meV/K)	β (K)	note
AlN [24]	6.026	1.799	1462	–
AlN [25]	6.2	–	–	–
AlN [26]	6.2	–	–	–
InN [24]	1.970	0.245	624	–
InN [27]	0.76	–	–	OMVPE (b)
InN [28]	0.75	–	–	OMVPE(b)

The bandgap energy of $In_xGa_{1-x}N$ ternary alloys measured by Osamura et $al.$ [29] at room temperature (RT) is treated as (1.2).

$$E_{g,In_xGa_{1-x}N}(x) = 2.07x + 3.4(1-x) - b \cdot x \cdot (1-x) \ (eV),$$ (1. 2)

where the values of 3.4 and 2.07 are the GaN and InN energy bandgap at RT, x is the composition of the indium, and b is the so-called bowing parameter (also called bowing vector), which is 1.0 eV. The bandgap energy dependent on the indium composition of In_xGa_{1-x} N has also been widely investigated by numerous researchers.[30],[31] Moreover, more different bowing parameters of InGaN ternary alloys can be searched as well, which are listed in Table 1.3.

The bandgap energy of $Al_yGa_{1-y}N$ ternary alloys at room temperature (RT) is treated as (1.3).

$$E_{g,Al_yGa_{1-y}N}(y) = 6.28y + 3.42(1-y) - b \cdot y \cdot (1-y) \ (eV),$$ (1. 3)

where the values, 3.42 and 6.28, are bandgap energy of GaN and AlN at RT[8], y is the composition of the aluminum, and b is bowing parameter (also called bowing vector), which is equal to 1.0 ± 0.3 eV. However, some other groups announced that the ternary bandgap energy can be described by a linear relationship with the composition of AlN and GaN. At this situation, it means that the bowing parameter b is zero. Moreover, more different bowing parameters of AlGaN ternary alloys can be searched as well, which are listed in Table.1.4.

Table 1.3 Bowing parameter of InGaN ternary alloys

Reference	Bowing parameter	Reference	Bowing parameter
[32]	2.39	[35]	3.35
[33]	2.65	[36]	3.8
[34]	3.2	[37]	4.11

Table 1.4 Bowing parameter of AlGaN ternary alloys

Reference	Bowing parameter	Reference	Bowing parameter
[38]	0.62 ± 0.45	[41]	1.3
[39]	0.53	[42]	1.3 ± 0.2
[40]	0.6		

After mentioning about the ternary alloys, we introduce the quaternary alloys about aluminum indium gallium nitride (AlInGaN). Mostly, the band parameters of quaternary alloys can be expressed in linear interpolation formula as (1.4)

$$P(Al_xIn_yGa_{1-x-y}N) = x \cdot P(AlN) + (1-x-y) \cdot P(GaN) + y \cdot P(InN).$$ (1. 4)

For the bandgap energy of AlInGaN, some reported with rather small indium fraction. M Asif Khan found that the bandgap energy of AlInGaN reduced almost linearly when the composition of indium is less than 2%.[43] A relationship for the calculation of composition dependent parameters by a weighted sum of ternary alloys has also been permitted. The bandgap energy of AlInGaN can be described as (1.5). [44]

$$E_g(AlInGaN) = \frac{xy \cdot E_g^u(AlInN) + yz \cdot E_g^v(InGaN) + zx \cdot E_g^w(AlGaN)}{xy + yz + zx},$$ (1. 5)

where $E_g^u(AlInN) = u \cdot E_g(InN) + (1-u) \cdot E_g(AlN) - b_{AlInN} \cdot u \cdot (1-u)$, (1. 6)

$$u = \frac{1-x+y}{2} \quad v = \frac{1-y+z}{2} \quad w = \frac{1-x+z}{2},$$ (1. 7)

where x, y, and $z = 1-x-y$ represent the compositions of Al, In, and Ga in the AlInGaN

alloy. The bandgap energy of ternary InGaN and AlGaN can be depicted in equations (1.6) and (1.7).

1.1.2 Band-offset Values of Ⅲ-nitride Alloys

The value of band-offset, which plays a very important role in the analysis of energy band diagram, is quite significant for the design of heterostructure devices. In some other textbooks, band-offset is also called band discontinuity, and it is obvious that when two different materials are grown next to each other, the conduction and the valence bands of the two materials will become discontinuous at the interface. The concepts of the quality and even feasibility of heterojunction device often crucially depend on the values of these band-offsets. Several researchers investigate the band-offset values of Ⅱ-Ⅵ and Ⅲ-Ⅴ heterostructures experimentally by the growing techniques such as MBE and MOCVD. To determine band-offset values of semiconductor materials, X-ray photoelectron spectroscopy (XPS) and ultraviolet photoelectron spectroscopy (UPS) are primarily used by means of the electron core level energy. Furthermore, optical techniques, for instance, excitation PL and reflectivity, are also presented with a more accurate tool to determine band-offset values. However, the devotion of the determination of the band-offset values in semiconductor hetero-junction from experimental measurements and theoretical calculations exists large discrepancy which may be related to different factors in the following.

(A) Technical difficulty and often indirect nature of measurements,

(B) Possible dependence of band discontinuity on detailed,conditions of interface preparation,

(C) Strain dependence of band discontinuity.

And they may be related to the difficulty of obtaining high equality epitaxial films.

Various types of band alignments can arise in the semiconductor interfaces which depend on the relative adjustment of energy bands with respect to each other. For semiconductor heterojunctions, there are two most common types of alignments. Type I alignment is the bandgap of one semiconductor that lies completely within the other bandgap. This type is the most useful one in the optoelectronic devices because the carriers are well confined in the smaller bandgap region. Type II alignment is the bandgap of the overlap of two materials but not completely covering to each other. We can see the two types of alignments in Fig. 1.1.
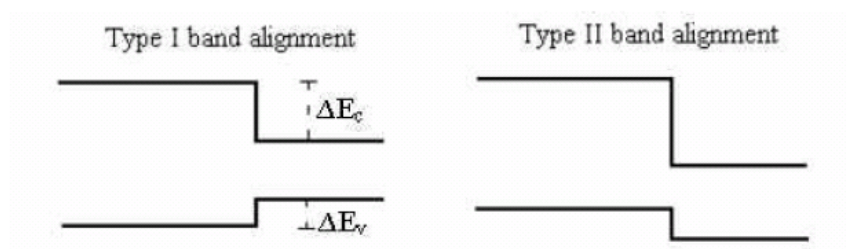
Fig. 1.1 Schematic designation of type I and type II band alignment

All of nitride-based materials belong to type Ⅰ, and six different kinds of heterojunction

combination, such as AlN/GaN, InN/GaN, GaN/AlN, InN/AlN, AlN/InN, and GaN/InN (A/B

represents that a thin film is grown on top of B material), are listed. Table 1.5 lists some

band-offset values of wurtzite nitride binary alloys reported by Martin *et al.*

Table 1.5 Valence band-offset values of nitride binary alloys (Unit：eV)

Reference	AlN/GaN	InN/GaN	GaN/AlN	InN/AlN	AlN/InN	GaN/InN
[45]	0.8 ±0.3	–	0.8 ±0.3	–	–	–
[46]	0.57 ±0.22	0.93 ±0.25	0.60 ±0.24	1.71 ±0.20	1.32 ±0.14	0.59 ±0.24
[47]	–	–	0.5 ±0.5	–	–	–
[48]	1.36 ±0.07	–	–	–	–	–
[49]	0.81	0.48	0.81	1.25	1.25	0.48
[50]	0.84	0.26	0.84	1.04	1.04	0.26

The Ⅲ-nitrides are piezoelectric material which means the strain induces static electric

fields via the piezoelectric effect. Figure 1.2 shows how a strain induces piezoelectric field to

change the valence band-offset value. It is obvious that strain which induces piezoelectric

fields always tends to decrease valence band-offset value.
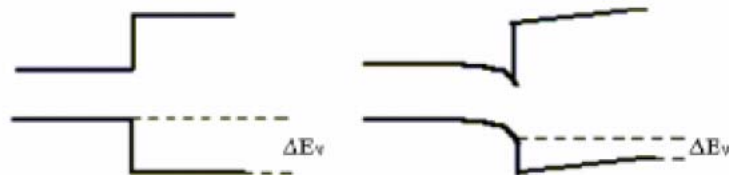
Fig. 1.2 Schematic representation of how piezoelectric effects change the measured
band-offset value.

The ratios of conduction band discontinuities to valence band discontinuities ($\Delta E_c : \Delta E_v$)

are roughly 30:70 for InN-GaN, 75:25 for GaN-AlN, and 60:40 for InN-AlN, respectively.[51]

Table 1.6 lists the valence band-offset values after piezoelectric correction.

Table 1.6 Valence band-offset values after piezoelectric correction

Heterojunction	InN-GaN	GaN-AlN	InN-AlN
ΔE_v (eV)	1.05 ± 0.25	0.7 ± 0.24	1.81 ± 0.20

1.1.3   Lattice Constants of Ⅲ-nitride Alloys

In the design process of the semiconductor devices, lattice constant is quite important.

Not only different lattices can result in different types of strains, but also it may cause huge

effects on the efficiency of the devices. This phenomenon can be obviously found in the

nitride-based materials.

Table 1.7 Lattice constants of binary AlN, GaN , and InN alloys

Reference	a -lattice constant ($\overset{o}{\text{A}}$)			c -lattice constant ($\overset{o}{\text{A}}$)		
	AlN	GaN	InN	AlN	GaN	InN
[58]	3.112	3.188	3.533 3.548	4.982	5.185	5.963 5.760
[52]	3.112[a]	3.188[a]	3.542	4.982[a]	5.185[a]	5.72
[53]	3.112[a]	3.189	3.54	4.982[a]	5.185[a]	5.70
[54]	3.091	3.174	3.538	4.954	5.169	5.707
[55]	3.111	3.189	3.544	4.978	5.185	5.718
[56]	3.112	3.210	--	4.995	5.237	--
[57]	3.112	3.188	--	4.982	5.185	--
[58]	3.06	3.17	3.53	4.91	5.13	5.54
[59]	--	3.162	--	--	5.142	--
[60]	3.10	3.22	3.59	4.97	5.26	5.81
[61]	3.144	3.146	--	5.046	5.125	--

Note: a represents the datum from reference [58] originally.

Table 1.7 lists the lattice constants from different references of binary AlN, GaN, and

InN. It is noteworthy that Ⅲ-nitride materials are usually grown on c-face sapphire substrates.

The lattice constants of the ternary AlGaN and InGaN can be described by *Vegard's Law*

which linearly combines the lattice constants of two binary alloys and obtains the lattice

constants of ternary alloys. For example, the lattice constant of $In_xGa_{1-x}N$ can be expressed in

(1.8) and (1.9).

$$a_{InGaN}(x) = a_{GaN} \cdot (1-x) + a_{InN} \cdot x , \qquad (1.8)$$

$$c_{InGaN}(x) = c_{GaN} \cdot (1-x) + c_{InN} \cdot x,$$ (1. 9)

where $a_{InGaN}(x)$ and $c_{InGaN}(x)$ represent the lattice constant of InGaN material of x indium composition, a_{GaN}, a_{InN}, and c_{GaN}, c_{InN} are binary GaN and InN lattice constants.

1.2   Introduction to Nitride Based LEDs

The nitride-based materials, such as GaN and the related ternary (AlGaN and InGaN) and quaternary (AlInGaN) compounds, are considered more promising for high-brightness emission, and currently they have been used commercially to make the blue-violet and green LEDs. Except for the blue-violet light sources, the nitride-based materials also have the potential to become the main materials of the light sources for the whole range of visible light due to their large variation of bandgap energy from 0.78 eV to 6.2 eV. Figure 1.3 shows the bandgap energy of GaN, AlN, InN, and their ternary compounds or possible quaternary compounds as a function of the lattice constants.[8]
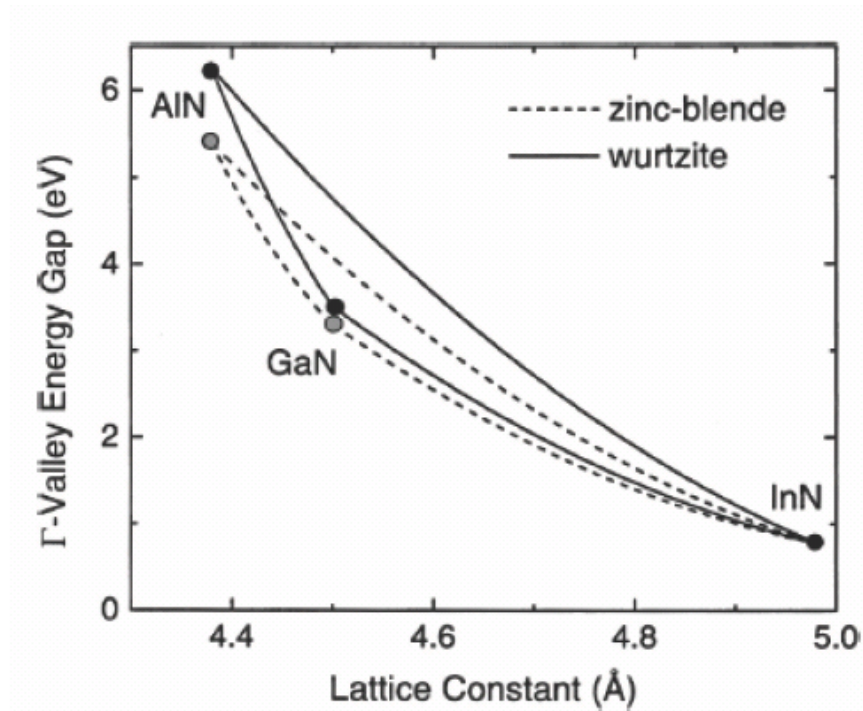
Fig. 1.3 Bandgap energy of GaN, AlN, InN, and their ternary compounds or possible quaternary compounds as function of the lattice constants.[8]

In this section, a brief history of development of Ⅲ-nitride LEDs and recent commercialized Ⅲ-nitride LED structures are introduced.

Since the first candela-class blue LEDs were fabricated in 1994[62], the market of blue LEDs has almost been dominated by Ⅲ-nitride materials. As shown in Fig. 1.4, the achievement of Ⅲ-nitride LEDs has been rapidly increased since 1994, and recently super high-brightness LEDs has been also fabricated.[63] Furthermore, we can see the development of LEDs with other materials in Fig. 1.4 as well.

Fig. 1.4 A review of the historical revolution of LEDs.[64]

Basically, green LEDs can be fabricated with Ⅲ-nitride materials by increasing the composition of indium in InGaN active layers. Unfortunately, poor crystal quality of InGaN active layers, which reduces LED performance, is found due to large lattice mismatch between active layers and claddings. Therefore, it is too difficult for high-performance green LEDs to be commercialized in early stage. Nakamura *et al.* fabricated blue InGaN/GaN double-heterostructure LEDs for the first time in 1993 with the use of two-flow MOCVD growing technique. The c-face (0001 orientation) sapphire was used as the substrate and the flow was laterally grown at atmospheric pressure. Utilizing this technique, the LED characteristic was obtained. The peak wavelength was 440 nm with a full width at half maximum (FWHM) of 20 nm at forward current of 20 mA. To obtain blue emission, the first candela-class blue LEDs were fabricated with the use of Si and Zn codoped InGaN active

layer. Due to higher the composition of indium in InGaN layer that might cause the decrease

of luminescence intensity, relatively low composition of indium in InGaN layer was used. The

thickness of InGaN active layer was 50 nm, and the active layer was sandwiched between two

150-nm-thick $Al_{0.15}Ga_{0.85}N$ cladding layers. The output power and external quantum

efficiency at 20 mA were 1.5 mW and 2.7%, respectively.[62] Soon afterward, the

InGaN/InGaN multiple-QW structures and several novel designs were employed in

GaN-based LEDs, and the first commercial GaN-based LEDs were commercialized by Nichia

Chemical Company in 1990s. To date, it is less than fifteen years that high-brightness

GaN-based LEDs are used throughout the world, for example, in the applications of full-color

displays, traffic signals, chemical processes, and medical applications.
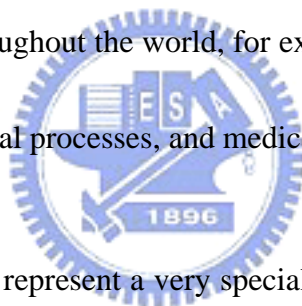
Ⅲ-nitride and their alloys represent a very special class of material. They are indeed the

best choice for short wavelength emission due to their wide and direct bandgap energy. Unlike

the arsine or phosphide materials, there is not a suitable substrate for their growth, and they

are in the hexagonal (wurtzite) crystal system. Mostly, the polarization effect in GaN-based

materials has been found much stronger than other Ⅲ-Ⅴ compounds. Next, the properties of

materials of wurtzite GaN and their relevant alloys are investigated.

1.3　Introduction to Nitride Based EELs & VCSELs

The research of blue light emitting devices started from the development of gallium nitride (GaN) light emitting diodes in the early 1970s. Two decades later, the first room-temperature (RT) pulse-operation LDs under pulse current injection were successfully demonstrated by Nakamura *et al.* in 1996. This made nitride-based laser diodes begin to be widely used in many applications such as laser printers, high-density storages, compact projectors, and so on. Recently, the performance of nitride-based laser diodes has been announced to emit power as high as 100mW at RT with a low threshold current density only 3kA/cm^2, and the LDs have been already effectively commercialized to be applied to digital versatile discs (DVDs).
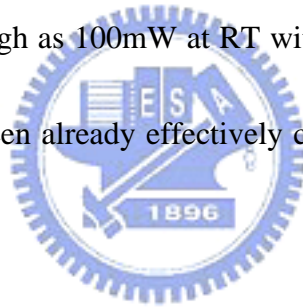
(A)　Edge Emitting Lasers (EELs)

The major type of commercial nitride-based laser diodes is edge emitting laser. This kind of structure is currently the most mature one among all nitride laser devices. It is made by a stripe-type long cavity and a pair of cleaved facet as the mirror. Generally, the cavity length of this structure shown in Fig. 1.5(a) is about several hundred micrometers. In these years, several groups improved and researched on the growth and optimization of its structure. One of them improved the huge amounts of defects and threading dislocations existing in the

grown nitride-based materials on the sapphire substrate due to large lattice-mismatch between

the nitride-based material and sapphire. The epitaxally lateral overgrowth (ELOG) was a very

efficient method to reduced threading dislocation and defect density. Other one was to raise

the lower confinement factor of the optical field in the structure. Due to the small difference

of index between $Al_xIn_{1-x}N$ and GaN, the guiding ability of optical field in active region was

usually weak. Nakamura et. al. solved this problem with using modulation doped strain

superlattice layer to improve the optical confinement.[65],[66]

Another issue was quantum confined stark effect (QCSE) which was resulted from the

spontaneous polarization and piezoelectric field in multiple quantum well. Recently, M.

Schmidt et. al.[67] and D. Feezell *et al.*[68] demonstrated nonpolar laser diodes on m-plane

GaN substrate. Moreover, in this thesis, we try to use the quaternary alloys (AlInGaN) in

quantum barrier layer to eliminated QCSE, and the details will be discussed in Chapter 4. The

fabrication of flat and high-reflectivity mirrors is also a key point for achieving an excellent

lasing performance. In order to obtain a flat facer, the etching and cutting techniques are

rapidly developed.

(b) Vertical Cavity Surface Emitting Lasers (VCSELs)

Except for the edge emitting lasers, K. Iga [69] demonstrated a new kind of laser diodes,

vertical cavity surface emitting lasers (VCSELs) which is a vertical-emitting-type laser, in

1977. The structure is shown in Fig. 1.5(b). But why should K. Iga *et al.* develop this kind of laser different from EELs? The vertical surface emitting lasers have many advantageous properties, including circular beam shape, small divergence, light emission in the vertical direction, two-dimensional arrays on the wafer level, low threshold, and so on.

It is formed by sandwiching a few-lambda cavity in a pair of reflectors, usually in the form of distributed Bragg reflector (DBR), with a very high reflectivity (>99.9%). The DBR mirrors provide longitudinal optical confinement. In recent years, several efforts have been devoted to the realization of nitride-based VCSELs. Currently, three kinds of structures are reported. The First one is "fully epitaxial grown VCSEL structure" which uses the lattice-matched AlInN/GaN as the bottom and top reflectors to avoid the occurrence of the cracks due to the accumulation of the strain after stacking large pairs of layers. The second one is "VCSEL structure with two dielectric mirrors" which is employed in some process techniques such as wafer bonding and laser lift-off to make dielectric mirrors be coated onto both sides of nitride-based cavity. The third one is "VCSEL structure with hybrid mirrors". The so-called hybrid mirrors are the combination of two different kinds of reflectors, for example, a dielectric mirror and an epitaxial reflector. Typically, the fabrication of this structure is to grow the bottom reflector and cavity using MOCVD, and then coat dielectric mirror to complete VCSEL structure. In the comparison of these three VCSELs, it does not require the complicated process, for example, laser lift-off technique, to complete a hybrid

23

VCSEL device. This means the fabrication of such structure is stable and reliable comparing to other structures. Hence, the hybrid structure is more advantageous in the aspects of fabrication and commercialization.
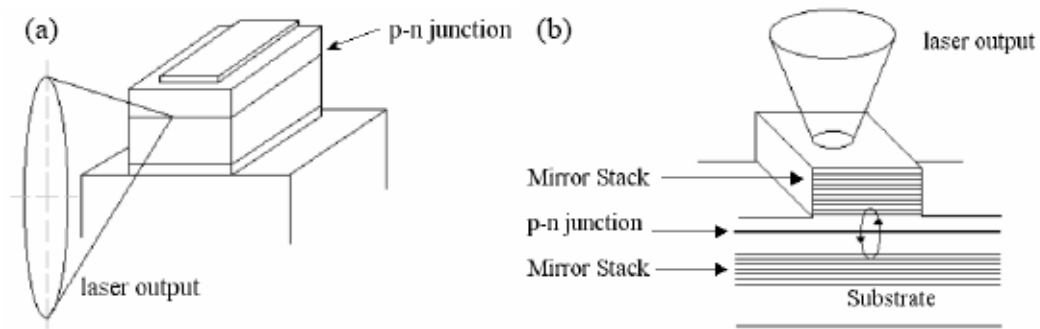
Fig. 1.5 Sketch of semiconductor laser diode structures. (a) Edge emitting laser. (b) VCSEL

Chapter 2 Physical Model and Theoretical Considerations

2.1. Introduction

Qualitative numerical analysis can help us figure out the output characteristics of the optoelectronic semiconductor devices. And it can also help for modulation and the optimization of the simulation to the performance of the devices.

In this thesis, we use commercial simulation software named LASTIP (Laser Technology Intergrated Program) published by Crosslight Software Inc., an international company headquartered in Vancouver, Canada. Crosslight Software (Formerly Beamtek Software) is the first commercial company to provide CAD software for electrical and optical modeling of laser diodes (LDs), and it has maintained the leadership position in that field since then. Typical laser emission L-I-V curves, 2D potential, electric field, and current distribution, special electron and hole concentrations, band diagram, optical field distribution, gain spectrum, and far-field patterns can be obtained. It is a useful simulation program to give a qualitative theoretical analysis and to provide a way to realize the physics of the optoelectronic semiconductor lasers. The numerical analysis of the simulation is based on $k \cdot p$ theory published by Luttinger-Kohn, utilizing Hamiltonian matrix and envelope function to solve the structure of the quantum well subband. This physical model includes basic Poisson's

equation, current continuity equations, photon rate equations, and scalar wave equations, etc.

In addition, other formulae describe the carrier characteristics and the boundary conditions.

2.2. Model of the Software

The software, LASTIP, includes the calculation of carrier transportation, thermonic

emission, optical gain, and waveguide of the transversal plane, etc. The effect of heat is very

important for the efficiency of the semiconductor laser diodes. Hence, all factors about the

heat such as Joule heating, recombination heat, Thomson heat, and Peltier heat are almost

considered into this software. [70]
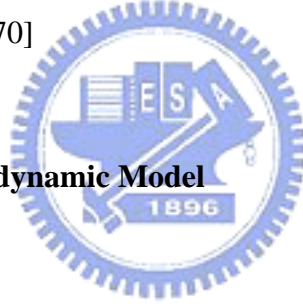
2.2.1. Drift-Diffusion/Hydrodynamic Model

In the semiconductor field, several physical phenomena are described with different

models. In general, the drift-diffusion model which can explain many basic characteristics in

semiconductor devices is a well-known basic model. We can use Poisson's equation to

describe the behaviors of the devices. As for current continuity equation for electrons and

holes, they can be described as expression (2.2) and (2.3)

$$-\nabla \cdot (\frac{\varepsilon_0 \varepsilon_{dc}}{q} \nabla V) = -n + p + N_D(1 - f_D) - N_A f_A + \sum_j N_{tj}(\delta_j - f_{tj}),\tag{2.1}$$

$$\nabla \cdot J_n - \sum_j R_n^{tj} - R_{sp} - R_{st} - R_{au} + G_{opt}(t) = \frac{\partial n}{\partial t} + N_D \frac{\partial f_D}{\partial t},$$ (2.2)

$$\nabla \cdot J_p - \sum_j R_p^{tj} + R_{sp} + R_{st} + R_{au} - G_{opt}(t) = -\frac{\partial p}{\partial t} + N_A \frac{\partial f_A}{\partial t},$$ (2.3)

where V, n, and p are the electric potential, the electron concentration, and the hole concentration, respectively. N_D, N_A, and N_{tj} represent the shallow donors concentration, the shallow acceptors concentration, and the deep level trap concentration, respectively.

Moreover, f_D, f_A, and f_{tj} means their occupying level. J_p and J_n are electron and hole current density. R_p^{tj}, R_n^{tj}, R_{sp}, R_{st}, and R_{au} are the recombination rate of the electron and hole deep level trap, the spontaneous recombination rate, the stimulated recombination rate, and the Auger recombination rate, respectively. These equations provide the descriptions of the behaviors of the electrons and holes in the semiconductor devices field.

2.2.2. Gain Model

In general gain model theory, the gain and the loss of a material can be treated as the functions of the wavelength and the carrier density for bulk and quantum well. Because the wide bandgap of the nitride-based materials have lower dielectric constants, the optical gain of the quantum well structure of the AlInGaN compounds can be calculated by the Coulomb

enhanced gain spectral function. [71]

$$g(\hbar\omega) = real\left\{\int_{E_{g0}}^{\infty} \frac{g_0(E_{cv})}{1-q_1(E_{cv},\hbar\omega)}\left[1-i\frac{E_{cv}-\hbar\omega}{\Gamma_{cv}}\right]L(\hbar\omega-E_{cv})dE_{cv}\right\}$$

(2.4)

Here,

$$q(E_{cv},\hbar\omega) = \frac{-ia_0E_0E_{cv}}{\pi k\,|\,M_{ji}(E_{cv})\,|}\int_0^{\infty}dk'k'\frac{|\,M_{ji}(E_{cv'})\,|}{E_{cv'}}\times\frac{f_e(E_{cjk'})+f_h(E_{vjk'})-1}{\Gamma_{cv}+i(E_{cv}-\hbar\omega)}\times\Theta(k,k')$$

(2.5)

and

$$\Theta(k,k') = \int_0^{2\pi}d\theta\frac{1+C_{pl}ka_0q^2/32\pi N_{2D}}{1+q/k+C_{pl}ka_0q^2/32\pi N_{2D}},\,q^2=k^2+k'^2-2kk'\cos\theta\,,$$

(2.6)

where θ is the angle of the vector k and k', and $g_0(E_{cv})$ is the spectral wave function

including $g_{ji}(E_{cv})$ which means the summation of the jth-subband and the ith-subband holes

transition. Γ_{cv} represents the Lorenzian width and also equals to $\hbar/\tau_{cv}$. Furthermore, we

regard $\hbar\omega$ and E_{cv} as constants in the way of simplifying the calculation. a_0 is the

exciton Bohr radius. ($a_0=\dfrac{4\pi\hbar^2\varepsilon_b\varepsilon_0}{e^2m_{rj}}$) E_0 is the Rydberg energy.
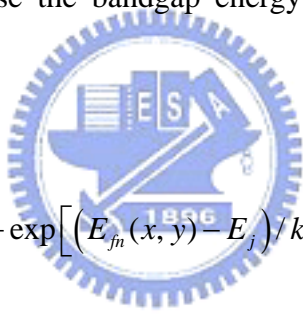
$E_{cv}(k) = E_g + \Delta E_g + E_{cjk} + E_{vik}$. E_{cjk} E_{vik} are the energy of the electrons and the holes of the

j^{th}-subband of conductor band and the ith-subband of valence band in the active region.

$|\,M_{ji}\,|^2$ is the transition matrix element. C_{pl} is the unit constant ranged from one to four.

2.2.3. Self-Consistent Density Model

When the potential well is under a strong electric field, such as a piezoelectric field, the quantum well will be skewing. At the same time, the wave functions confined in the quantum well are also separated and the behaviors of the optical transition are different from those in flat quantum well. Hence, some effects occur to the device characteristic. For this reason, we need a new model to re-calculate the bandgap energy and the wave function.

Moreover, the self-consistent carrier density model is used to solve the piezoelectric field in the quantum well and revise the bandgap energy and the wave function expressed in equation (2.7).

$$n_{2D}(x, y) = \sum_j g_n^j(y) \rho_j^0 kT \ln \left\{ 1 + \exp \left[\left(E_{fn}(x, y) - E_j \right) / kT \right] \right\} \tag{2.7}$$

where the subscript j represents all the confined states, and $g_n^j(y)$ is hypothesized the wave function of the quantum well paralleling the x-axis. ρ_j^0 is the 2D density of state. E_j is the confined level.

The self-consistent process as follows,

(1) First of all, utilize the flat band to solve under thermal equilibrium, and it will get an initial potential distribution.

(2) Second, utilize the self-consistent carrier density model, and replace the initial potential

distribution with the result from the first step into the calculation. Thus, we can obtain a new

carrier distribution density.

(3) Third, use the iteration method at the second step until the convergence of the carrier

distribution and the potential distribution.

Finally, increase bias voltage and take the second and the third step again after repeating

the iteration method. The correct potential and the distribution of wave function will be

obtained

2.3. Summary

Previously, we introduce several important physical models illustrated much detailed in

ref.[72]. Furthermore, we can use Fig. 2.1 to explain the relationship with these equations.
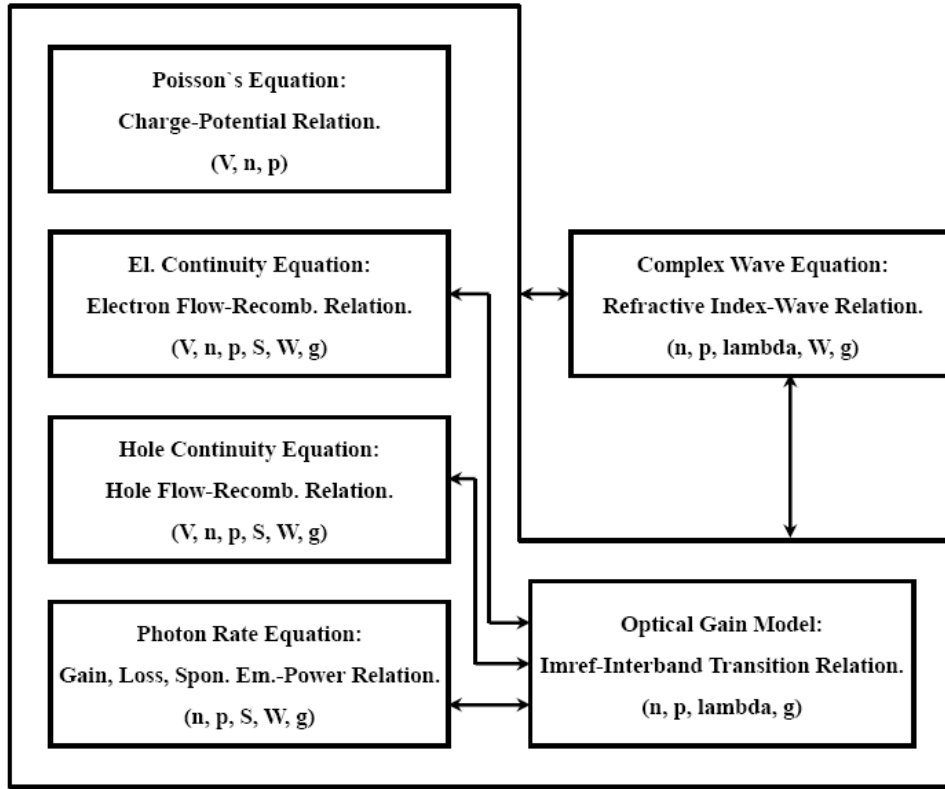
Fig. 2.1 The relationship between these equations

where V is the electric potential. n and p represent the concentrations for the electrons and holes. S and W are the photon numbers and the wave intensity, respectively. lambda means the emit wavelength and g means the gain value.

Chapter 3 Numerical Study on Optimization of Active Layer

Structures for GaN/AlGaN MQW Ultraviolet Laser Diodes

3.1 Paper Review

Group-III nitride semiconductors have received much attention in the past few years due to their promising applications in the field of optoelectronic devices such as light-emitting diodes (LEDs) used in solid-state lighting and laser diodes (LDs) used in high-density optical storage systems. Recently, GaN-based high-efficiency optoelectronic devices in the blue and green regions have been realized and commercialized by achieving breakthroughs in the improvement of crystal quality and the realization of conductivity control. New ultraviolet laser diodes are also expected for the applications in frontier technologies such as super-high density optical storage systems, high-resolution laser printers, biological sensing, full-color projection displays, biotechnology applications, and an excitation source of optical catalyst.[73] However, in the ultraviolet region the high-efficiency group-III nitride optoelectronic devices are still difficult to fabricate, especially for ultraviolet laser diodes. One main reason is the difficulty in obtaining high-quality AlGaN materials due to the low diffusion length of aluminum atom or the aluminum-containing molecules on the surface of epitaxial film. Moreover, it is difficult to achieve high p-type conductivity in p-type AlGaN alloys due to high activation energy of Mg dopants [74]. A further problem is that the

GaN/AlGaN system does not have isolation of carriers from nonradiative recombination centers unlike the InGaN/GaN system. [73], [75] Therefore, the reported lifetimes of ultraviolet laser diodes are still quite short from a commercial viewpoint.

Despite the material quality or fabrication problems, realizations of the ultraviolet laser diodes have been reported. 365 nm ultraviolet laser diodes using quaternary AlInGaN single-quantum-well structure were demonstrated under continuous wave (cw) operation at 25°C by Masui *et al.* in 2003. The estimated lifetime of the 365 nm ultraviolet laser diodes was approximately 2000 hours at an output power of 3 mW under cw operation at 30°C.[76] Kneissl *et al.* also realized ultraviolet AlGaN multiple-quantum-well laser diodes with emission wavelengths between 359.7 and 361.6 nm in the same year. [77] Furthermore, Edmond *et al.* achieved cw laser diode operation from 348 nm to 410 nm by using AlInGaN/AlGaN material system grown on SiC substrates in 2004.[78] Recently, GaN/AlGaN multiple-quantum-well ultraviolet laser diode with 350.9-nm-lasing wavelength has been demonstrated by Iida *et al.*.[73], [79],[80]   Nevertheless, the laser diode was still operated under pulsed current injection.

In order to achieve high performance ultraviolet laser diodes, systematic and compact theoretical modeling is a necessary approach to improve existing laser structures and understand internal physical processes, which provides timely and efficient guidance toward

the optimal structure design and device parameters. In this study, effects of quantum-well

number and quantum-barrier aluminum composition on threshold properties of ultraviolet

GaN/AlGaN multiple-quantum-well laser diodes are theoretically studied in detail by using an

advanced LASer Technology Integrated Program (LASTIP), which self-consistently

combines quantum well band structure calculations by 6×6 *k·p* theory, radiative and

nonradiative carrier recombination, carrier drift and diffusion, and optical mode

computation.[81] Since different quantum-barrier aluminum composition in GaN/AlGaN

quantum wells result in different refractive indices, bandgap energies, and interface charge

densities induced by spontaneous and piezoelectric polarization, it is expected that the laser

performance will be varied with different quantum-barrier aluminum compositions. Although

the similar research on AlGaN/AlGaN system has been reported by Chow *et al.* [82], we will

focus our study on GaN/AlGaN system and systematically discuss the effects of

quantum-well number, quantum-barrier aluminum composition, and quantum-well thickness

on ultraviolet GaN/AlGaN multiple-quantum-well laser performance. Furthermore, how the

different physical mechanisms influence the threshold properties is shown in this study as

well.

3.2 Theoretical Model & Structure and Parameters of GaN/AlGaN LDs

The self-consistent LASTIP simulation program combines band structure and gain calculations with two-dimensional (2-D) simulations of wave guiding, carrier transport and heat flux. The carrier transport model includes drift and diffusion of electrons and holes in devices. Built-in polarization induced by spontaneous and piezoelectric polarization is considered at hetero-interfaces of nitride related devices. In the quantum wells, self-consistent Poisson and Schrödinger equations are recomputed at every bias point for the states of quantum well levels and carrier distributions. In the optical mode model, a 2-D scalar complex wave equations is solved for the lateral modes. By calibrating with specific material parameters, LASTIP is a useful tool to access new designs, understand internal physical process, and optimize existing devices [83].

The physical model of the GaN/AlGaN quantum wells is considered in such a way that the conduction bands are assumed to be decoupled from valence subbands and have isotropic parabolic bands due to the larger bandgap of nitride semiconductor and the valence band structures, which includes the coupling of the heavy-hole (HH), the light-hole (LH), and the spin-orbit split-off bands, are calculated by the 6×6 Hamiltonian with envelop function approximation. By using the basis transformation, the 6×6 Hamiltonian can be transformed into a block-diagonalized Hamiltonian [84],
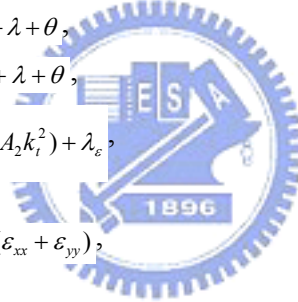
$$H_{6\times6} = \begin{bmatrix} H^U & 0 \\ 0 & H^L \end{bmatrix} \tag{3.1}$$

with

$$H^U = \begin{bmatrix} F & K_t & -iH_t \\ K_t & G & \Delta - iH_t \\ iH_t & \Delta + iH_t & \lambda \end{bmatrix} \tag{3.2}$$

$$H^L = \begin{bmatrix} F & K_t & iH_t \\ K_t & G & \Delta + iH_t \\ -iH_t & \Delta - iH_t & \lambda \end{bmatrix} \tag{3.3}$$

$$F = \Delta_1 + \Delta_2 + \lambda + \theta,$$

$$G = \Delta_1 - \Delta_2 + \lambda + \theta,$$

$$\lambda = \frac{\hbar^2}{2m_0}(A_1 k_z^2 + A_2 k_t^2) + \lambda_\varepsilon,$$

$$\lambda_\varepsilon = D_1 \varepsilon_{zz} + D_2(\varepsilon_{xx} + \varepsilon_{yy}),$$

$$\theta = \frac{\hbar^2}{2m_0}(A_3 k_z^2 + A_4 k_t^2) + \theta_\varepsilon,$$

$$\theta_\varepsilon = D_3 \varepsilon_{zz} + D_4(\varepsilon_{xx} + \varepsilon_{yy}),$$

$$K_t = \frac{\hbar^2}{2m_0} A_5 k_t^2,$$

$$H_t = \frac{\hbar^2}{2m_0} A_6 k_z k_t,$$

$$\Delta = \sqrt{2}\Delta_3, \text{ and } k_t^2 = k_x^2 + k_y^2, \tag{3.4}$$

where m_0 is the free electron mass. The A_i parameters are related to the hole effective masses.

The crystal-field split energy is $\Delta_{cr} = \Delta_1$ and the spin-orbit splitting is $\Delta_{so} = 3\Delta_2 = 3\Delta_3$. The D_i

parameters are deformation potential constants.

To obtain the numerical parameters required for *k·p* calculations for the AlGaN materials, a linear interpolation between the parameters of the relevant binary semiconductors is utilized except for the unstrained bandgap energies. The material parameters of the binary semiconductors are taken from the paper by Vurgaftman and Meyer and summarized in Table. 3.1.

Table 3.1 The material parameters of the binary semiconductors

Parameter	Symbol (unit)	GaN	AlN
Lattice constant	a_0 (Å)	3.189	3.112
Spinorbit split energy	Δ_{so} (eV)	0.017	0.019
Crystalfield split energy	Δ_{cr} (eV)	0.010	0.169
Hole effective mass parameter	A_1	7.21	3.86
	A_2	0.44	0.25
	A_3	6.68	3.58
	A_4	3.46	1.32
	A_5	3.40	1.47
	A_6	4.90	1.64
Hydrost. deform. potential (*c* axis)	a_z (eV)	4.9	3.4
Hydrost. deform. potential (transverse)	a_t (eV)	11.3	11.8
Shear deform. potential	D_1 (eV)	3.7	17.1
	D_2 (eV)	4.5	7.9
	D_3 (eV)	8.2	8.8
	D_4 (eV)	4.1	3.9
Elastic stiffness constant	C_{33} (GPa)	398	373
Elastic stiffness constant	C_{13} (GPa)	106	108
Electron effective mass (*c* axis)	m_e^z / m_0	0.2	0.32
Electron effective mass (transverse)	m_e^t / m_0	0.2	0.30

The unstrained AlGaN bandgap energies can be expressed as

$$E_{g,\text{AlGaN}}(x) = x \cdot E_{g,\text{AlN}} + (1-x) \cdot E_{g,\text{GaN}} - b \cdot x \cdot (1-x),$$ (3. 5)

where b is the bandgap bowing parameter of AlGaN, which is 0.7 eV in our calculation . The temperature dependent bandgap energies of the relevant binary semiconductors are calculated using the commonly employed Varshni formula

$$E_g(T) = E_g(T=0) - \frac{\alpha T^2}{T+\beta} \cdot$$ (3. 6)

The values of α, β, and $E_g(T=0)$, i.e., the bandgap energy at zero Kelvin, of the binary alloys are listed in Table. 3.3 .

Table 3.2 Bandgap energy of GaN and AlN and related-temperature parameters

Parameter (unit)	GaN	AlN
α (meV/K)	0.909	1.799
β (K)	830	1462
$E_g(T=0)$ (eV)	3.51	6.25

The optical gain spectra of quantum-well structures, with the valence-band-mixing effect being taken into account, can be expressed by [85]

$$g(\hbar\omega) = g_{sp}(\hbar\omega)\left[1 - \exp\left(\frac{\hbar\omega - (F_c - F_v)}{k_B T}\right)\right], \tag{3.7}$$

$$g_{sp}(\hbar\omega) = \frac{2q^2\pi}{nc\varepsilon_0 m_0^2 \omega L_z} \times \sum_{\sigma=U,L}\sum_{n,m}\int \left|M_{nm}^{\sigma}(k_t)\right|^2 \frac{f_n^c\left(1 - f_{\sigma m}^v\right)(\gamma/\pi)}{\left(E_{cn} - E_{kpm} - \hbar\omega\right)^2 + \gamma^2}\frac{k_t}{2\pi}dk_t, \tag{3.8}$$

where q is the free electron charge, $\hbar$ is the reduced Planck's constant, n is the index of refraction, ε_0 is the free-space dielectric constant, c is the speed of light, L_z is the thickness of quantum well, $\hbar\omega$ is the photon energy, $M_{nm}(k_t)$ is the momentum matrix element in the quantum well, $1/\gamma$ is the intraband scattering relaxation time, E_{cn} is the nth conduction subband, E_{kpm} is the mth valence subband from the k·p calculation, f_c^n and f_v^m are the Fermi functions for the conduction band states and the valence band states respectively. The indices n and m denote the electron states in the conduction band and the heavy hole (light hole) subband states in the valence band. To account for the broadening due to scattering, it is assumed that τ = 0.1 ps [85] in the calculations. The conduction band offset ratio $\Delta E_c / \Delta E_g$ for the AlN/GaN interface is between 0.66 and 0.81 according to the recent calculations. In our calculations, this value is assumed to be 0.7 based on published literatures.

The physical model of carrier transport is the traditional drift-diffusion model for semiconductors. The specific equations can be expressed as

$$\bar{J}_n = q\mu_n n\bar{F} + qD_n\nabla n,$$

(3. 9)

$$\bar{J}_p = q\mu_p p\bar{F} - qD_p\nabla p,$$

(3. 10)

where n and p are the electron and hole concentrations, $\bar{J}_n$ and $\bar{J}_p$ are the current densities of electrons and holes, $\bar{F}$ is the electrostatic field, μ_n and μ_p are the mobilities of electrons and holes. The diffusion constants D_n and D_p are replaced by mobilities using the Einstein relation $D = \mu k_B T/q$. The equations used to describe the semiconductor device behavior are Poisson's equation,

$$\nabla\cdot\left(\varepsilon_0\varepsilon\bar{F}\right) = q(p - n + p_D - n_A \pm N_f)$$

(3. 11)

and the current continuity equations for electrons and holes,

$$\frac{1}{q}\nabla\cdot\bar{J}_n - R_n + G_n = \frac{\partial n}{\partial t},$$

(3. 12)

$$\frac{1}{q}\nabla\cdot\bar{J}_p + R_p - G_p = -\frac{\partial p}{\partial t},$$

(3. 13)

where ε is the relative permittivity. G_n and R_n are the generation rates and recombination rates for electrons, G_p and R_p are the generation rates and recombination rates for holes, respectively. The electric field is affected by the charge distribution, including the electron

and hole concentrations, dopant ions p_D and n_A, and other fixed charges N_f that are of special importance in nitride-based devices due to the effect of built-in polarization.

Built-in polarization induced due to spontaneous and piezoelectric polarization is known to influence the performance of nitride devices. In order to consider the built-in polarization within the interfaces of nitride devices, the method developed by Fiorentini *et al*. is employed to estimate the built-in polarization, which is represented by fixed interface charges at each hetero interface. They provided explicit rules to calculate the nonlinear polarization for nitride alloys of arbitrary composition. [86] For the GaN/AlGaN quantum-well lasers under study, the net surface charges at all interfaces are calculated and listed in Table. 3.3.

Table 3.3 The net surface charges at all interfaces are calculated

Interface	Built-in charge density
GaN/Al$_{0.18}$Ga$_{0.82}$N	-7.84×10^{12} cm^{-2}
Al$_{0.18}$Ga$_{0.82}$N/Al$_{0.08}$Ga$_{0.82}$N	$+4.56\times10^{12}$ cm^{-2}
Al$_{0.08}$Ga$_{0.92}$N/Al$_{0.25}$Ga$_{0.75}$N	-8.08×10^{12} cm^{-2}
Al$_{0.25}$Ga$_{0.75}$N/Al$_{0.08}$Ga$_{0.92}$N	$+8.08\times10^{12}$ cm^{-2}
Al$_{0.08}$Ga$_{0.92}$N/GaN	$+3.28\times10^{12}$ cm^{-2}
GaN/Al$_{0.08}$Ga$_{0.92}$N	-3.28×10^{12} cm^{-2}
Al$_{0.08}$Ga$_{0.92}$N/Al$_{0.18}$Ga$_{0.82}$N	-4.56×10^{12} cm^{-2}

Although the interface charges can be obtained by this theoretical model, experimental investigations often find weaker built-in polarization than that predicted by theoretical calculation. It is mainly attributed to partial compensation of the built-in polarization by

defect and interface charges. [87] Typical reported experimental values are of 20%, 50% or 80% smaller than the theoretically calculated values. [88] As a result, 50% of the theoretical polarization values are used in our simulation from the average of the reported values.

A widely used empirical expression for modeling the mobility of electrons and holes is the Caughey~Thomas approximation, which is employed in our calculation and can be expressed as [89]

$$\mu(N) = \mu_{\min} + \frac{\mu_{\max} - \mu_{\min}}{1 + (N/N_{ref})^{\alpha}}$$ (3. 14)

where $\mu_{\min}$, $\mu_{\max}$, N_{ref}, and α are fitting parameters according to the experimental mobility measurements. We employ this carrier mobility model for binary GaN material in our calculation. The relative parameters are summarized in Table 3.4.[90] ,[91]

Table 3.4 The relative parameters of this carrier mobility model

Parameter	$\mu_{\max}$	$\mu_{\min}$	N_{ref}	α
(unit)	$(cm^2V^{-1}s^{-1})$	$(cm^2V^{-1}s^{-1})$	(cm^{-3})	(–)
Electrons [33]	1405	80	0.778×10^{17}	0.71
Holes [32]	170	3	3×10^{17}	2

As for ternary AlGaN, the analytical expressions for mobility as a function of doping density have been established by Monte Carlo simulation for various nitride alloys. [92] Non-radiative recombination is commonly characterized by Shockley-Read-Hall (SRH) recombination and is governed by the defect-related nonradiative SRH lifetime (τ_{SRH}). Defect density and nonradiative lifetime depend on the substrate used and on the growth quality. In this study, we employ a common value of $\tau_{SRH} = 1$ ns in our simulation. [93] The calculation of carrier capture and escape from the quantum wells is considered in accordance with the model provided by Romero *et al.*.[94] As for the parameter of refractive index, Adachi model is employed to calculate the refractive index values in each layer listed in Table. 3.5. [38-40] More description about the physical models utilized in LASTIP simulation program can be found in [96]–[98].
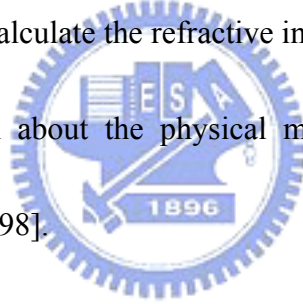
In this simulation, the GaN/AlGaN laser diode structure under study is referred to the real structures [73], [79], [80]. We first assume that the GaN/AlGaN laser diode is grown on an *n*-type $Al_{0.18}Ga_{0.82}N$ layer that is 4.0 m in thickness. On top of this $Al_{0.18}Ga_{0.82}N$ layer is a 0.12- m-thick *n*-type $Al_xGa_{1x}N$ confining layer. The multiple-quantum-well active region consists of three 3-nm-thick GaN quantum wells and 8-nm-thick $Al_xGa_{1x}N$ barriers. A 20-nm-thick *p*-type $Al_{0.25}Ga_{0.75}N$ electronic blocking layer is grown on top of the active region to reduce electron leakage into the *p*-type AlGaN layer [83], [99], [100]. Furthermore, a 0.12- m-thick *p*-type $Al_xGa_{1x}N$ confining layer and a 0.7- m-thick *p*-type $Al_{0.18}Ga_{0.82}N$

cladding layer are grown. Finally, a 20-nm-thick *p*-type GaN cap layer is grown to complete the

structure. The aluminum composition in the $Al_xGa_{1x}N$ barrier and the confining layers are

varied from 8% to 16%. The effective active region of the ridge geometry is 4   m in width and

the cavity is 500   m in length. The reflectivities of the two end mirrors are set at 50% and 90%,

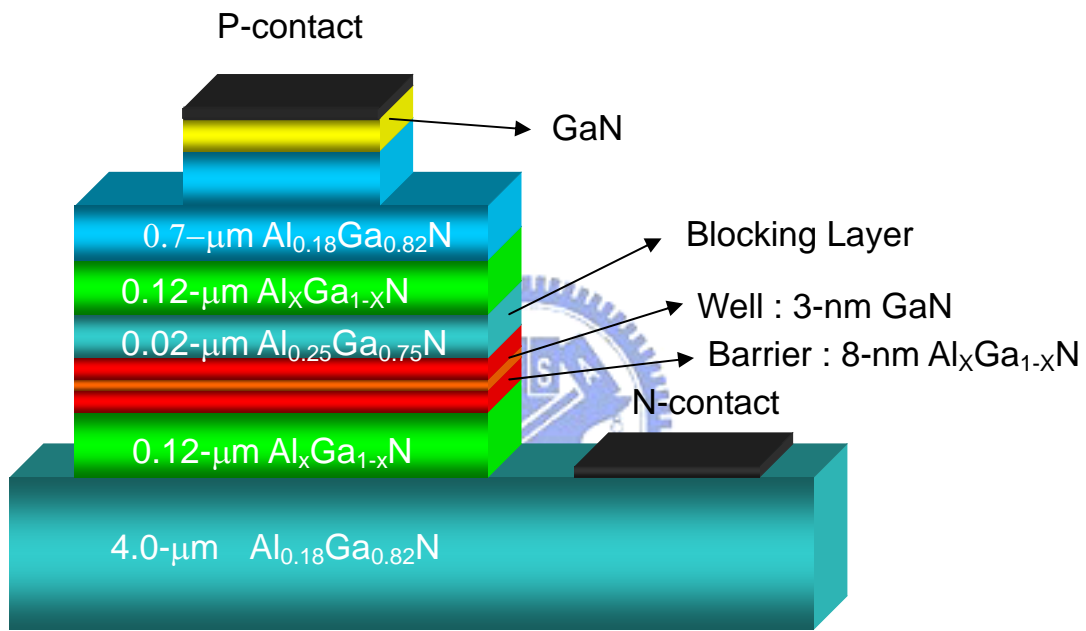respectively. We illustrate the device structure in Fig 3.1.

Fig. 3.1 The illustration of the device structure

The doping concentrations in each layer and the detailed device structure are described in

Table. 3.5. The doping data in this table gives the actual densities of free carriers.

Table 3.5 The detailed device structure, the refractive index values, and the doping
concentrations in each layer are described

Parameter (unit)	d (nm)	N_{dop} (1/cm^3)	n
p-GaN (contact layer)	20	1×10^{18}	2.9
p-Al$_{0.18}$Ga$_{0.82}$N (cladding layer)	700	1.4×10^{17}	2.365
p-Al$_{0.08}$Ga$_{0.92}$N (confining layer)	120	1×10^{17}	2.654
p-Al$_{0.25}$Ga$_{0.75}$N (blocking layer)	20	1.4×10^{17}	2.167
i-Al$_{0.08}$Ga$_{0.92}$N (barrier layer)	8	—	2.654
i-GaN (quantum well)	3	—	2.9
i-Al$_{0.08}$Ga$_{0.92}$N (barrier layer)	8	—	2.654
i-GaN (quantum well)	3	—	2.9
i-Al$_{0.08}$Ga$_{0.92}$N (barrier layer)	8	—	2.654
i-GaN (quantum well)	3	—	2.9
i-Al$_{0.08}$Ga$_{0.92}$N (barrier layer)	8	—	2.654
n-Al$_{0.08}$Ga$_{0.92}$N (confining layer)	120	1×10^{17}	2.654
n-Al$_{0.18}$Ga$_{0.82}$N (cladding layer)	4000	2×10^{18}	2.365
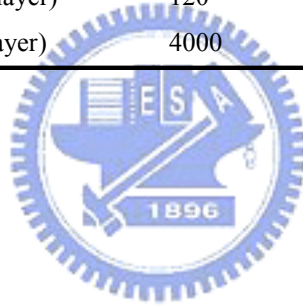
3.3 Optimization of QW Numbers, Quantum Barrier Aluminum Composition, and

Quantum Well Thickness & Physical Mechanisms Discussions

The laser output power of the GaN/Al$_{0.08}$Ga$_{0.92}$N laser diode structure as a function of

input current is shown in Fig. 3.2. when the number of quantum wells varies from one to five.

The simulation results indicate that the best laser performance is obtained when the number of

quantum wells is three and the worst laser performance is observed when the number of

quantum wells is one.
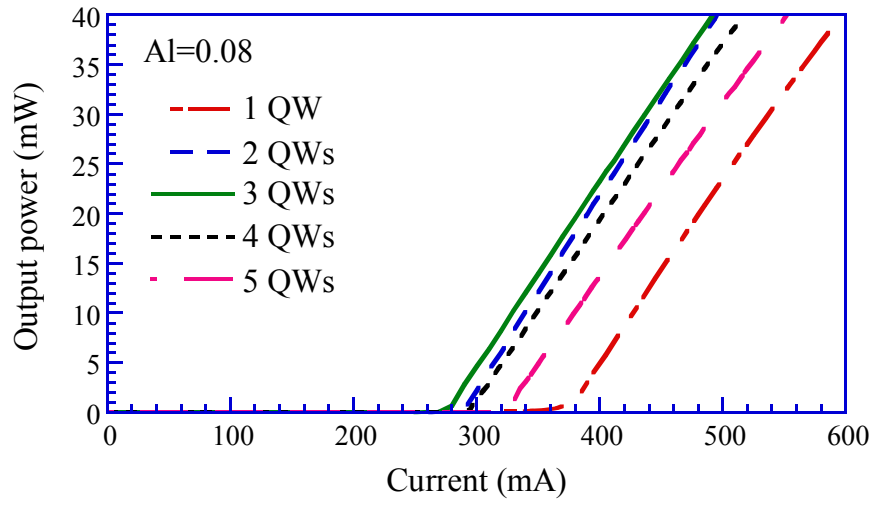
Fig. 3.2 The laser output power of the GaN/Al$_{0.08}$Ga$_{0.92}$N laser diode structure as a function of input current

In order to further study the effects of quantum-barrier aluminum composition on threshold current of the GaN/Al$_x$Ga$_{1-x}$N laser diodes. The threshold current values of the laser diodes with different barrier aluminum compositions are plotted in Fig. 3.3 when the number of quantum wells varies form one to five. According to the simulation results, optimal barrier aluminum composition is about 10~ 12% for the GaN/Al$_x$Ga$_{1-x}$N quantum-well lasers.
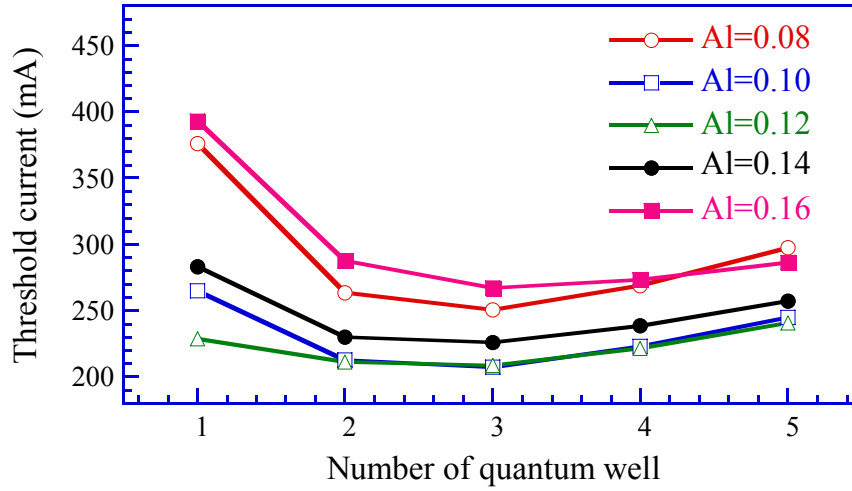
Fig. 3.3 The threshold current values of the laser diodes with different barrier aluminum compositions

Lower and higher aluminum compositions in $Al_xGa_{1-x}N$ barrier/confining layer result in larger threshold current values. Furthermore, in this study the optimized number of quantum wells for $GaN/Al_xGa_{1-x}N$ laser diodes is found to be three. This optimal quantum-well number consists with that of the experimental laser structure employed by Iida *et al.* [73], [79], [80]. All possible internal physical mechanisms which lead to these results will be discussed and analyzed in detail in the following content.

A.   Electron Leakage Current

In order to understand the internal physical mechanisms which result in the worst laser performance in the cases of lower barrier aluminum composition and fewer number of quantum wells, the vertical electron current density profiles within the active regions of laser structures

with $Al_{0.08}Ga_{0.92}N$ and $Al_{0.16}Ga_{0.84}N$ barrier layers, respectively, are plotted in Fig. 3.3 at 400

mA injection current. This driving current is chosen to be above the threshold current values of

the laser diodes under study. The positions of five quantum wells are marked with gray areas.

The left-hand side of the figure is the n-side of the device. The electron current is injected from

n-type layers into quantum wells and recombines with holes in quantum wells.
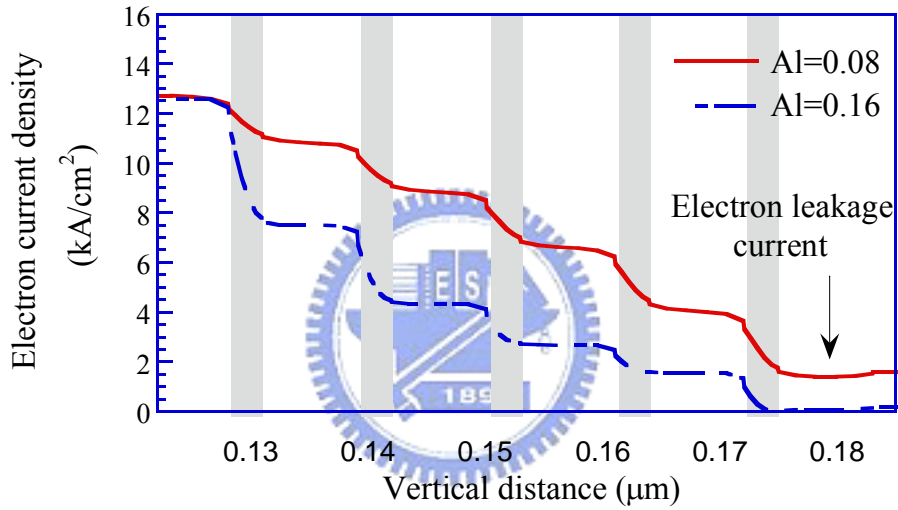
Fig. 3.4 The vertical electron current density profiles within the active regions of laser
structures with $Al_{0.08}Ga_{0.92}N$ and $Al_{0.16}Ga_{0.84}N$ barrier layers, respectively (400 mA injection
current)

Therefore, the electron current density is reduced in the quantum wells. Electron current

which overflows through quantum wells is viewed as leakage current. The problem of electron

leakage current plays an important role for the optical performance of III-nitride laser diodes

which are mostly operated at high injection level [83], [99], [100]. Several methods have been

proposed to suppress the leakage current, such as increasing p-type doping concentration to

increase the barrier height [101] and employing the multi-quantum barrier (MQB) structure to block the overflowing electrons [102]. Besides, optimizing the active region structure is another approach to minimize the electron leakage current. The increases of quantum-well number and height of quantum barrier provide better electron confinement, especially for high operation temperature and high current injection. In Fig. 3.4 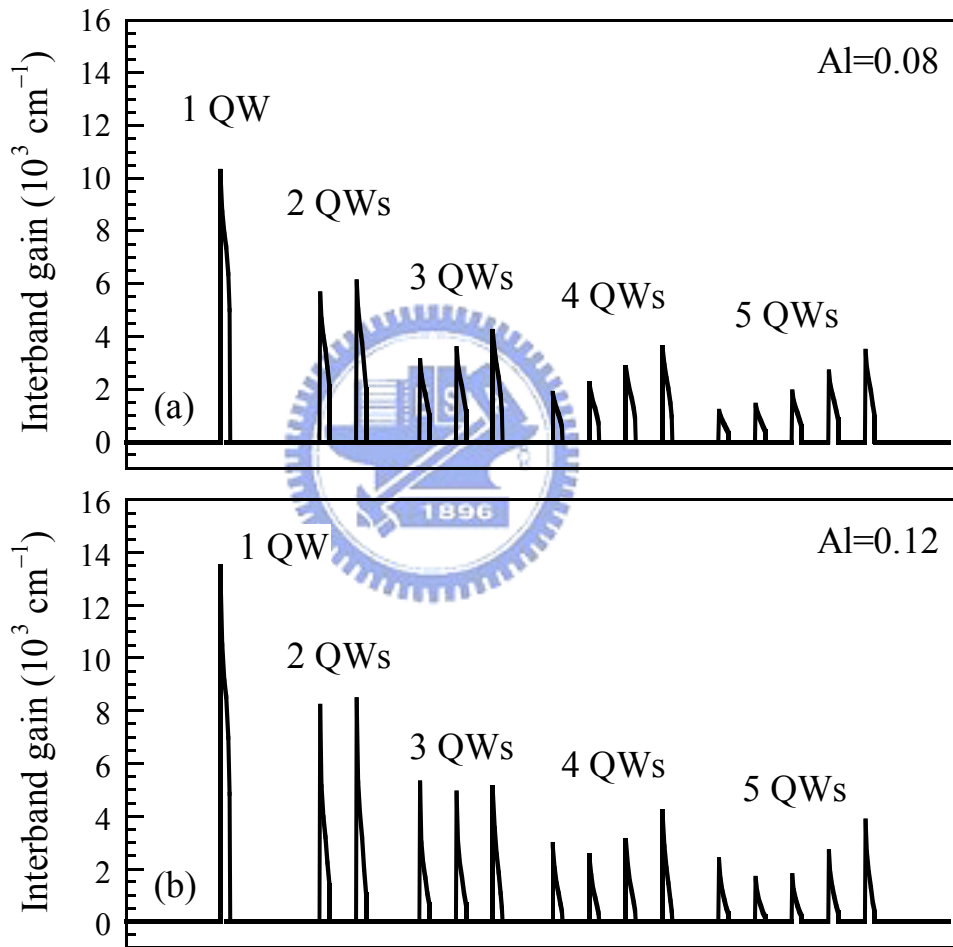the electron leakage current is still observed even though the number of quantum wells is five in the $GaN/Al_{0.08}Ga_{0.92}N$ laser diode structure. On the contrary, when the barrier aluminum composition increases from 8% to 16%, better electron confinement is provided and electron leakage current is hardly observed. Therefore, the increase in barrier height by adding more aluminum composition in barrier layer is also an effective approach to suppress the electron leakage current except for the increase in quantum-well number.

B. *Non-uniform Carrier Distribution*

Multiple-quantum-well laser diode performance is significantly affected by non-uniform carrier distribution within the multiple-quantum-well active regions [103]. It is expected that this effect will be more critical for nitride-based laser diodes since the conduction band offset is relatively higher than that of conventional III-V semiconductor heterostructures [104]. The non-uniform carrier distribution will also lead to the non-uniform interband gains within multiple-quantum-well active regions. In order to study the effect of non-uniform carrier

distribution induced by quantum-well number and quantum-barrier aluminum composition, the

interband gains in the active regions of the GaN/Al$_x$Ga$_{1-x}$N laser diodes with different barrier

aluminum compositions are illustrated in Fig. 3.5 at an input current of 400 mA when the

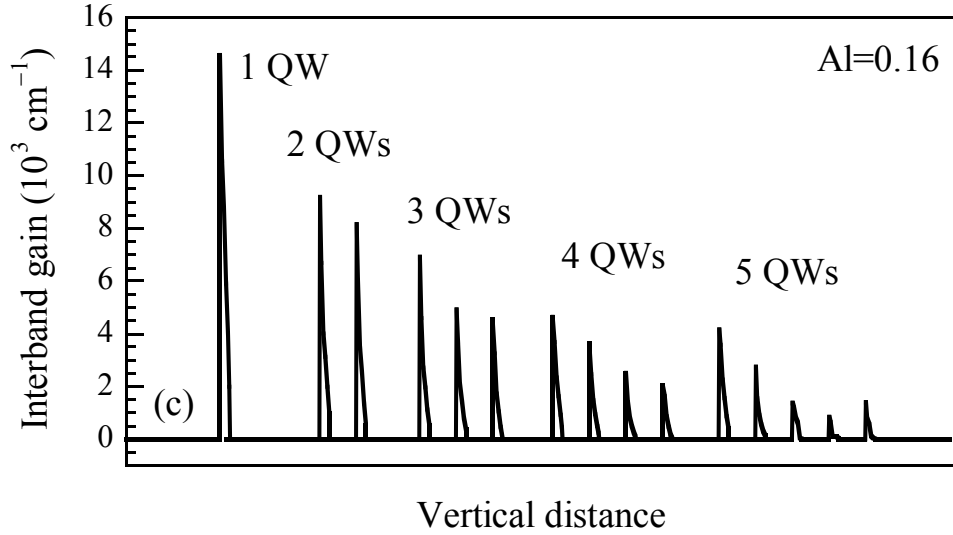number of quantum wells varies from one to five.

Fig. 3.5 The interband gains in the active regions of the GaN/Al$_x$Ga$_{\bar{1}x}$N laser diodes with different barrier aluminum compositions (400 mA injection current)

In Fig. 3.5(a), the GaN/Al$_{0.08}$Ga$_{0.92}$N laser diode structure induces serious electron leakage current due to poor electron confinement, which results in lower interband gain, especially for the laser structures with fewer number of quantum wells. Therefore, when the number of quantum wells is less than three, the interband gain increases with aluminum composition in barrier layer. However, as shown in Fig. 3.5(c), although the GaN/Al$_{0.16}$Ga$_{0.92}$N laser diode structure provides better carrier confinement due to the higher aluminum composition in barrier layer, the interband gain values in the quantum wells become very non-uniform, and the highest interband gain is always observed in the well closest to the n-side. Furthermore, relatively more uniform interband gain values in multiple-quantum-well active region are observed when the barrier aluminum composition is 0.12, as shown in Fig. 3.5(b). Consequently, when the number of quantum wells is more than three, the non-uniform interband gain in multiple-quantum-well active region is obvious with increasing aluminum composition in barrier layer. The deep

quantum well with a high aluminum composition barrier is the main mechanism which makes

the non-uniform interband gain in active region with multiple-quantum-well structure. To

further understand the effects of non-uniform interband gain on laser threshold current, Fig. 3.6

shows the conduction band structure, quasi-Fermi level, and interband gain for the

three-quantum-well active layers with a $Al_xGa_{1-x}N$ barrier of (a) $x = 0.08$, (b) $x = 0.12$, and (c) x

$= 0.16$ under an operation current of 400 mA. In Fig. 3.6(a), shallow quantum wells make the

electron overflow severe, which can be observed from the distribution of quasi-Fermi level

across the three quantum wells. Nevertheless, as the aluminum composition in barrier layer

increases, the non-uniform distribution of electron carriers in the deep quantum wells is obvious,

as indicated in Fig. 3.6(c). In this situation, the interband gain decreases gradually as the well

position is close to the p-type layer. Consequently, by comparing Fig. 3.6(a), Fig. 3.6(b), and

Fig. 3.6(c), when altering the aluminum composition of the barrier layers, a compromise

between reducing the electron overflow and an uniform electron distribution is required. Hence,

the results for triple-quantum-well $GaN/Al_xGa_{1-x}N$ active layer structure with $x = 0.12$ gives the

optimum performance.

(a)

(b)
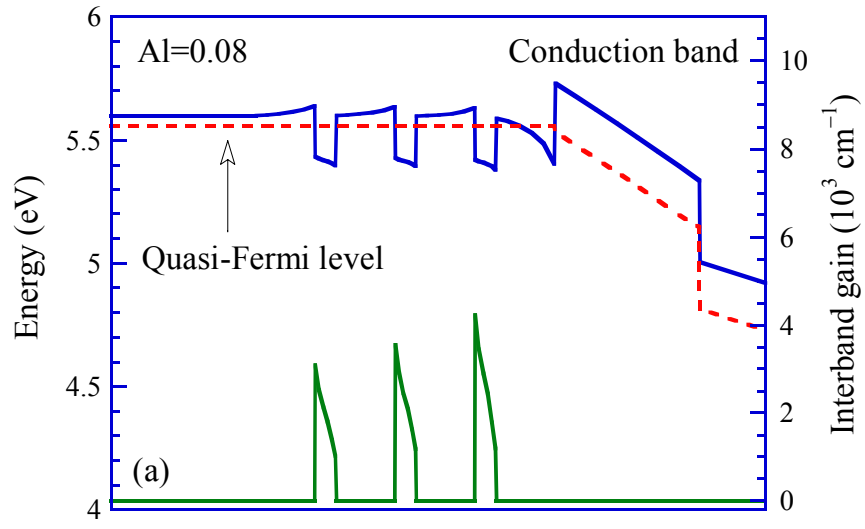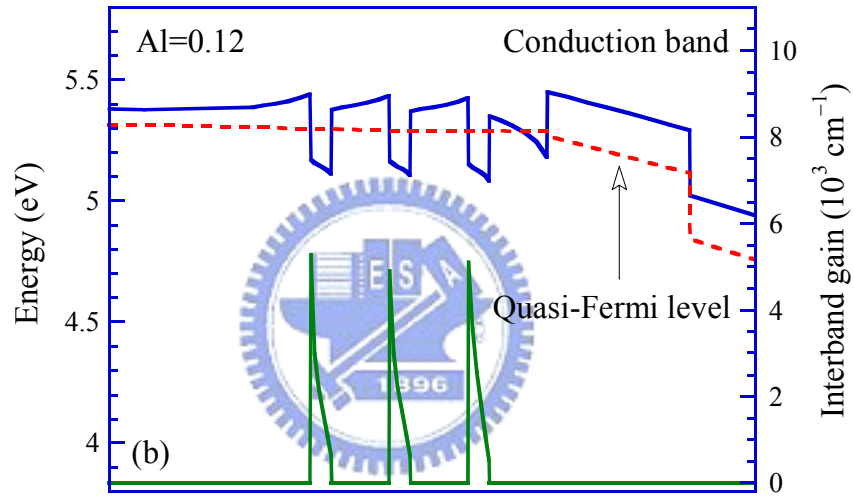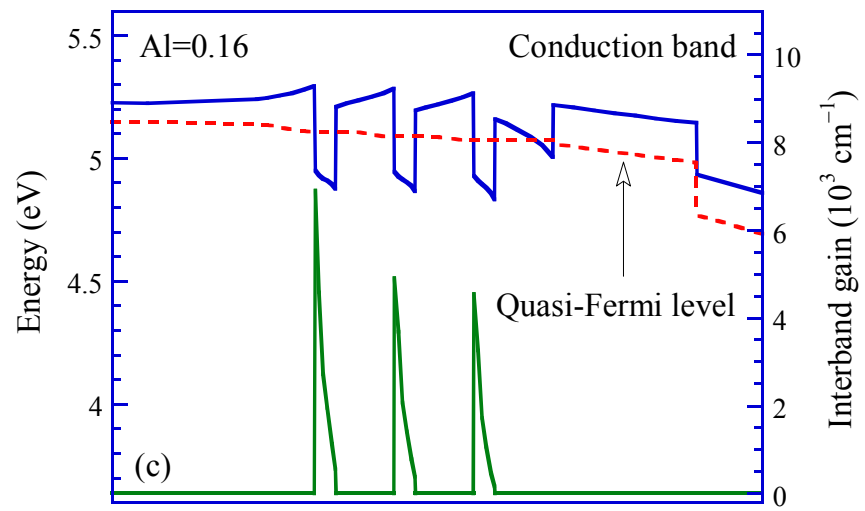
(c)

Fig. 3.6 The conduction band structure, Quasi-Fermi level, and interband gain for the three-quantum-well active layers with a $Al_xGa_{1-x}N$ barrier of (a) $x = 0.08$, (b) $x = 0.12$, and (c) $x = 0.16$ under an operation current of 400 mA

C. Spontaneous and Piezoelectric Polarization

Fig. 3.7 shows the electron and hole concentration distribution in active region for the laser structures with a $Al_xGa_{1-x}N$ barrier of (a) $x = 0.08$, (b) $x = 0.12$, and (c) $x = 0.16$ under an operation current of 400 mA.
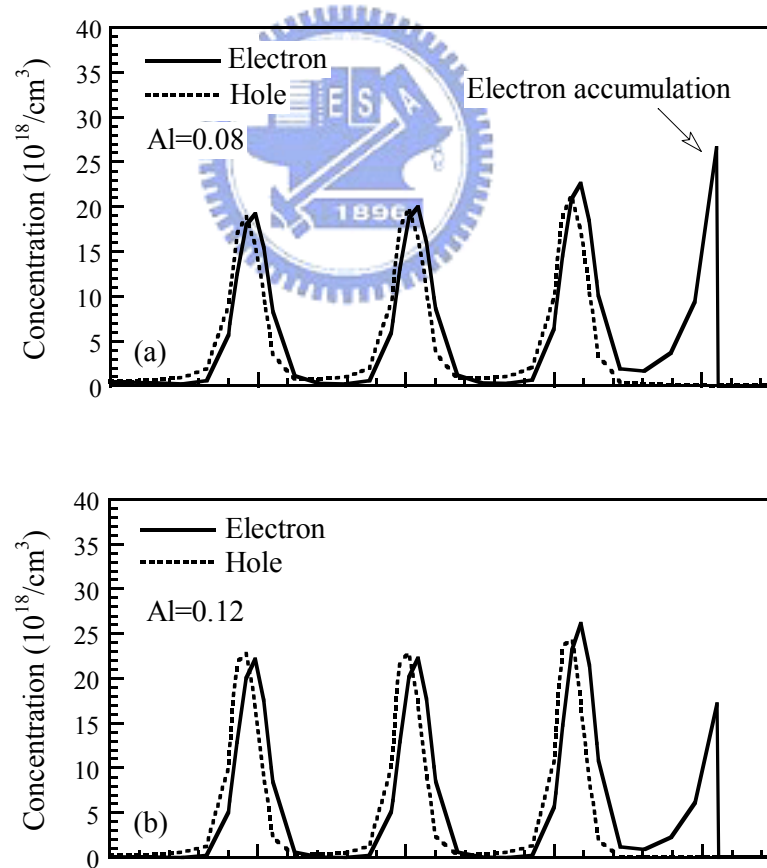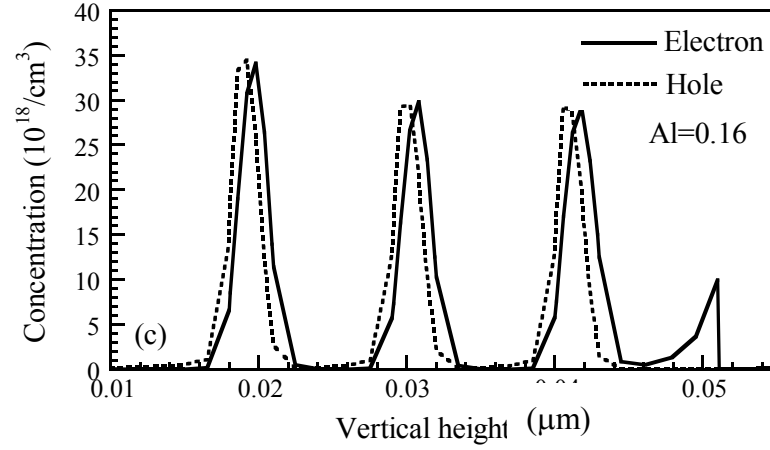
Fig. 3.7 The electron and hole concentration distribution in active region for the laser structures with a $Al_xGa_{1x}N$ barrier of (a) $x = 0.08$, (b) $x = 0.12$, and (c) $x = 0.16$ under an operation current of 400 mA

In addition to the effects of barrier height on the electron overflow and the non-uniform electron distribution, it is noteworthy that the energy barrier height created by $Al_{0.25}Ga_{0.75}N$ electronic blocking layer is substantially reduced by the high density of positive polarization charges at the interface between the $Al_xGa_{1x}N$ barrier layer and the $Al_{0.25}Ga_{0.75}N$ electronic blocking layer, as indicated in Table. 3.3 and Fig. 3.6.

This condition is more obvious for laser diode with $Al_{0.08}Ga_{0.92}N$ barrier. Under this condition, the electrons are attracted by Coulomb force and accumulate at this interface, which leads to strong band bending, as shown in Fig. 3.6 (a) and Fig. 3.7 (a). Consequently, the increase of laser threshold current will be expected due to the enhanced electron carrier leakage from active layer to p-type layer [101]. Moreover, the high density of positive polarization charges inhibits the injection of hole carriers into quantum wells. As for the injected holes in quantum wells, they will be attracted by the high density of electrons accumulated at this

55

interface. Because of these two mechanisms, hole concentration decreases from p-side quantum well to n-side quantum well gradually, which leads to the same trend for quantum-well interband gain, as evident in Fig. 3.5 (a), Fig. 3.6(a), and Fig. 3.7(a). In the case of the laser diode with $Al_{0.16}Ga_{0.84}N$ barrier, the density of positive polarization charges at this interface is relatively lower, which leads to lower electron accumulation at the interface between the $Al_{0.16}Ga_{0.84}N$ barrier layer and the $Al_{0.25}Ga_{0.75}N$ electronic blocking layer, as shown in Fig. 3.6(c) and Fig. 3.7(c). Therefore, the injection of hole carriers is easier than that of laser diode with $Al_{0.08}Ga_{0.92}N$ barrier. Furthermore, the injected holes in quantum wells are attracted by the accumulated electrons in the n-side quantum well, which results from the deeper well due to the higher aluminum composition in barrier layer. For these two reasons, hole concentration increases from p-side quantum well to n-side quantum well gradually, which leads to the same trend for quantum-well interband gain, as evident in Fig. 3.5(c), Fig. 3.6(c), and Fig. 3.7(c).

Fig. 3.8 depicts the percentage of electronic leakage current as a function of the bias current for the laser diodes with three-quantum-well active layers with a $Al_{x}Ga_{1-x}N$ barrier of $x = 0.08$, $x = 0.12$, and $x = 0.16$, respectively. The percentage of electron leakage current is defined as the ratio of the electron current overflowed to the p-type layer to that injected into the active region of the laser diodes. The percentage of electron leakage current increases with increasing input current and decreasing aluminum composition in barrier layers.
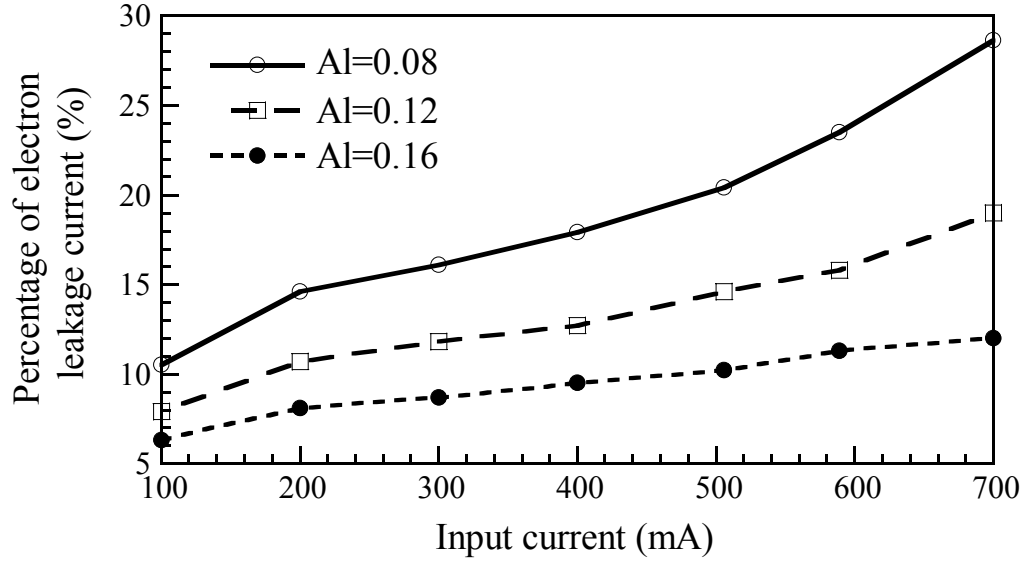
Fig. 3.8 The percentage of electronic leakage current as a function of the bias current for the laser diodes with three-quantum-well active layers with a $Al_xGa_{1x}N$ barrier of $x = 0.08$, $x = 0.12$, and $x = 0.16$, respectively

When the input current is below the threshold current values, which are about 200~250 mA, the leakage current rises obviously with input current. Nevertheless, when the input current is larger than the threshold current, the mechanism of stimulated emission occurs, which results in significant carrier recombination in quantum wells. Consequently, the increase of leakage current is suppressed as the input current is above the threshold current. Furthermore, the increase of the electron leakage current of the laser diode with $Al_{0.08}Ga_{0.92}N$ barrier layer is more obvious with the increasing input current as compared with that of the laser diode with $Al_{0.16}Ga_{0.84}N$ barrier layer. This result is attributed to the above reasons, such as barrier height and electron accumulation at the interface of barrier layer and electronic blocking layer. Fig. 3.9 shows 50% of the theoretically calculated interface charge densities at the $Al_xGa_{1x}N$/GaN (i.e., the interface between barrier layer and quantum well) and $Al_{0.25}Ga_{0.75}N$/$Al_xGa_{1x}N$ (i.e., the

interface between electronic blocking layer and barrier layer) interfaces as a function of the aluminum composition in barrier layer. The interface charge densities at the interface between $Al_{0.25}Ga_{0.75}N$ electronic blocking layer and $Al_xGa_{1-x}N$ barrier layer decrease with increasing aluminum composition in barrier layer. Therefore, the condition of band bending due to the high density of positive polarization charges at the $Al_{0.25}Ga_{0.75}N/Al_xGa_{1-x}N$ interface becomes less evident when the aluminum composition in barrier layer increases, as shown in Fig. 3.6. On the other hand, the interface charge densities at the interface between $Al_xGa_{1-x}N$ barrier layer and GaN quantum well increase with the barrier aluminum composition, as shown in Fig. 3.9.

In this situation, the built-in polarization causes a deformation of the quantum wells accompanied by a strong electrostatic field, as evident in Fig. 3.6 (c). Therefore, the separation of electrons and holes in the quantum well becomes more obvious with the increasing aluminum composition in barrier layer, as shown in Fig. 3.7(c). Under this circumstance, the photon emission rate will decrease significantly, which leads to the increase of laser threshold current.
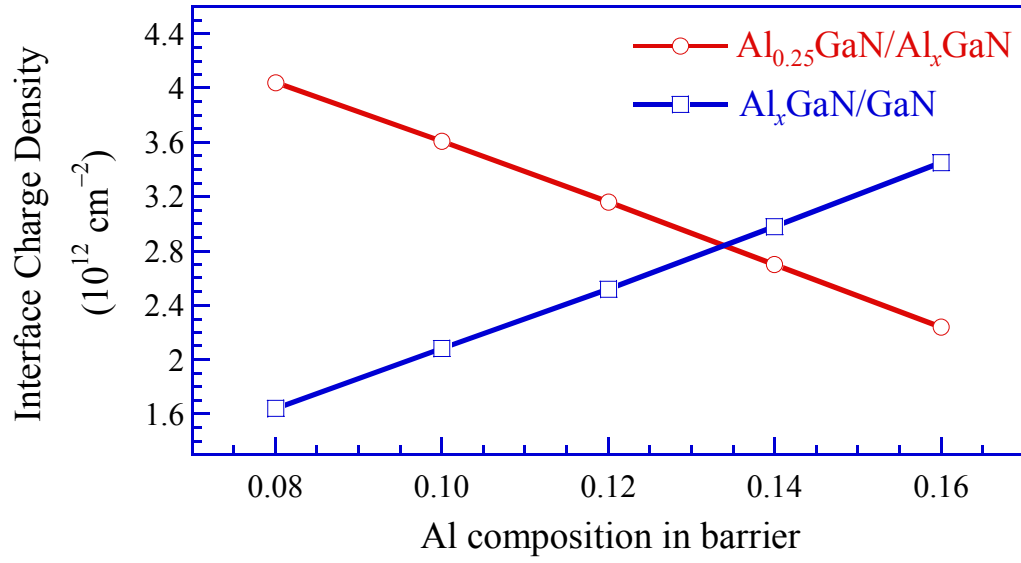
Fig. 3.9 50% of the theoretically calculated interface charge densities at the $Al_xGa_{1-x}N$/GaN (i.e., the interface between barrier layer and quantum well) and $Al_{0.25}Ga_{0.75}N$/$Al_xGa_{1-x}N$ (i.e., the interface between electronic blocking layer and barrier layer) interfaces as a function of the aluminum composition in barrier layer.

D.   Optical Confinement Factor

Except for the effects of electron leakage current, non-uniform electron distribution, and built-in polarization, optical confinement factor is also play an important role for the laser threshold properties. As the aluminum composition in the barrier/confining layer increases, the refractive index decreases simultaneously. Fig. 3.10 shows the quantum-well optical confinement factor versus quantum-barrier aluminum composition when the number of quantum well is three and the quantum-well thickness is 3 nm. The optical confinement factor decreases with the increasing aluminum composition in barrier layer due to the smaller difference of refractive index between confining layer and cladding layer. For the laser diode with $x = 0.08$, the optical wave intensity is mostly confined within the confining layers.

59
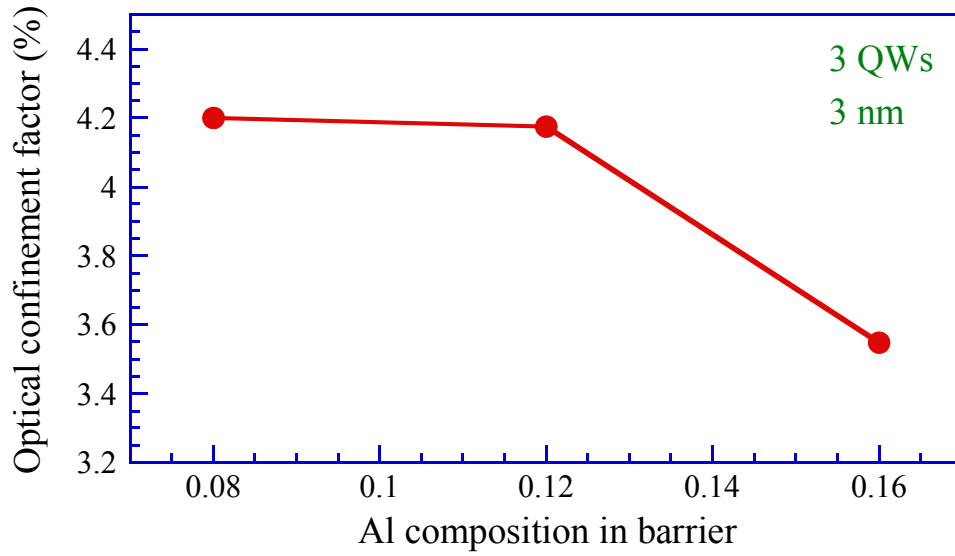
Fig. 3.10 The quantum-well optical confinement factor versus quantum-barrier aluminum composition when the number of quantum well is three and the quantum-well thickness is 3 nm

On the contrary, the optical wave intensity is spread into cladding layers as the barrier aluminum composition is 0.16, which leads to the lower optical confinement factor. Although the gain increases with barrier aluminum composition because of the enhanced carrier confinement, the change in confinement factor will decrease the modal gain provided by the laser structure. Therefore, the lower optical confinement factor is also an important role which results in the larger threshold current when the aluminum composition in barrier/confining layer increases.

E. *Thickness of the Quantum Well*

After investigating the internal physical mechanisms of the GaN/AlGaN laser diodes with different quantum-well numbers and quantum-barrier aluminum compositions, we will further

study the effect of quantum-well thickness on laser diode performance. The most nitride-based light-emitting devices are grown by employing relatively thin quantum wells due to the quantum confined Stark effect (QCSE) in the GaN-based quantum wells. The effect is induced by spontaneous and piezoelectric polarization, as discussed in section C. From the view point of the quantum-well structures, the radiative recombination rate is larger with decreasing quantum-well thickness due to the increasing electron-hole wave function overlap [105], [106]. Although the enhanced wave function overlap gives higher material gain for the laser diodes, the thinner quantum well will decrease the optical confinement factor. Fig. 3.11 shows the threshold current values of the laser diodes with different barrier aluminum compositions when the number of quantum wells varies from one to five. The quantum-well thickness is changed from 3 nm to 2 nm. In Fig. 3.11, it is found that the variation of the threshold current values of the laser diodes with 2-nm quantum wells has similar trend as compared with that of the laser diodes with 3-nm quantum wells. This result means that the competition of the above-mentioned physical mechanisms still dominates the threshold properties.
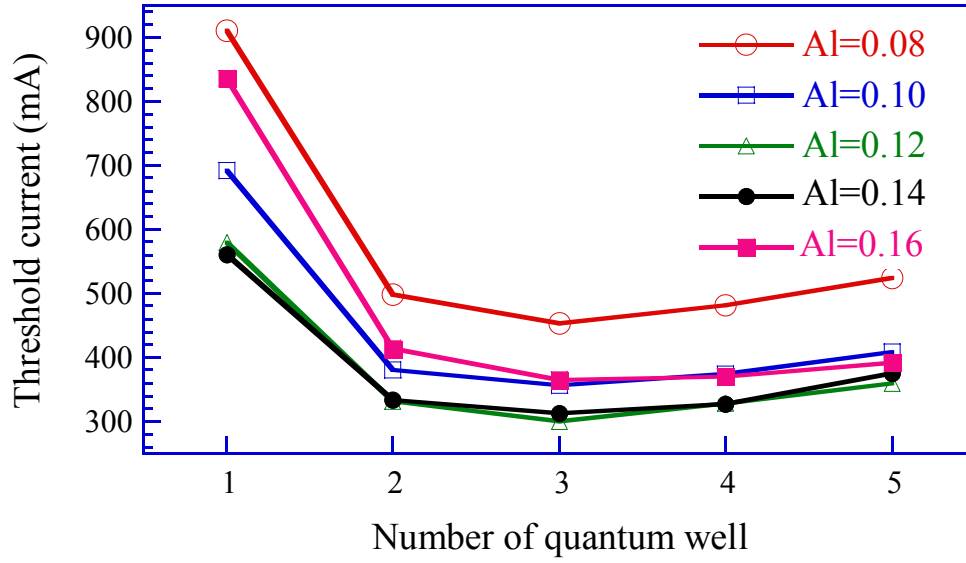
Fig. 3.11 The threshold current values of the laser diodes with different barrier aluminum compositions when the number of quantum wells varies from one to five and the quantum-well thickness is 2 nm

Furthermore, it is noteworthy that the threshold current values of the 2-nm quantum-well

laser diodes is larger than that of the 3-nm quantum-well laser diodes. This reason can be found

from Fig. 3.12, which shows the quantum-well optical confinement factor versus

quantum-barrier aluminum composition for the 2-nm GaN/AlGaN triple-quantum-well laser

diodes. By comparing Fig. 3.12 and Fig. 3.10, the lower optical confinement factor is one of the

most important factors which results in the higher threshold current of the laser diodes with

2-nm quantum wells. Besides, the thinner quantum well will induce larger electron leakage

current, which is observed in our calculation. As for the laser diodes with larger quantum-well

thickness than 3 nm, not presented here, the higher threshold current values are also found in

our simulation due to the increase of electron-hole wave function separation. Therefore, 3-nm

quantum-well thickness is optimal to balance the advantages of a large confinement factor against the disadvantages of QCSE for the ultraviolet laser diodes [82]. This quantum-well thickness is mostly employed in the nitride-based ultraviolet laser diodes [73], [79], [80], [82].
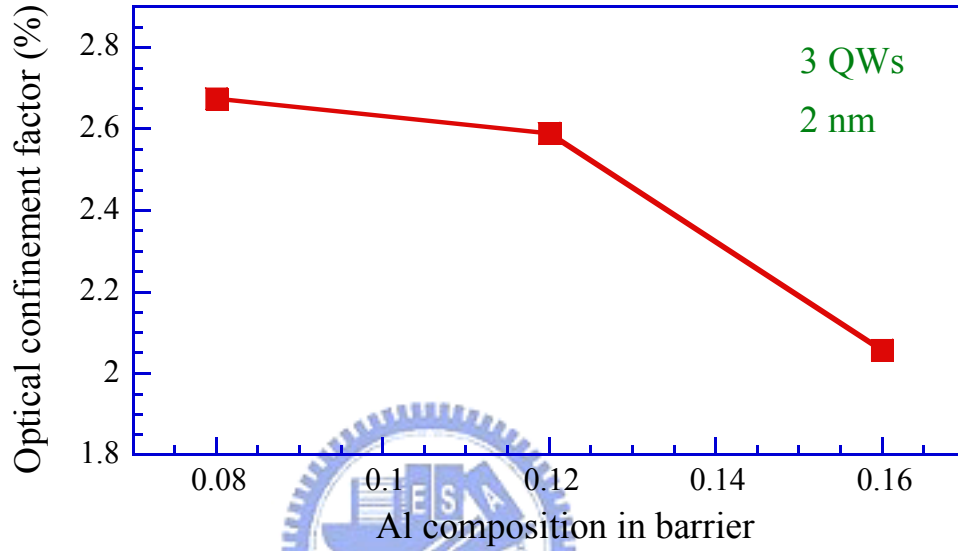
Fig. 3.12 The quantum-well optical confinement factor versus quantum-barrier aluminum composition for the 2-nm GaN/AlGaN triple-quantum-well laser diodes

3.4 Summary

We have done the theoretical simulation to investigate the effects of quantum-well number, quantum-barrier aluminum composition, and quantum-well thickness on the GaN/AlGaN multiple-quantum-well laser performance. The relations between the electron leakage currents and the active region structures, for different numbers of quantum well and aluminum compositions in the barrier/confining layers, are discussed and analyzed. The

simulation results indicate that, among the active layer structures under study, lower threshold

current can be achieved when the number of quantum wells is two or three and the aluminum

composition in barrier/confining layer is about 10~12%. Five different effects cause this result.

First, the severe electron leakage current is observed due to the lower barrier aluminum

composition and fewer number of quantum wells. Second, the obvious non-uniform

distribution of electron carriers is found due to the higher barrier aluminum composition and

the more number of quantum wells. Third, the higher density of positive polarization charges

at the interface between the $Al_xGa_{1-x}N$ barrier layer and the $Al_{0.25}Ga_{0.75}N$ electronic blocking

layer with decreasing barrier aluminum composition is also another important factor which

enhances the electron leakage current. Fourth, the interface charge density at the interface

between $Al_xGa_{1-x}N$ barrier layer and GaN quantum well increases with the barrier aluminum

composition, which lowers the photon emission rate. Fifth, the optical confinement factor

decreases with the increasing aluminum composition in barrier layer, which leads to the larger

threshold current. Therefore, the GaN/AlGaN laser diode with an active layer of two or three

quantum wells and $x = 0.10~0.12$ in the $Al_xGa_{1-x}N$ barrier/confining layer has found to be the

optimized active layer structure due to the competition of these five internal physical

mechanisms. Furthermore, the simulation results also indicate that the optimal quantum-well

thickness is about 3 nm due to the balance of the advantages of a large confinement factor

against the disadvantages of significant QCSE.

Chapter 4 Numerical Study on Optimization of Active Layer

Structures for InGaN/InGaN and InGaN/AlInGaN MQW

Laser Diodes

4.1 Paper Review

Recently, group III nitrides have attracted a great amount of attention because of their application in electronic and optoelectronic devices. It was from 1994, the use of InGaN/GaN double heterostructure (DH) in LEDs by Nakamura is thought to reignite the III-V nitride system. People did a lot of work in all aspects to improve the light emission efficiency including the material selection, crystal growth, and device manufacture process, etc. One of the difficulties hampering further advances in nitride emitters is the presence of large piezoelectric fields in these materials.

InGaN/GaN multiple quantum wells are a widely used material and structure to serve as the active layer in nitride heterostructures for its advantage in easy tuning wavelength through controlling the composition of indium. However conventional InGaN/GaN quantum wells grown along the crystallographic c-axis exhibit an internal spontaneous and piezoelectric field in the MV/cm range. The spontaneous field is induced from different atoms arrange in one direction parallel with the growth axis while the piezoelectric field is caused by biaxial

compressive strain due to the lattice mismatch between InGaN and GaN.

Under this circumstance, electrons and holes are drawn to opposite interfaces of the QW and the spatial separation of wave functions suppresses radiative recombination with respect to nonradiative recombination, diminishing the emission efficiency drastically. All the effects caused by the build in electiric field are called as Quantum Confined Stark Effect (QCSE). In order to overcome the problem, nonpolar structure was thought as a method to eliminate the built in polarization field. Waltereit and colleagues at the Paul Drude Institute in Berlin first demonstrated the absence of the piezoelectric field in m-plane GaN/AlGaN QWs grown on LiAlO$_2$ substrates.

For the past few years, many group have announced several results on nonpolar structures. Growth of m-plane GaN(1 -1 00) onγ-LiAlO2(1 0 0) was reported by P. Waltereit *et al.* in 2000.[107] Nonpolar (11-2 0) a-plane GaN thin films grown on (1-1 0 2) r-plane sapphire was published by S. P. Denbaars *et al.* in 2002. [108] Recently, *a*-plane InGaN/GaN multiple quantum wells grown on *r*-plane sapphire by metal organic chemical vapor deposition (MOCVD) was announced by T. S. Ko *et al.* [109] in 2007. In the same year, S. Nakamura *et al.* realized nonpolar m-plane InGaN/GaN multiple-quantum-well laser diodes with emission wavelengths 405.5 nm at threshold current density as low as 7.5 kA / cm^2 and continuous-wave operation of m-plane InGaN multiple quantum well laser diodes with the

lasing wavelengths approximately 400 nm at 4.0 kA / cm^2 was also demonstrated. [110],[111]

In addition to the nonpolar structure, we discuss another method to eliminate QCSE in this chapter. As far as we know, QCSE caused by the spontaneous and the piezoelectric field induces the electrical field in the active region. Hence, we try to use different compositions of aluminum and indium in AlInGaN barrer layer for this purpose. First of all, quaternary (AlInGaN) is used to replace the conventional ternary (InGaN) or binary compound (GaN) of the quantum-barrier layer used in the structure of laser diodes. The bandgap energies of the quaternary compounds in the quantum-barrier will be chosen similarly the ternary ones. These chosen quaternary materials can eliminate QCSE, and these results will be shown in the following section.
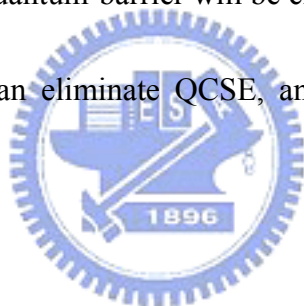
Applying AlInGaN in the quantum-barrier layer to enhance the performance of light-emitting devices has been proposed by several research groups. M. E. Aumer *et al.* reported the luminescence properties of AlInGaN/InGaN quantum well structures in 2000. [112] W. C. Lai *et al.* published the AlInGaN/InGaN MQW LEDs in 2001. [113] Their observations all suggest that employing the quaternary AlInGaN in barrier layer can improve the properties of nitride-based LEDs. Except for the blue MQW LEDs, this AlInGaN/InGaN quantum-well structure can also be utilized in the ultraviolet (UV) LEDs. The experimental results were demonstrated by J. Lee *et al.* and S. H. Baek *et al.,* respectively. [114],[115]

However, their concepts were based on utilizing different AlInGaN composition to match the lattice constant of well layer. In this chapter, we discuss not only the lattice-matched issue but also to eliminate spontaneous effect and piezoelectric field with AlInGaN in the quantum-barrier layer. The results are shown in the following sections.

4.2 Theoretical Model & Structure and Parameters of InGaN/InGaN & InGaN/AlInGaN LDs

In order to achieve high-performance GaN-based laser diodes, systematic and compact theoretical modeling is a necessary approach to improve the existing laser structures and to understand the internal physical processes, which provides the timely and efficient guidance toward the optimal structure design and device parameters. By performing computational simulations, we can expect the trend of device design and understand the main physical factor which limits the performance of GaN-based laser diodes. The self-consistent LASTIP simulation program combines band structure and gain calculations with 2-D simulations of wave guiding, carrier transport, and heat flux. The carrier-transport model includes drift and diffusion of electrons and holes in devices. The built-in polarization induced by spontaneous and piezoelectric polarizations is considered at heterointerfaces of nitride-related devices. In the quantum wells, self-consistent Poisson and Schrödinger equations were recomputed at

every bias point for the states of quantum-well levels and carrier distributions. The physical model of the strained InGaN quantum wells is considered in such a way that the conduction bands are assumed to be parabolic, and the valence-band structures, which include the coupling of the heavy-hole, the light-hole, and the spin-orbit split-off bands, are calculated by the 6 x 6 Hamiltonian with an envelop function approximation. Free-carrier gain model, including a Lorentzian broadening function with a 0.1-ps scattering time, is used in calculating the optical gain of the quantum wells.

In this simulation, we first assume that the InGaN laser diode is grown on an n-type GaN layer that is 3.0 μm in thickness. On top of this GaN layer are a 0.1-μm-thick n-type $In_{0.1}Ga_{0.9}N$ compliant layer and a 1.0-μm-thick n-type $Al_{0.07}Ga_{0.93}N$ cladding layer, followed by a 0.1-μm-thick n-type GaN guiding layer. The multiple-quantum-well active region consists of two 2-nm-thick $In_{0.1}Ga_{0.9}N$ quantum wells and 5-nm-thick $In_{0.035}Ga_{0.965}N$ barriers or 5-nm-thick AlInGaN barriers. A 20-nm-thick p-type $Al_{0.2}Ga_{0.8}N$ is grown on top of the active region to reduce an electron leakage into the p-type GaN layer. Furthermore, a 0.1-μm-thick p-type GaN guiding layer and a 1.0-μm-thick p-type $Al_{0.07}Ga_{0.93}N$ cladding layer are grown. Finally, a 0.1-μm-thick p-type GaN cap layer is grown to complete the structure. The illustration of the device structure is shown in Fig. 4.1.

p-contact

0.1-μm p-GaN

1-μm p-Al$_{0.07}$Ga$_{0.93}$N

0.1-μm p – GaN

p- Al$_{0.2}$Ga$_{0.8}$N blocking   0.02-μm

barrier : i-In$_{0.035}$Ga$_{0.965}$N   5-nm

MQW X 2

QW : i-In$_{0.1}$Ga$_{0.9}$N   2-nm

0.1-μm n – GaN

n-contact

1-μm n – Al$_{0.07}$Ga$_{0.93}$N

0.1-μm   n – In$_{0.1}$Ga$_{0.9}$N

n – GaN   3-μm
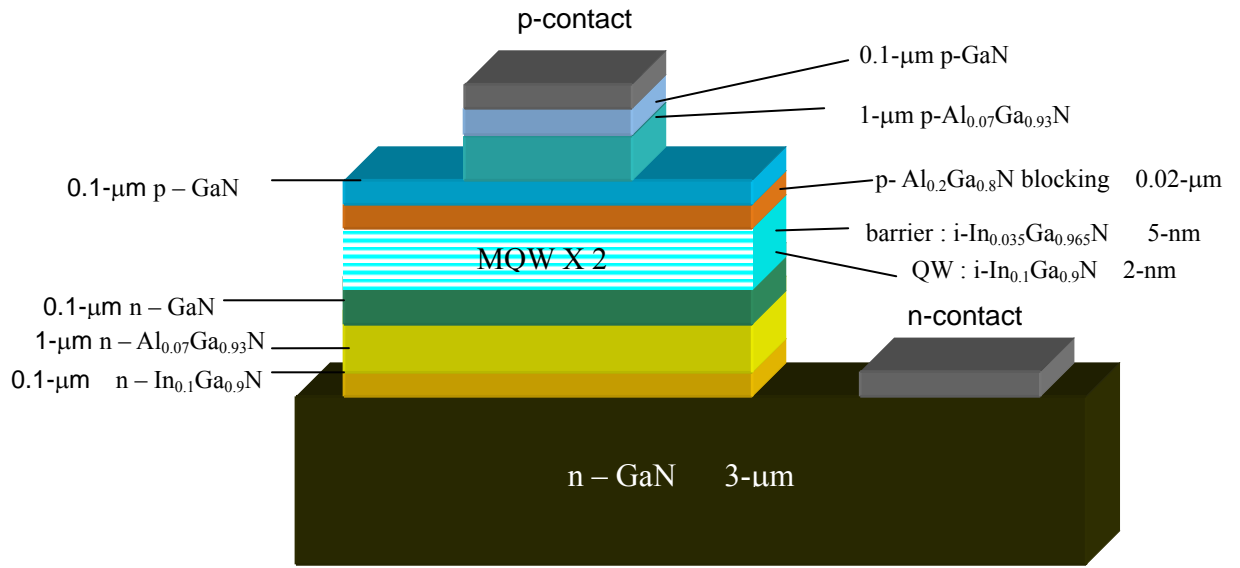
Fig. 4.1 The illustration of the device structure

(Note: utilize AlInGaN to replace the barrier layer for new structure)

The effective active region of the ridge geometry is 2 μm in width and 500 μm in length.

The reflectivities of the two end mirrors are set at 20% and 50%, respectively. The doping

concentrations in each layer and the detailed device structure are described in Table. 4.1.

Table 4.1 The doping concentrations and the refractive index in each layer and the detailed device structure (Note: utilize AlInGaN to replace the barrier layer for new structure)

Parameter (unit)	d (nm)	$N_{dop}(1/cm^3)$	n
p-GaN (contact)	100	1×10^{18}	2.55
p-Al$_{0.07}$Ga$_{0.93}$N (cladding)	1000	5×10^{17}	2.519
p-GaN (waveguide)	100	5×10^{17}	2.55
p-Al$_{0.2}$Ga$_{0.8}$N (EBL)	20	5×10^{17}	2.489
i-In$_{0.035}$Ga$_{0.965}$N (barrier)	5	--	2.585
i-In$_{0.1}$Ga$_{0.9}$N (quantum well)	2	--	3.835
i-In$_{0.035}$Ga$_{0.965}$N (barrier)	5	--	2.585
i-In$_{0.1}$Ga$_{0.9}$N (quantum well)	2	--	3.835
i-In$_{0.035}$Ga$_{0.965}$N (barrier)	5	--	2.585
n-GaN (waveguide)	100	1×10^{18}	2.55
n-Al$_{0.07}$Ga$_{0.93}$N (cladding)	1000	1×10^{18}	2.519
n-In$_{0.1}$Ga$_{0.9}$N (compliance)	100	1×10^{18}	2.835
n-GaN (substrate)	3000	1×10^{18}	2.55

Proper material parameters are essential to obtain correct simulation results. As for AlInGaN materials, a linear interpolation between the parameters of the relevant binary semiconductors is utilized except for the bandgap energies. For physical parameter P, the interpolation formula is [116]

$$P(Al_x In_y Ga_{1-x-y}N) = P(AlN)x + P(InN)y + P(GaN)(1-x-y) .$$

(4.1)

The AlInGaN bandgap energies can be expressed as a weighted sum of the bandgap energies of relevant ternary semiconductors with appropriate bandgap-bowing parameters. Specifically, the AlInGaN bandgap energy is calculated by the following expressions. [117]

$$E_g(AlInGaN) = \frac{xy \cdot E_g^u(AlInN) + yz \cdot E_g^v(InGaN) + zx \cdot E_g^w(AlGaN)}{xy + yz + zx} \tag{4.2}$$

$$E_g^u(AlInN) = u \cdot E_g(InN) + (1-u) \cdot E_g(AlN) - b_{AlInN} \cdot u \cdot (1-u), \tag{4.3}$$

$$E_g^v(InGaN) = v \cdot E_g(GaN) + (1-v) \cdot E_g(InN) - b_{InGaN} \cdot v \cdot (1-v), \tag{4.4}$$

$$E_g^w(AlGaN) = w \cdot E_g(GaN) + (1-w) \cdot E_g(AlN) - b_{AlGaN} \cdot w \cdot (1-w), \tag{4.5}$$

$$u = \frac{1-x+y}{2} \quad v = \frac{1-y+z}{2} \quad w = \frac{1-x+z}{2}, \tag{4.6}$$

where x, y, $z = 1 - x - y$ and represent the compositions of aluminum, indium, and gallium in the AlInGaN material system, respectively. The bandgap-bowing parameters of AlInN, InGaN, and AlGaN are 2.5, 1.4, and 0.7 eV, respectively. [118]

The built-in polarization induced due to spontaneous and piezoelectric polarizations is known to influence the performance of nitride devices. In order to consider the built-in polarization within the interfaces of nitride devices, the method developed by Fiorentini *et al.*

is employed to estimate the built-in polarization, which is represented by fixed interface

charges at each heterointerface. They provide explicit rules to calculate the nonlinear

polarization for nitride alloys of arbitrary composition [119]. Specifically, the spontaneous

polarization of ternary nitride alloys can be expressed by

$$P_{sp}(Al_xGa_{1-x}N) = -0.090x - 0.034(1-x) + 0.019x(1-x), \tag{4.7}$$

$$P_{sp}(In_xGa_{1-x}N) = -0.042x - 0.034(1-x) + 0.038x(1-x), \tag{4.8}$$

and $\quad P_{sp}(Al_xIn_{1-x}N) = -0.090x - 0.042(1-x) + 0.071x(1-x). \tag{4.9}$

The spontaneous polarization of the quaternary AlInGaN can be calculated in a similar

way as that shown in (4.2). As for the piezoelectric polarization of AlInGaN, InGaN, and

AlGaN, it can be calculated by the following expression.

$$P_{pz}(Al_xIn_yGa_{1-x-y}N) = P_{pz}(AlN)x + P_{pz}(InN)y + P_{pz}(GaN)(1-x-y) \tag{4.10}$$

where

$$P_{pz}^{AlN} = -1.808\varepsilon(x) + 5.624\varepsilon(x)^2 \quad for \ \varepsilon < 0 \tag{4.11}$$
$$P_{pz}^{AlN} = -1.808\varepsilon(x) - 7.888\varepsilon(x)^2 \quad for \ \varepsilon > 0 \tag{4.12}$$
$$P_{pz}^{GaN} = -0.918\varepsilon(x) + 9.541\varepsilon(x)^2 \tag{4.13}$$

$$P_{pz}^{InN} = -1.373\varepsilon(x) + 7.559\varepsilon(x)^2 \tag{4.14}$$

$$\varepsilon = (a_{subs} - a_L)/a_L \tag{4.15}$$

where a_{subs} and a_L are the lattice constants of the substrate and epitaxial layer, respectively. The total built-in polarization is the sum of spontaneous and piezoelectric polarizations. At an abrupt interface of a top/bottom layer heterostructure such as InGaN/GaN or AlGaN/GaN, the polarization can decrease or increase within a bilayer, causing a fixed polarization charge density σ defined by [120]

$$\begin{aligned}
\sigma(P_{sp} + P_{pz}) &= P(bottom) - P(top) \\
&= \left[P_{sp}(bottom) + P_{pz}(bottom) \right] - \left[P_{sp}(top) + P_{pz}(top) \right]
\end{aligned} \tag{4.16}$$
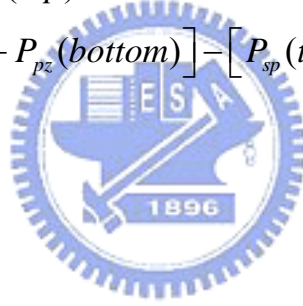
Table 4.2 Net surface charge density at each interface of the InGaN LD

Interface	Built-in charge density
$Al_{0.07}Ga_{0.93}N/GaN$	+2.86 x 10^{12} cm^{-2}
$GaN/Al_{0.2}Ga_{0.8}N$	-8.82 x 10^{12} cm^{-2}
$Al_{0.2}Ga_{0.8}N/In_{0.035}Ga_{0.965}N$	+1.20 x 10^{13} cm^{-2}
$In_{0.035}Ga_{0.965}N/In_{0.1}Ga_{0.9}N$	+6.46 x 10^{12} cm^{-2}
$In_{0.1}Ga_{0.9}N/ In_{0.035}Ga_{0.965}N$	-6.46 x 10^{12} cm^{-2}
$In_{0.035}Ga_{0.965}N/GaN$	-3.19 x 10^{12} cm^{-2}
$GaN/Al_{0.07}Ga_{0.93}N$	-2.86 x 10^{12} cm^{-2}

For the InGaN quantum-well lasers under study, the net surface charges at all interfaces are calculated and listed in Table. 4.2. Although the interface charges can be obtained by this theoretical model, experimental investigations often find a weaker built-in polarization than that predicted by theoretical calculation. It is mainly attributed to partial compensation of the built-in polarization by defect and interface charges [121]. Typical reported experimental values are 20%, 50%, or 80% smaller than the theoretically calculated values [122]–[124]. As a result, 40% of the theoretical polarization values are used in our simulation to study the effects of built-in polarization on the laser performance.

4.3 Conventional InGaN/InGaN LDs & InGaN/AlInGaN LDs

First of all, conventional InGaN/InGaN LDs have a big problem, which is called QCSE

mentioned in the preceding section. This effect causes wavefunction of the electrons and the

holes separating in the space and also reduces the recombination rate of the carriers. We can

see the phenomenon in Fig. 4.2 (a). In order to improve the disadvantage, we replace the

ternary alloy ($In_{0.035}Ga_{0.965}N$) with the quaternary alloy (AlInGaN) in the quantum-barrier

layer. Moreover, the compositions of the aluminum and indium of the quaternary alloy should

be decided. First, we consider the bandgap energy should be similar to the bandgap energy of

the ternary barrier layer and another issue is to match the interface charge density between

barrier layer and quantum well layer, which can help to eliminate the spontaneous effect and

the piezoelectric field. Hence, we can obtain the quaternary material ($Al_{0.25}In_{0.226}GaN$) whose

bandgap energy is 3.204 eV and the bandgap energy of the $In_{0.035}Ga_{0.965}N$ is 3.297 eV. The

bandgap energy values of the $Al_{0.25}In_{0.226}GaN$ and the $In_{0.035}Ga_{0.965}N$ can be calculated by (4.2)

and (4.4), respectively. We can see that the overlap of the wave function in Fig. 4.2 (b) is

better than in Fig. 4.2 (a).
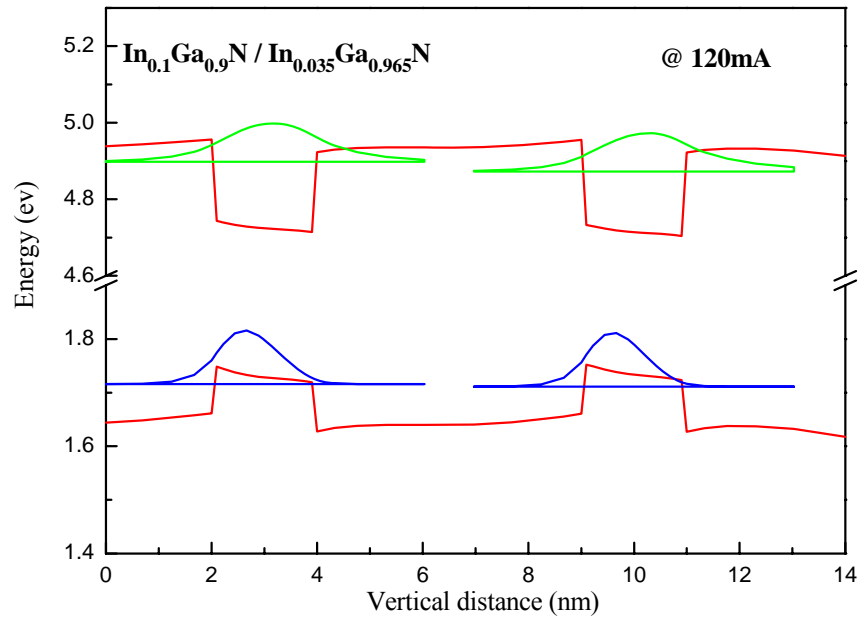
(a)
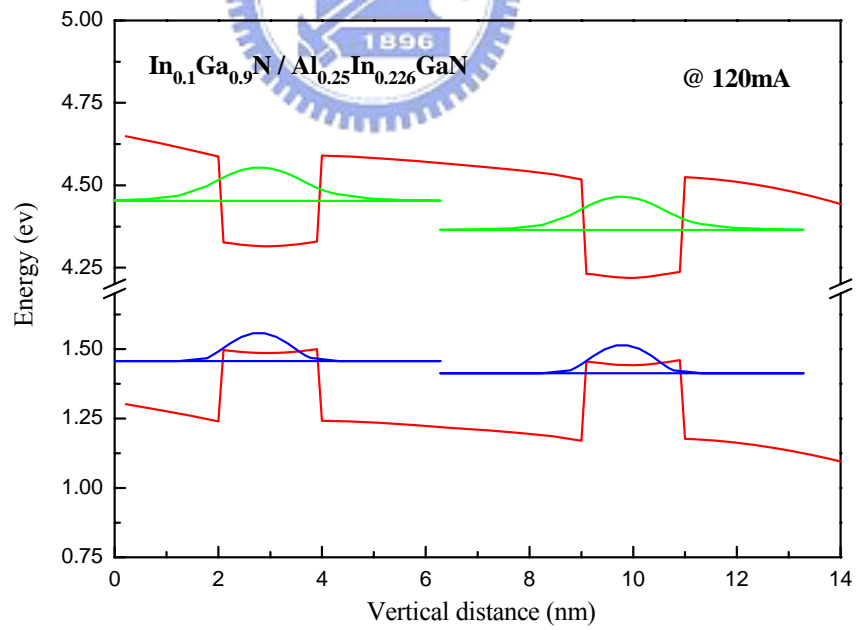
(b)

Fig. 4.2 (a) The wavefunction of the In0.1Ga0.9N/In0.035Ga0.965N LD in the
quantum well. (b) The wavefunction of the
In0.1Ga0.9N/A0.25lIn0.226GaN LD in the quantum well

The laser output power of $In_{0.1}Ga_{0.9}N/In_{0.035}Ga_{0.965}N$ and $In_{0.1}Ga_{0.9}N /Al_{0.25}In_{0.226}GaN$ laser diodes as a function of input current is shown in

Fig. 4.3. The performance of the structure is improved obviously. The threshold current and the slope efficiency of the $In_{0.1}Ga_{0.9}N/Al_{0.25}In_{0.226}GaN$ LD are 81.41 mA and 0.142 W/A, respectively. The threshold current and the slope efficiency of the $In_{0.1}Ga_{0.9}N/In_{0.035}Ga_{0.965}N$ LD are 110.90 mA and 0.296 W/A, respectively.
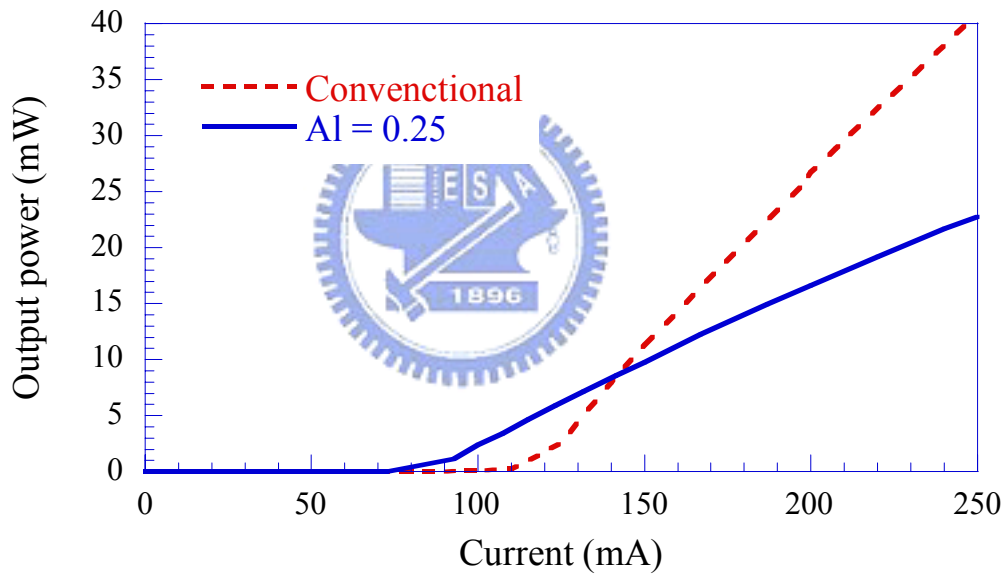
Fig. 4.3 The laser output power of the $In_{0.1}Ga_{0.9}N/In_{0.035}Ga_{0.965}N$ and the $In_{0.1}Ga_{0.9}N/Al_{0.25}In_{0.226}GaN$ laser diodes structure as a function of input current

However, in Fig. 4.3, it is found that the slope efficiency is lower than that of InGaN/InGaN laser diode. It is worthy to note that the positive interface charge density makes the band bending between the blocking layer and the barrier layer, which causes the lower barrier height in the blocking layer and results in large electron current overflows especially

for $In_{0.1}Ga_{0.9}N/Al_{0.25}In_{0.226}GaN$ laser diode, as shown in Fig. 4.4. Furthermore, there is an

unexpected barrier height between the waveguide layer and the barrier layer, as indicated in

Fig. 4.4 (b). It makes current inject into the quantum well relatively difficultly.
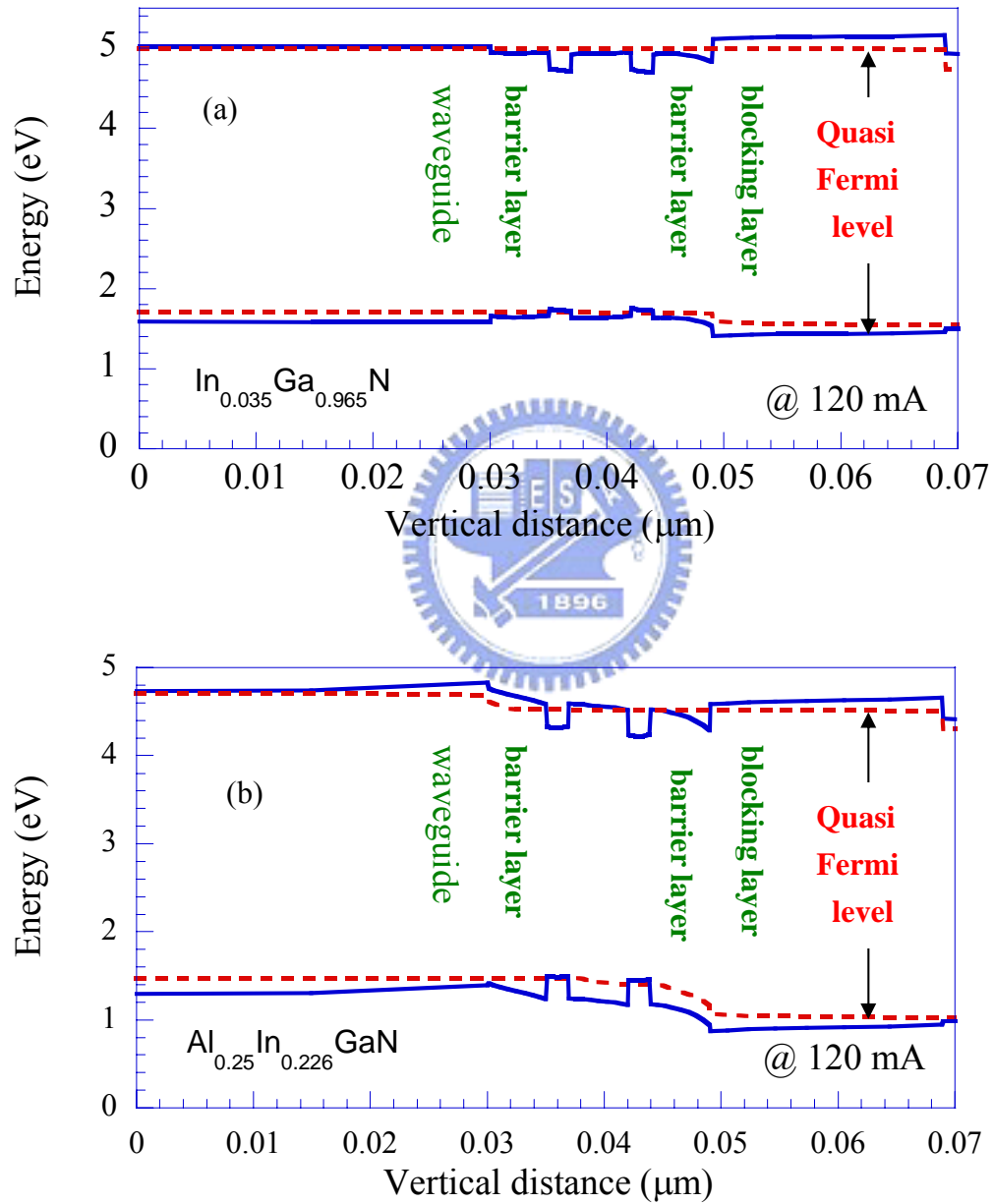
Fig. 4.4 (a) The band diagram of the InGaN/InGaN MQW LD (b) The band diagram of the InGaN/AlInGaN MQW LD

Fig. 4.5 depicts the percentage of electron leakage current at different input current. We can find that the overflow ratio is obviously higher for the laser diode using $Al_{0.25}In_{0.226}GaN$ than using $In_{0.035}Ga_{0.965}N$ in the quantum barrier layer. This is the main reason which results in the lower slope efficiency in the $InGaN/Al_{0.25}In_{0.226}GaN$ LD. In order to improve the drawbacks, the laser diodes with different AlInGaN barrier layers will be discussed in the following section.
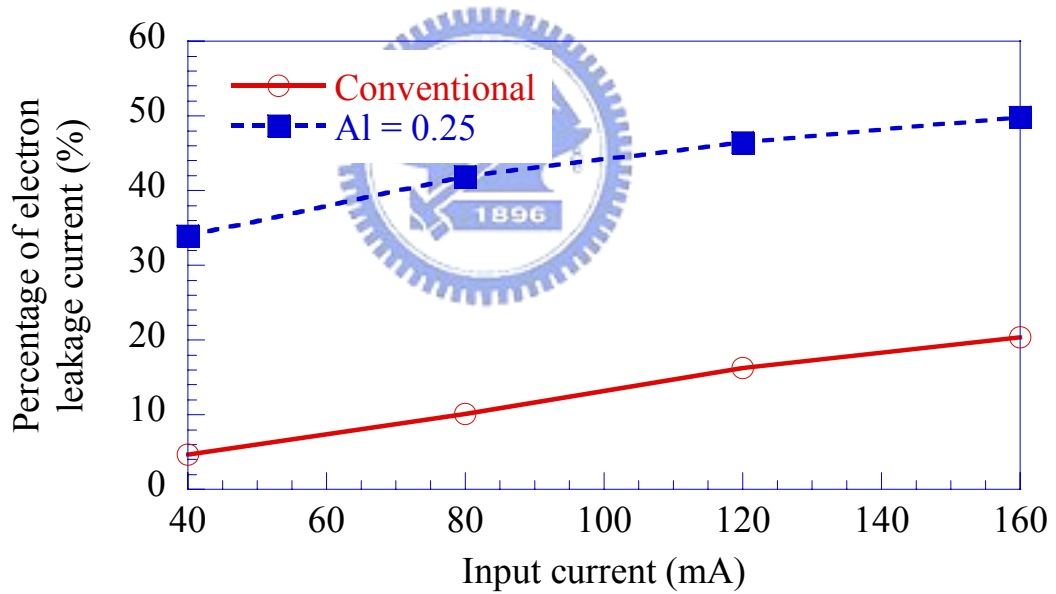
Fig. 4.5 The percentage of electron leakage current at different input current

4.4 Optimization of InGaN LDs with Quaternary AlInGaN Barrier Layer

In order to further study the optimization of InGaN LDs with quaternary AlInGaN barrier layer, we find another four quaternary alloys used in barrier layer, including $Al_{0.20}In_{0.207}GaN$, $Al_{0.15}In_{0.188}GaN$, $Al_{0.10}In_{0.169}GaN$, and $Al_{0.05}In_{0.150}GaN$. The laser output power of the InGaN/AlInGaN laser diodes structure with different barrier aluminum and indium compositions as a function of input current is shown in Fig. 4.6.
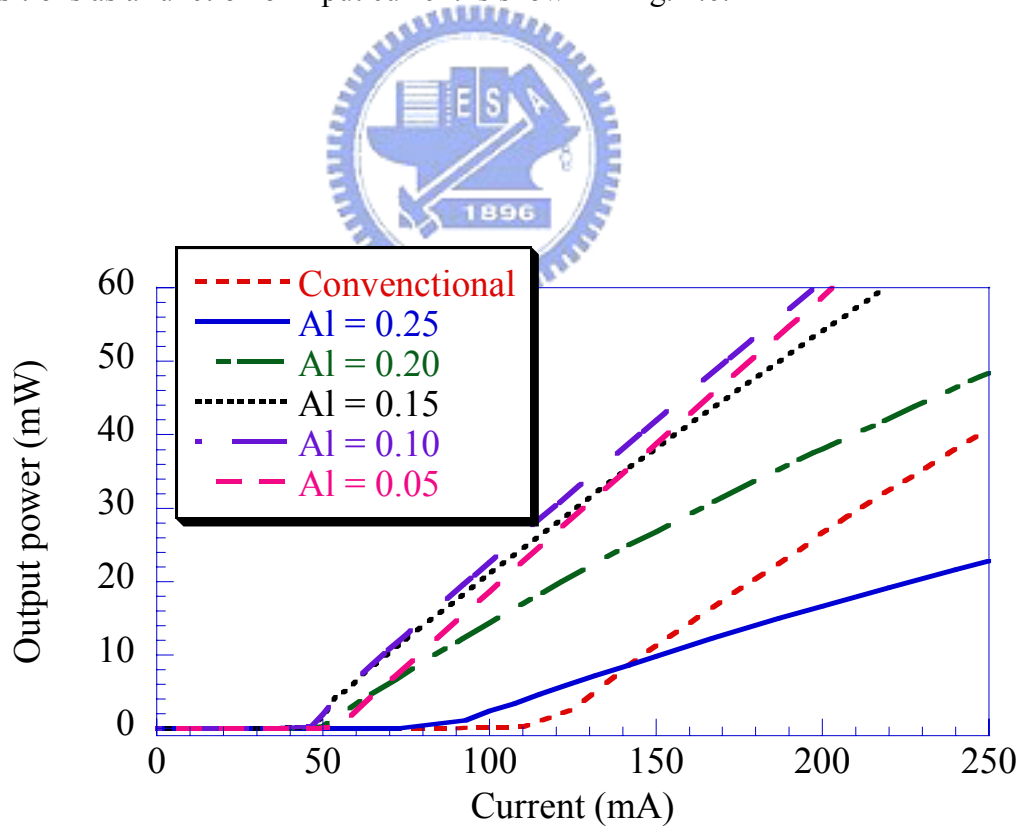
Fig. 4.6 The laser output power of the InGaN/AlInGaN laser diodes structure as a function of input current

According to the simulation results, optimal barrier aluminum composition is about 10~ 15% for the InGaN/Al$_x$In$_y$Ga$_{1-x-y}$N quantum-well lasers, as shown in Fig. 4.7 (a). However, lower aluminum compositions in AlInGaN barrier layer have higher slope efficiency, as shown in Fig. 4.7 (b). At the same time, we can find that lower and higher aluminum compositions in Al$_x$In$_y$Ga$_{1-x-y}$N barrier layer result in larger threshold current values. All possible internal physical mechanisms which lead to these results will be discussed and analyzed in detail in the following section.
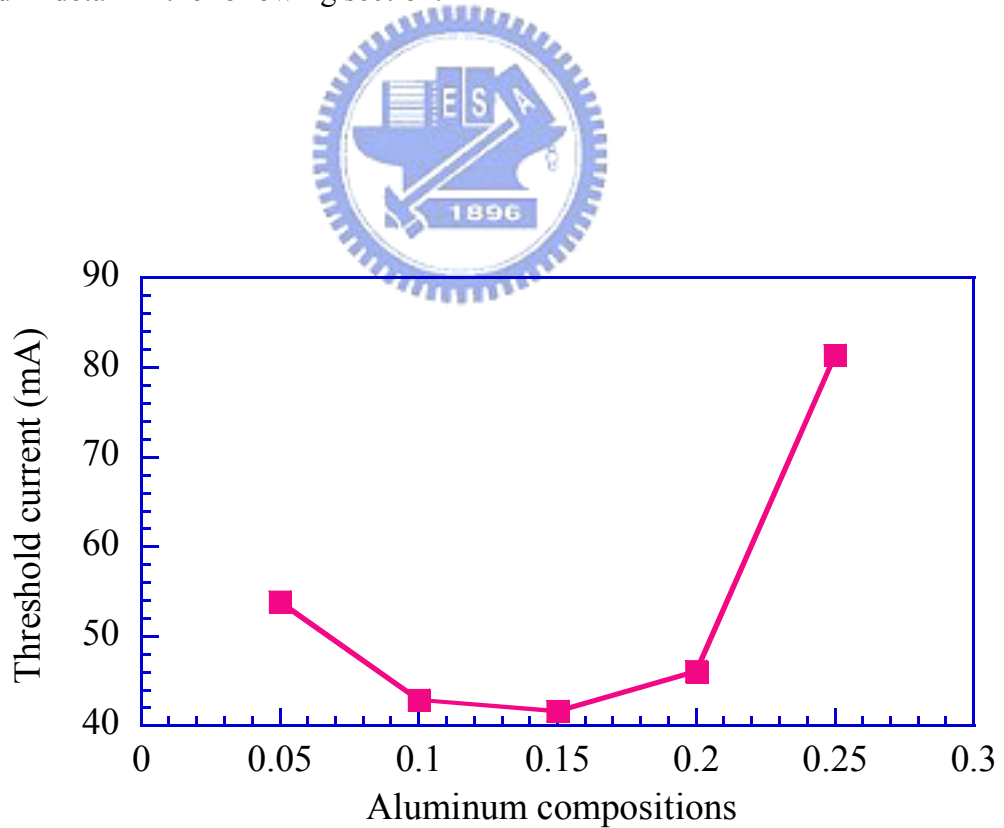
(a)
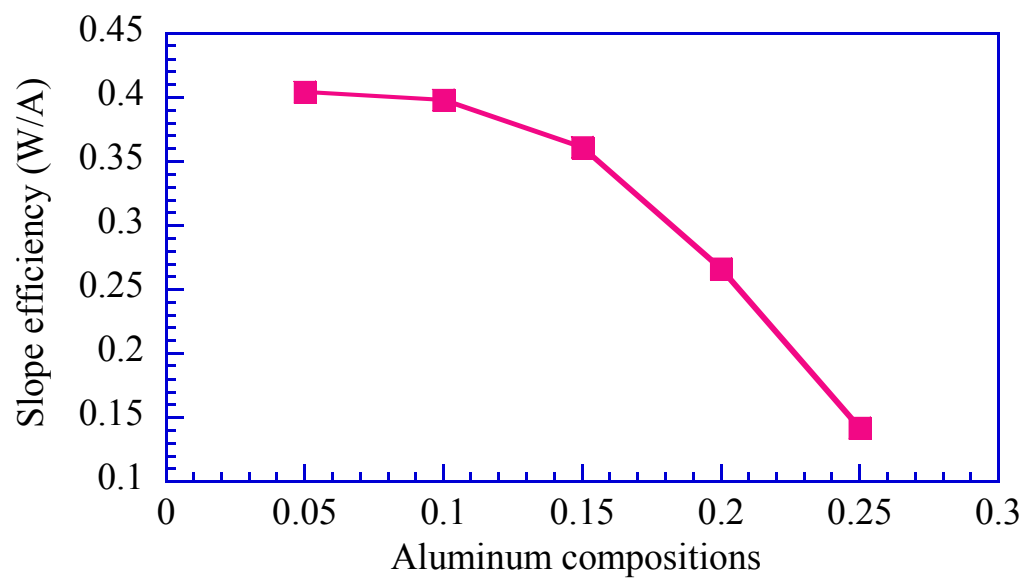
(b)

Fig. 4.7 (a) The threshold current values with different aluminum compositions (b)
The slope efficiency with different aluminum compositions

4.5 Physical Mechanisms Discussions

A. Electron Leakage Current

In order to understand the internal physical mechanisms which result in the worst laser performance in the cases of higher barrier aluminum composition, the vertical electron current density profiles within the active regions of laser structures with $Al_{0.25}In_{0.226}GaN$, $Al_{0.15}In_{0.188}GaN$, and $Al_{0.05}In_{0.150}GaN$ barrier layers, respectively, are plotted in Fig. 4.8 at 120 mA injection current. This driving current is chosen to be above the threshold current values of the laser diodes under study. The positions of two quantum wells are marked with gray areas. The left-hand side of the figure is the n-side of the device. The electron current is injected from n-type layers into quantum wells and recombines with holes in quantum wells.
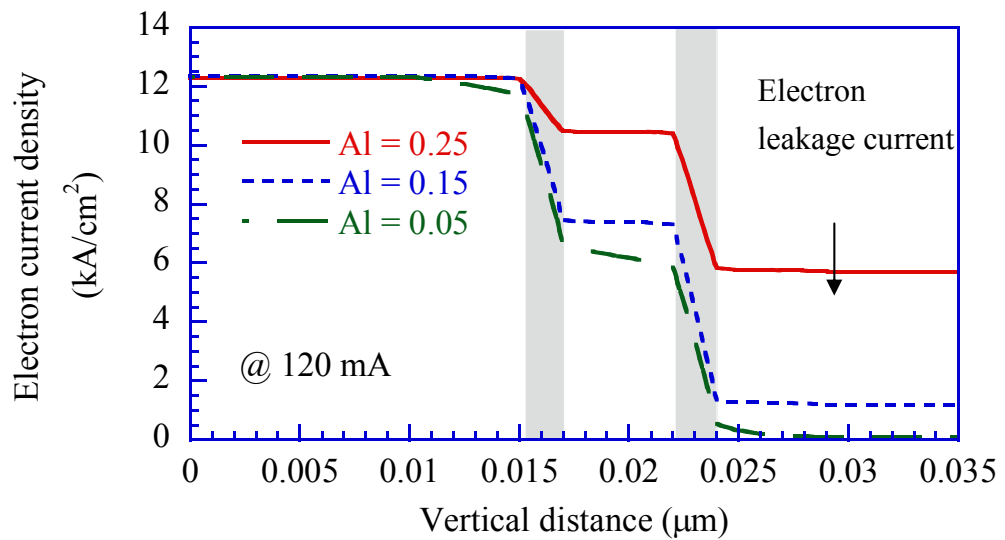
Fig. 4.8 The vertical electron current density profiles within the active regions of laser structures with $Al_{0.25}In_{0.226}GaN$, $Al_{0.15}In_{0.188}GaN$, and $Al_{0.05}In_{0.150}GaN$ barrier layers, respectively, at 120 mA injection current

Therefore, the electron current density is reduced in the quantum wells. Electron current which overflows through quantum wells is viewed as leakage current. On the contrary, when the barrier aluminum composition decreases from 25% to 5%, better electron confinement is provided and electron leakage current is hardly observed. And these values of the electron current overflow ratio at 120 mA injection current are shown in Table. 4.3.

Meanwhile, we can explain why the slope efficiency values become higher as the aluminum compositions decrease. When the electron current overflow ratio become lower, it means there is higher slope efficiency values.

Table 4.3 The electron current overflow ratio at 120 mA injection current

Barrier layer	Overflow ratio (%) @ 120mA
$Al_{0.25}In_{0.226}GaN$	46.47
$Al_{0.20}In_{0.207}GaN$	24.46
$Al_{0.15}In_{0.188}GaN$	9.65
$Al_{0.10}In_{0.169}GaN$	3.20
$Al_{0.05}In_{0.150}GaN$	0.78

B. Carrier Confinement

Fig. 4.9 depicts the conduction band and the interband gain in the quantum well at 120 mA injection current for the laser diodes with an $Al_xIn_yGa_{1-x-y}N$ barrier of $x = 0.25$, $x = 0.15$, and $x = 0.05$, respectively. Obviously, the carrier confinement in the quantum well increases with increasing aluminum composition in barrier layers. However, in addition to the carrier confinement in the quantum well, we also find that the barrier height at the interface between the barrier layer and the blocking layer becomes lower with increasing aluminum composition in the barrier layers. At the same time, this physical mechanism causes more electron current overflow, and makes the laser diodes have higher threshold current.
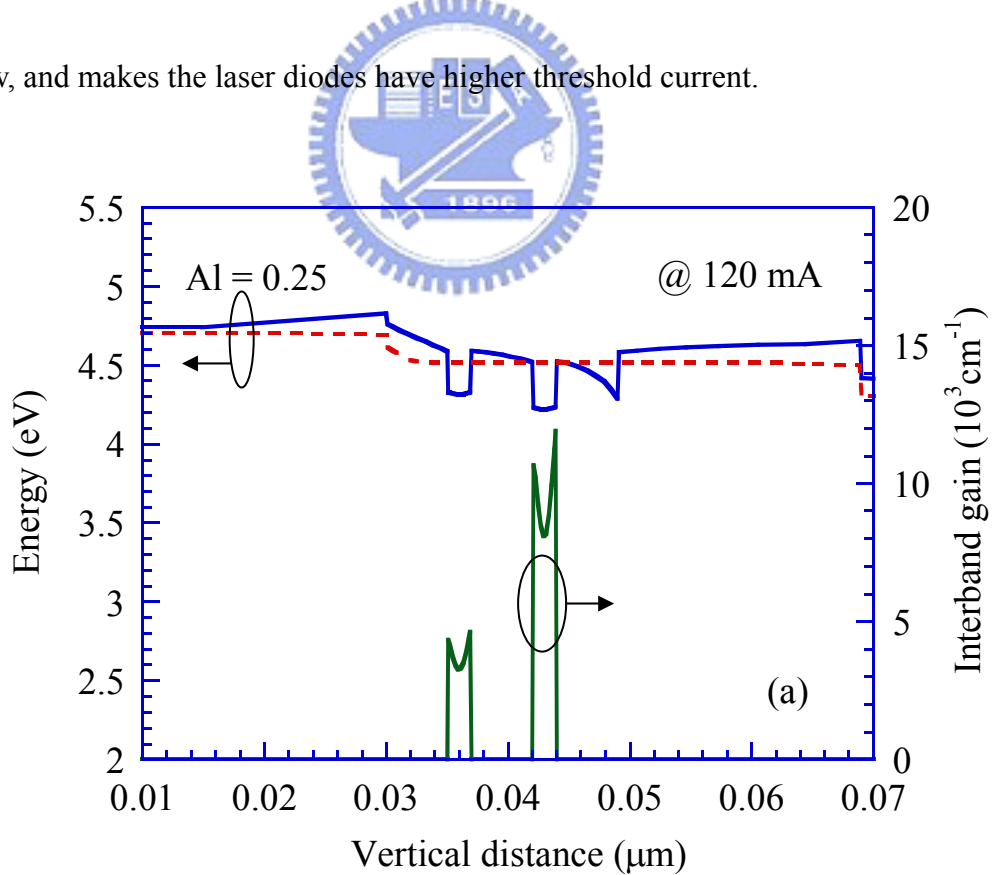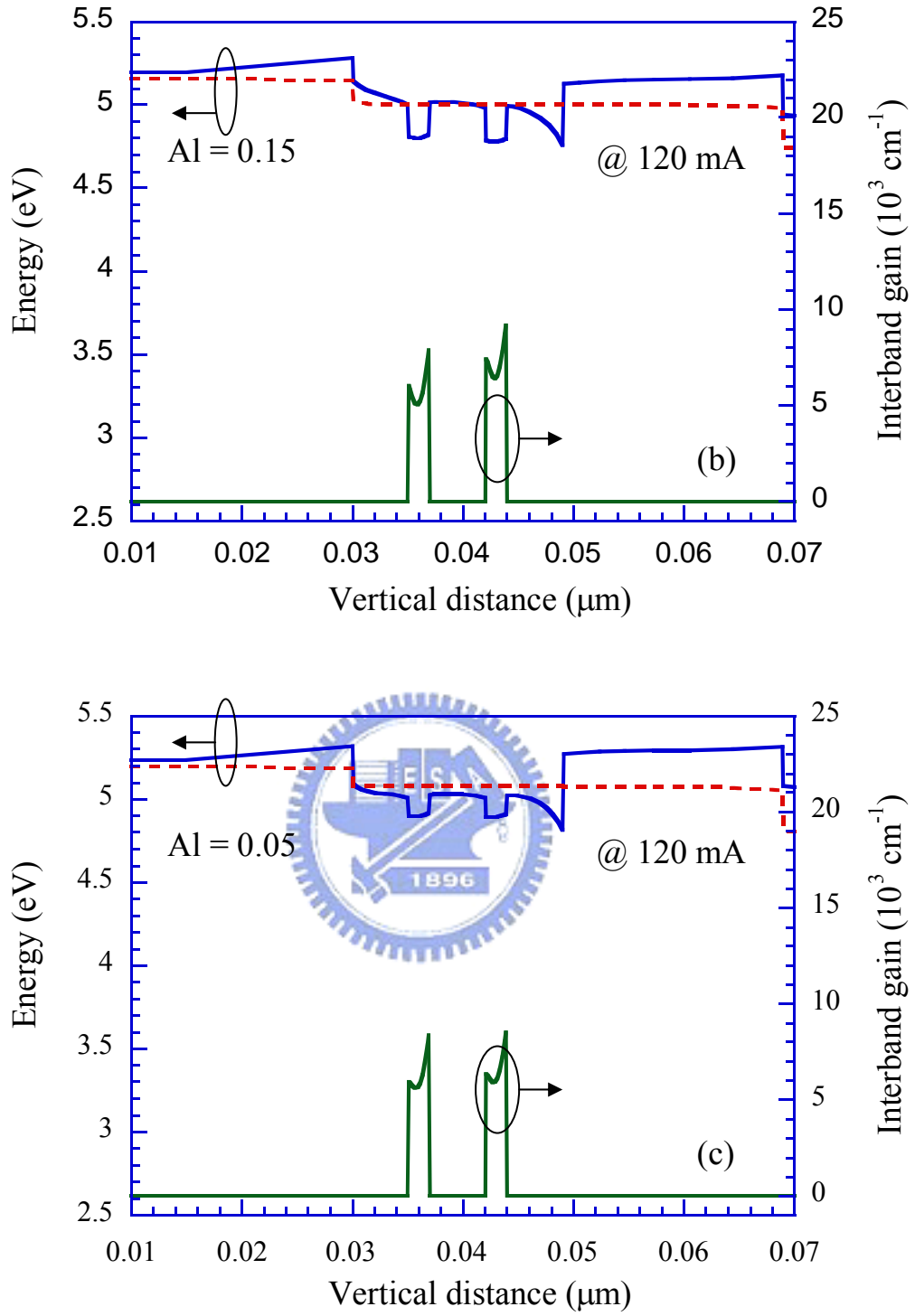
Fig. 4.9 The conduction band and the interband gain in the quantum well at 120 mA injection current for the laser diodes with a $Al_xIn_yGa_{1-x-y}N$ barrier of $x = 0.25$, $x = 0.15$, and $x = 0.05$, respectively

C. Optical Confinement Factor

Except for the effects of electron leakage current and carrier confinement factor, optical confinement factor is also play an important role for the laser threshold properties. As the aluminum composition in the barrier layer increases, the refractive index decreases simultaneously.Fig. 4.10 shows the quantum-well optical confinement factor versus quantum-barrier aluminum composition, and Table. 4.4 shows the refractive index in the barrier layer at 405 nm and the confinement factor Γ values. The optical confinement factor decreases with the increasing aluminum composition in barrier layer due to the smaller difference of refractive index between barrier layer and cladding layer. Therefore, the lower optical confinement factor is also an important role which results in the larger threshold current when the aluminum composition in barrier layer increases. Moreover, the confinement factor can be defined as follow.

$$\Gamma = \frac{\text{active region optical field}}{\text{full region optical field}} \times 100\ \% \tag{4.17}$$
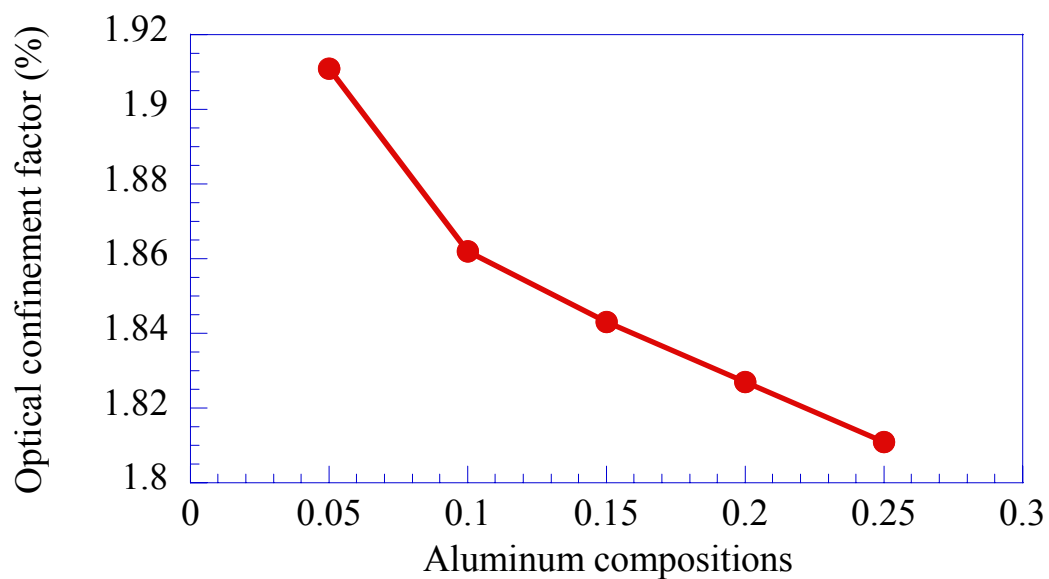
Fig. 4.10 The quantum-well optical confinement factor versus quantum-barrier aluminum composition

Table 4.4 The refractive index in the barrier layer at 405 nm and the confinement factor Γ values

Barrier layer	Index @ 405 nm	Confinement factor Γ
$Al_{025}In_{0.226}GaN$	2.502	1.811 %
$Al_{0.20}In_{0.207}GaN$	2.508	1.827 %
$Al_{0.15}In_{0.188}GaN$	2.514	1.843 %
$Al_{0.10}In_{0.169}GaN$	2.521	1.862 %
$Al_{0.05}In_{0.150}GaN$	2.539	1.911 %

4.6 Summary

We have done the theoretical simulation to investigate the elimination of quantum confine stark effect on the $In_{0.1}Ga_{0.9}N/In_{0.035}Ga_{0.965}N$ and $In_{0.1}Ga_{0.9}N/Al_{0.25}In_{0.226}GaN$ multiple-quantum-well laser performance. The results indicate that the quaternary alloys used in the quantum-barrier layer can eliminate the QCSE and also make the laser diodes have better performance. The threshold current values of $In_{0.1}Ga_{0.9}N/In_{0.035}Ga_{0.965}N$ and $In_{0.1}Ga_{0.9}N/Al_{0.25}In_{0.226}GaN$ MQW LDs are 110.90 mA and 81.41 mA, respectively. However, the performance of the $In_{0.1}Ga_{0.9}N/Al_{0.25}In_{0.226}GaN$ MQW LD should be improved further. Therefore, we optimize the InGaN/AlInGaN MQW LDs utilizing different aluminum and indium compositions in the barrier layer and investigate the internal physical mechanisms. We obtain the InGaN/AlInGaN LDs with an active layer of x = 0.15 and y = 0.188 in the $Al_xIn_yGa_{1-x-y}N$ barrier layey which is found to be the optimized active layer structure due to the competition of these three internal physical mechanisms. The optimal laser diode structure has threshold current value of 41.68 mA. Three different effects cause this result. First, the severe electron leakage current is observed due to the higher barrier aluminum composition. Second, the better carrier confinement in the quantum well is observed due to the higher barrier aluminum composition. Third, the optical confinement factor decreases with the increasing aluminum composition in barrier layer, which leads to the larger threshold current.

Chapter 5 Conclusions

In this thesis, we firstly investigated the performance of GaN/AlGaN laser diodes with different aluminum compositions in barrier layer by LASTIP simulation program. Specifically, the effects of quantum-well number, quantum-barrier aluminum composition, and quantum-well thickness on the device properties are discussed in an attempt to obtain optimal design in the active region. Simulation results suggest that the use of an $Al_xGa_{1-x}N$ barrier/confining layer with an aluminum composition of 10~12 % and two or three quantum wells has better device performance. Higher or lower aluminum compositions in the quantum-barrier layer and more or fewer quantum-well numbers make the GaN/AlGaN MQW lasers have worse device performance. In our analysis, several different effects cause this result, such as electron leakage current, non-uniform carrier distribution, spontaneous and piezoelectric polarization, and optical confinement factor. Furthermore, the simulation results also indicate that the optimal quantum-well thickness is about 3 nm due to the balance of the advantages of a large confinement factor against the disadvantages of significant QCSE.

Second, the investigations of the InGaN/InGaN and the InGaN/AlInGaN MQW laser performance are also numerically studied by LASTIP simulation program. We have successfully demonstrated the elimination of QCSE by utilizing quaternary alloys to replace conventional ternary alloys in the quantum-barrier layer. The results indicate that the new

structure of the laser diode has better performance. The threshold current values of the $In_{0.1}Ga_{0.9}N/In_{0.035}Ga_{0.965}N$ and the $In_{0.1}Ga_{0.9}N/Al_{0.25}In_{0.226}GaN$ MQW LDs are 110.90 mA and 81.41 mA, respectively. However, the performance of the $In_{0.1}Ga_{0.9}N/Al_{0.25}In_{0.226}GaN$ MQW LD should be improved further. Therefore, we optimize the InGaN/AlInGaN MQW LDs utilizing different aluminum and indium compositions in the barrier layer and investigate the internal physical mechanisms. We obtain the InGaN/AlInGaN LDs with an active layer of $x = 0.15$ and y = 0.188 in the $Al_xIn_yGa_{1-x-y}N$ barrier layer which is found to be the optimized active layer structure due to the competition of these three internal physical mechanisms. The optimal threshold current of the InGaN/AlInGaN laser diode is 41.68 mA. Three different effects, electron leakage current, carrier confinement in the quantum well, and optical confinement factor, cause this result.
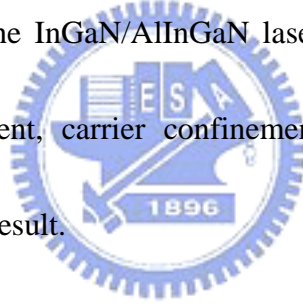
Reference

[1]   R. N. Hall, G. E. Fenner, J. D, Kingsley, T. J. Soltys, and R. O. Carlson, "Coherent Light Emission From GaAs Junctions," *Phys. Rev. Lett.*, vol. 9, no. 9, pp. 366-368 (1962)

[2]   M. I. Nathan, W. P. Dumke, G. Burns, F. H. Dill, and G. J. Lasher, "Stimulated Emission of Radiation from GaAs p-n Junctions," *Appl. Phys. Lett.*, vol. 1, no. 3, pp. 62-64 (1962)

[3]   T. M. Quist, R.H. Rediker, R. J. Keyes, W. E. Krag, B. Lax, A. L. MeWhorter, and H. J. Zeigler, "Semiconductor Maser of GaAs," *Appl. Phys. Lett.*, vol. 1, no.4, pp. 91-92 (1962)

[4]   Nick Holonyak, Jr., and S. F. Bevacqua, "Coherent (Visible) Light Emission From GaAs$_{1-x}$P$_x$ Junctions," *Appl. Phys. Lett.*, vol. 1, no.4, pp. 82-83 (1962)

[5]   H. Kressel, and H. Nelson, "Close-Confinement Gallium Arsenide P-N Junction Lasers with Reduced Optical Loss at Room Temperature," *RCA Rev.*, vol. 30, pp. 106 (1969)

[6]   I. Hayashi, M. B. Panish, P. W. Foy, "A Low-Threshold Room-Temperature Injection Laser," *IEEE. J. Quantum Electron.*, vol. 5, pp. 211-212, (1969)

[7]   Zh. I. Alferov, V.M. Andreev, E.L. Portnoi, and M. K. Trukan, Sov. Phys. Semicond., vol. QE-5,PP. 211 (1969)

[8]   I. Vurgaftman, and J. R. Meyer, "Band Parameters for Nitrogen-Containing Semiconductors," *J. Appl. Phys.*, vol. 94, no. 6, pp. 3675-3696 (2003)

[9]   S. Yoshida, S. Misawa, and S. Gonda, "Improvements on the Electrical and Luminescent Properties of Reactive Molecular Beam Epitaxially Grown GaN Films by Using AlN-Coated Sapphire Substrates," *Appl. Phys. Lett.,* vol. 42, pp 427-429 (1983)

[10]   H. Amano, N. Sawaki, and I. Akasaki, "Metalorganic Vapor Phase Epitaxial Growth of a High Quality GaN Film Using an AlN Buffer Layer," *Appl. Phys. Lett.,* vol. 48, pp 353-355 (1986)

[11]   S. Nakamura, Y. Harada, and M. Seno, "Novel Metalorganic Chemical Vapor Deposition system for GaN Growth," *Appl. Phys. Lett.,* vol. 58, pp 2021-2023 (1991)

[12]   S. Chichibu, T. Azuhata, T. Sota, and S. Nakamura, "Spontaneous emission of localized excitons in InGaN single and multiquantum well structures," *Appl. Phys. Lett.,* vol. 69, no.27, pp 4188-4190 (1996)

[13]   S. Nakamura, M. Senoh, S. I. Nagahama, N. Iwasa, T. Yamada, T. Matsushita, H. Kiyoku, Y. Sugimoto, T. Kozaki, H. Umemoto, M. Sano, and K. Chocho, "InGaN/GaN/AlGaN-Based Laser Diodes with Modulation-Doped Strained-Layer Superlattices," *Jpn. J. Appl. Phys.*, vol. 36, pp. L1568-L1571 (1997)

[14]   H. Amano, M. Krro, K. Hiramatsu, and I. Akasaki, "P-Typed Conduction in Mg-Doped GaN Treated with Low-Energy Electron Beam Irradiation (LEEBI)," *Jpn. J. Appl. Phys.*, vol. 28, no. 12, pp. L2112-L2114 (1989)

[15]   S. Nakamura, T. Mukai, M. Senoh, and N. Iwasa, "Thermal Annealing Effects on P-Type Mg-Doped GaN Films," *Jpn. J. Appl. Phys.*, vol. 31, pp. L139-L142 (1992)

[16]   S. Nakamura, M. Senoh, and T. Mukai, "Highly P-Typed Mg-Doped GaN Films Grown with Buffer Layers," *Jpn. J. Appl. Phys.*, vol. 30, pp. L1708-1711 (1991)

[17]   Y. P. Varshni, "Temperature Dependence of the Energy Gap in Semiconductors," *Physica*, vol. 34, pp. 149-154 (1967)

[18]   S. Strite, M. E. Lin, and H. Morkoc, "Progress and Prospects for GaN and the III-V Nitride Semiconductors," *Thin Solid Films*, vol. 231, pp. 197-210(1993)

[19]   H. P. Maruska, and J. J. Tietjen, "The Preparation and Properties of Vapor-Deposited Single-Crystal-Line GaN," *Appl. Phys. Lett.,* vol. 15, no.10, pp. 327-329 (1969)

[20]   H. Teisseyre, P. Perlin, T. Suski, I. Grzegory, S. Porowski, and J. Jun, A. Pietraszko, T

D. Moustakas, "Temperature Dependence of the Energy Gap in GaN Bulk Single Crystals and Epitaxial Layer," *J. Appl. Phys.*, vol. 76, no.4, pp. 2429-2434 (1994)

[21]　M. O. Manasreh, "Optical Absorption Near the Band Edge in GaN Grown by Metalorganic Chemical-Vapor Deposition," *Phys. Rev. B,* vol. 53, no. 24, pp 16425-16428 (1996)

[22]　B. Monemar, "Fundamental Energy Gap from Photoluminescence Excitation Spectra," *Phys. Rev. B,* vol. 10, no. 2, pp 676-681 (1974)

[23]　J. Petalas, S. Logothetidis, and S. Boultadakis, "Optical and Electronic-Structure Study of Cubic and Hexagonal GaN Thin Films," *Phys. Rev. B,* vol. 52, no. 11, pp 8082-8091 (1995)

[24]　Q. Guo, and A. Yoshida, "Temperature Dependence of Band Gap Change in InN and AlN," *Jpn. J. Appl. Phys.*, vol. 33, pp. 2453-2456 (1194)

[25]　W. M. Yim, E. J. Stofko, P. J. Zenzucchi, J. I. Pankove, M. Ettenberg, and S. L. Gillbert, "Epitaxially Grown AlN and its Optical Band Gap," *J. Appl. Phys.*, vol. 44, no.1, pp. 292-296 (1973)

[26]　P. B. Perry, and R. F. Rutz, "The Optical Absorption Edge of Single-Crystal AlN Prepared by a Close-Space Vapor Process," *Appl. Phys. Lett.,* vol. 33, pp 319-321 (1978)

[27]　T. Matsuoka, H. Okamoto, M. Nakao, H. Harima, and E. Kurimoto, "Optical Bandgap Energy of Wurtzite InN," *Appl. Phys. Lett.,* vol. 81, no. 7, pp 1246-1248 (2002)

[28]　T. Matsuoka, M. Nakao, H. Okamoto, H. Harima, and E. Kurimoto, "Experimental Consideration of Optical Band-Gap Energy of Wurtzite InN," *Jpn. J. Appl. Phys.*, vol. 42, pp. 2288-2290 (2003)

[29]　S. Strite, D. Chandrasekhar, David J. Smith, J. Sariel, H. Chen, N. Teraguchi, and H. Morko," Structural properties of InN films grown on GaAs substrates: observation of the zincblende polytpe," *J. Cryst. Growth,* vol. 127, pp. 204-208 (1993)

[30] S. Yoshida, S. Misawa, and S. Gonda, "Properties of $Al_xGa_{1-x}N$ Films Prepared by Reactive Molecular Beam Epitaxy," *J. Appl. Phys.*, vol. 53, pp. 6844-6848 (1982)

[31] Y. Koide, H. Itoh, M. R. Khan, K. Hiramatu, N. Sawaki, and I. Akasaki, "Energy Band-Gap Bowing Parameter in an $Al_xGa_{1-x}N$ Alloy," *J. Appl. Phys.*, vol. 81, pp. 4540-4543 (1987)

[32] S. R. Lee, A. F. Wright, M. H. Crawford, G. A. Petersen, J. Han, and R. M. Biefeld, "The Band-Gap Bowing of $Al_xGa_{1-x}N$ Alloys," *Appl. Phys. Lett.,* vol. 74, no. 22, pp 3344-3346 (1999)

[33] A. F. Wright, and J. S. Nelson, "Bowing Parameters for Zinc-Blende $Al_{1-x}Ga_xN$ and $Ga_{1-x}In_xN$," *Appl. Phys. Lett.,* vol. 66, pp 3051-3053 (1995)

[34] G. Steude, B. K. Meyer, A. Go¨ldner, A. Hoffmann, F. Bertram, J. Christen, H. Amano, and I. Akasaki, "Optical Investigations of AlGaN on GaN Epitaxial Films," *Appl. Phys. Lett.,* vol. 74, no. 17, pp 2456-2458 (1999)

[35] H. Angerer, D. Brunner, F. Freudenberg, O. Ambacher, M. Stutzmann, R. Ho¨pler, T. Metzger, E. Born, G. Dollinger, A. Bergmaier, S. Karsch, and H. J. Ko¨rner, "Determination of the Al Mole Fraction and the Band Gap Bowing of Epitaxial $Al_xGa_{1-x}N$ Films," *Appl. Phys. Lett.,* vol. 74, pp 1504-1506 (1997)

[36] D. Brunner, H. Angerer, E. Bustarret, F. Freudenberg, R. Ho¨pler, R. Dimitrov, O. Ambacher, and M. Stutzmann, "Optical Constants of Epitaxial AlGaN Films and Their Temperature Dependence," *J. Appl. Phys.*, vol. 82, pp. 5090-5096 (1997)

[37] S. Nakamura, M. Senoh, and T. Mukai, "High-Power InGaN/GaN Double-Heterostructure Violet Light Emitting Diodes," *Appl. Phys. Lett.,* vol. 62, pp 2390-2392 (1993)

[38] S. Nakamura, T. Mukai, and M. Senoh, "High-Brightness InGaN/AIGaN Double-Heterostructure Blue-Green-Light-Emitting Diodes," *J. Appl. Phys.*, vol. 78, pp. 8189-8191(1994)

[39] S. Nakamura, M. Senoh, N. Iwasa, and S. I. Nagahama, "High-Power InGaN Single-Quantum-Well-Structure Blue and Violet Light-Emitting Diodes," *Appl. Phys. Lett.,* vol. 67, pp 1868-1870 (1995)

[40] G. Steude, B. K. Meyer, A. Goldner, A. Hoffmann, F. Bertram, J. Christen, H. Amano, and I. Akasaki,"Optical investigations of AlGaN on GaN epitaxial films," *Appl. Phys. Lett.,* vol. 74, pp. 2456-2458 (1999)

[41] H. Angerer, D. Brunner, F. Freudenberg, O. Ambacher, M. Stutzmann, R. Hopler, T. Metzger, and E. Born, G. Dollinger, A. Bergmaier, S. Karsh, and H. J. Korner,"Determination of the Al mole fraction and the band gap bowing of epitaxial $Al_xGa_{1-x}N$ films," *Appl. Phys. Lett.,* vol. 71, pp. 1504-1506 (1997)

[42] T. Nagatomo, T. Kuboyama, H. Minamino, and O. Omoto, "Properties of $Ga_{1-x}In_xN$ Films Prepared by MOVPE," *Jpn. J. Appl. Phys.,* vol. 28, no.8, pp. L1334-L1336 (1989)

[43] M. Asif Khan, J. W. Yang, G. Simin, R. Gaska,M . S. Shur, H. C. zur Loye, G. Tamulaitis, A. Zukauskas, D. J. Smith, D. Chandrasekhar, and R. Bicknell-Tassius, "Lattice and Energy Band Engineering in AlInGaN/GaN Heterostructures," *Appl. Phys. Lett.,* vol. 76, no. 9, pp 1161-1163 (2000)

[44] I. Vurgaftman, J. R. Meyer, and L. R. Ram-Mohan, "Band Parameters for III–V Compound Semiconductors and Their Alloys," *Appl. Phys. Revt.,* vol. 89, no. 11, pp 5815-5875 (2001)

[45] G. Mat-tin, S. Strite, A. Botchkarev, A. Agarwal, A. Rockett, H. Morkoc, W. R. L. Lambrecht, and B. Segall, "Valence-Band Discontinuity between GaN and AlN Measured by X-Ray Photoemission Spectroscopy," *Appl. Phys. Lett.,* vol. 65, pp 610-612 (1994)

[46] G. Mat-tin, A. Botchkarev, A. Rockett, and H. Morkoc, "Valence-Band Discontinuities of Wurtzite GaN, AlN, and InN Heterojunctions Measured by X-Ray

Photoemission Spectroscopy," *Appl. Phys. Lett.,* vol. 68, pp 2541-2543 (1996)

[47] J. Baur, K. Maier, M. Kunzer, U. Kaufmann, and J. Schneider, "Determination of the GaN/AlN Band Offset via the (-/0) Acceptor Level of Iron," *Appl. Phys. Lett.,* vol. 65, pp 2211-2213 (1994)

[48] J. R. Waldrop, and R. W. Grant, "Measurement of AlN/GaN (0001) Heterojunction Band Offsets by X-Ray Photoemission Spectroscopy," *Appl. Phys. Lett.,* vol. 68, pp 2879-2881 (1996)

[49] S. H. Wei, and A. Zunger, "Valence Band Splittings and Band Offsets of AlN, GaN, and InN," *Appl. Phys. Lett.,* vol. 69, pp 2719-2721 (1996)

[50] S. H. Wei, and A. Zunger, "Calculated Natural Band Offsets of All II–VI and III–V Semiconductors: Chemical Trends and the Role of Cation d Orbitals," *Appl. Phys. Lett.,* vol. 72, no. 16, pp 2011-2013 (1996)

[51] T. F. Kuech, R. T. Collins, D. L. Smith, and C. Mailhiot, "Field-Effect Transistor Structure Based on Strain-Induced Polarization Charges," *J. Appl. Phys.*, vol. 67, pp. 2650-2652 (1990)

[52] J. I. Pankove and T. D. Moustakas, "Gallium Nitride (GaN) Ⅱ-Semiconductors and Semimetals," *Academic Press,* vol. 57 (1999)

[53] G. B. Stringfellow, and M. G. Craford, "High Brightness Light EmittingDiodes: Semiconductors and Semimetals," *Academic Press,* vol. 48 (1997)

[54] J. A. Majewski, M. Stadele, and P. Vogl, "Electronic structure ofbiaxially strained wurtzite crystals GaN, AlN, and InN," *MRS Internet J. Nitride Semicond.,* vol. 1 (1999)

[55] J. H. Edgar, "Properties of Group III Nitrides," *Electronic Materials Information Service* (1994)

[56] K. Shimada, T. Sota, and K. Suzukib, "First-Principles Study on Electronic and Elastic Properties of BN, AlN, and GaN," *J. Appl. Phys.*, vol. 84, no. 9, pp. 4951-4958 (1998)

[57] H. Morkoc, S. Strite, G. B. Gao, M. E. Lin, B. Sverdlov, and M. Burns, "Large-Band-Gap SIC, III-V Nitride, and II-VI ZnSe-Based Semiconductor Device Technologies," *J. Appl. Phys.*, vol. 76, pp. 1363-1398 (1994)

[58] K. Kim, W. R. L. Lambrecht, and B. Segall, "Elastic Constants and Related Properties of Tetrahedrally Bonded BN, AlN, GaN, and InN," *Phys. Rev. B,* vol. 53, no. 24, pp 16310-16326 (1996)

[59] A. F. Wright, and J. S. Nelson, "Explicit Treatment of the Gallium 3D Electrons in GaN Using the Plane-Wave Pseudopotential Method," *Phys. Rev. B,* vol. 50, no. 4, pp 2159-2165 (1994)

[60] D. Vogel, P. Kru¨ger, and J. Pollmann, "Structural and Electronic Properties of Group-III Nitrides," *Phys. Rev. B,* vol. 55, no. 19, pp 12836-12839 (1997)

[61] K. Miwa, and A. Fukumoto, "First-Principles Calculation of the Structural, Electronic, and Vibrational Properties of Gallium and Aluminum Nitride," *Phys. Rev. B,* vol. 48, no. 11, pp 7897-7902 (1993)

[62] G. B. Stringfellow, and M. G. Craford, "High Brightness Light Emitting Diodes: Semiconductors and Semimetals," *Academic Press,* vol. 48 (1997)

[63] T. Mukai, "Recent Progress in Group-III Nitride Light-Emitting Diodes," *IEEE. J. Quantum Electron.*, vol. 8, no. 2, pp. 264-270, (2002)

[64] 史光國編著,現代半導體發光及雷射二極體材料技術,全華科技圖書股份有限公司,民國九十一年。

[65] S. Nakamura, M. Senoh, S. I. Nagahama, N. Iwasa, T. Yamada, T. Matsushita, H. Kiyoku, Y. Sugimoyo, T. Kozaki, H. Umemoto, and K. Chocho, "InGaN/GaN/AlGaN-based laser diodes with modulation-doped strained-layer superlattices grown on an epitaxially laterally overgrown GaN substrate," *Appl. Phys. Lett.,* vol. 72, pp. 211-213 (1998)

[66] S. Nakamura, "InGaN Multiquantum-Well-Structure Laser Diodes with GaN-AlGaN

Modulation-Doped Strained-Layer Superlattices," *J. Selected Topics in QE,* vol. 4, pp. 483-489 (1998)

[67] M. C. Schmidt, K. C. Kim, R. M. Farrell, D. F. Feezell, D. A. Cohen, M. Saito, K. Fujito, J. S. Speck, S. P. Denbaars, and S. Nakamura, "Demonstration of Nonpolar m-plane InGaN/GaN Laser Diodes," *Jpn. J. Appl. Phys.*, vol. 46, pp. L190-L191 (2007)

[68] D. F. Feezell, M. C. Schmidt, R. M. Farrell, K.C. Kim, M. Saito, K. Fujito, D. A. Cohen, J. S. Speck, S. P. Denbaars, and S. Nakamura, "AlGaN-Cladding-Free Nonpolar InGaN/GaN Laser Diodes," *Jpn. J. Appl. Phys.*, vol. 46, pp. L284-L286 (2007)

[69] K. Iga, F. Koyama, and S. Kinoshita, "Surface Emitting Semiconductor Lasers," *IEEE. J. Quantum Electron.*, vol. 24, pp.1845-1855 (1988)

[70] Z.-M. Li, "Physical Models and Numerical Simulation of Modern Semiconductor Lasers," Physics and Simulation of Optoelectronic Devices V; ed. M. Osinski and W. W. Chow; SPIE, vol. 2994, pp. 698-708 (1997)

[71] S.L Chuang, "Efficient Band-Structure Calculations of Strained Quantum Wells," *Phys. Rev. B*, vol.43, pp. 9649-9661 (1991)

[72] Crosslight Software General Description Version 2003.4 Edition 1

[73] S. Kamiyama, K. Iida, T. Kawashima, H. Kasugai, S. Mishima, A. Honshio, Y. Miyake, M. Iwaya, H. Amano, and I. Akasaki, "UV Laser Diode with 350.9-nm-Lasing Wavelength Grown by Hetero-Epitaxial-Lateral Overgrowth Technology," *IEEE J. Select. Topics Quantum Electron.*, vol. 11, pp. 1069-1073 (2005)

[74] J. Li, T. N. Oder, M. L. Nakarmi, J. Y. Lin, and H. X. Jiang, "Optical and Electrical Properties of Mg-Doped P-Type $Al_xGa_{\bar{1}x}N$," *Appl. Phys. Lett.*, vol. 80, pp. 1210-1212 (2002)

[75] G. Franssen, S. Grzanka, R. Czernecki, T. Suski, L. Marona, T. Riemann, J. Christen,

H. Teisseyre, P. Valvin, P. Lefebvre, P. Perlin, M. Leszczyński, and I. Grzegory, "Efficient Radiative Recombination and Potential Profile Fluctuations in Low-Dislocation InGaN/GaN Multiple Quantum Wells on Bulk GaN Substrates," *J. Appl. Phys.*, vol. 97, pp. 103507 (2005)

[76] S. Masui, Y. Matsuyama, T. Yanamoto, T. Kozaki, S. Nagahama, and T. Mukai, "365 nm Ultraviolet Laser Diodes Composed of Quaternary AlInGaN Alloy," *Jpn. J. Appl. Phys.*, vol. 42, pp. L1318-L1320 (2003)

[77] M. Kneissl, D. W. Treat, M. Teepe, N. Miyashita, and N. M. Johnson, "Ultraviolet AlGaN Multiple-Quantum-Well Laser Diodes," *Appl. Phys. Lett.*, vol. 82, pp. 4441-4443 (2003)

[78] J. Edmond, A. Abare, M. Bergman, J. Bharathan, K.L. Bunker, D. Emerson, K. Haberern, J. Ibbetson, M. Leung, P. Russel, and D. Slater, "High Efficiency GaN-Based LEDs and Lasers on SiC," *J. Crystal Growth*, vol. 272, pp. 242-250 (2004)

[79] K. Iida, T. Kawashima, A. Miyazaki, H. Kasugai, S. Mishima, A. Honshio, Y. Miyake, M. Iwaya, S. Kamiyama, H. Amano, and I. Akasaki, "350.9 nm UV Laser Diode Grown on Low-Dislocation-Density AlGaN," *Jpn. J. Appl. Phys.*, vol. 43, pp. L499-L500 (2004)

[80] K. Iida, T. Kawashima, A. Miyazaki, H. Kasugai, S. Mishima, A. Honshio, Y. Miyake, M. Iwaya, S. Kamiyama, H. Amano, and I. Akasaki, "Laser Diode of 350.9 nm Wavelength Grown on Sapphire Substrate by MOVPE," *J. Crystal Growth*, vol. 272, pp. 270-273 (2004)

[81] *LASTIP Version (2005)11*, Burnaby, BC, Canada: Crosslight Software (2005)

[82] W. W. Chow, M. Kneissl, J. E. Northrup, and N. M. Johnson, "Influence of Quantum-Well-Barrier Composition on Gain and Threshold Current in AlGaN Lasers," *Appl. Phys. Lett.*, vol. 90, pp. 101116 (2007)

[83] Y.-K. Kuo and Y.-A. Chang, "Effects of Electronic Current Overflow and Inhomogeneous Carrier Distribution on InGaN Quantum-Well Laser Performance," *IEEE J. Quantum Electron.*, vol. 40, pp. 437-444 (2004)

[84] S. L. Chuang and C. S. Chang, "K·P Method for Strained Wurtzite Semiconductors," *Phys. Rev. B*, vol. 54, pp. 2491-2504 (1996)

[85] S. L. Chuang, "Optical Gain of Strained Wurtzite GaN Quantum-Well Lasers," *IEEE J. Quantum Electron.*, vol. 32, pp. 1791-1799 (1996)

[86] V. Fiorentini, F. Bernardini, and O. Ambacher, "Evidence for Nonlinear Macroscopic Polarization in III-V Nitride Alloy Heterostructures," *Appl. Phys. Lett.*, vol. 80, pp. 1204-1206 (2002)

[87] J. P. Ibbetson, P. T. Fini, K. D. Ness, S. P. DenBaars, J. S. Speck, and U. K. Mishra, "Polarization Effects, Surface States, and the Source of Electrons in AlGaN/GaN Heterostructure Field Effect Transistors," *Appl. Phys. Lett.*, vol. 77, pp. 250-252 (2000)

[88] H. Zhang, E. J. Miller, E. T. Yu, C. Poblenz, and J. S. Speck, "Measurement of Polarization Charge and Conduction-Band Offset at $In_xGa_{1-x}N$ /GaN Heterojunction Interfaces," *Appl. Phys. Lett.*, vol. 84, pp. 4644-4646 (2004)

[89] C. M. Caughey and R. E. Thomas, "Carrier Mobilities in Silicon Empirically Related to Doping and Field," *Proc. IEEE*, vol. 55, pp. 2192-2193 (1967)

[90] T. T. Mnatsakanov, M. E. Levinshtein, L. I. Pomortseva, S. N. Yurkov, G. S. Simin, M. A. Khan, "Carrier Mobility Model for GaN," *Solid State Electron.*, vol. 47, pp. 111-115 (2003)

[91] F. Schwierz, "An Electron Mobility Model for Wurtzite GaN," *Solid State Electron.*, vol. 49, pp. 889-895 (2005)

[92] M. Farahmand, C. Garetto, E. Bellotti, K. F. Brennan, M. Goano, E. Ghillino, G. Ghione, J. D. Albrecht, and P. P. Ruden, "Monte Carlo Simulation of Electron

Transport in the III-Nitride Wurtzite Phase Materials System: Binaries and Ternaries," *IEEE Trans. Electron Devices*, vol. 48, pp. 535-542 (2001)

[93]   Y. K. Kuo, S. H. Yen, J. R. Chen, "Ultraviolet Light-Emitting Diodes," *Nitride Semiconductor Devices: Principles and Simulation*, WILEY-VCH Verlag GmbH & Co. KGaA (2007)

[94]   B. Romero, J. Arias, I. Esquivias, and M. Cada, "Simple Model for Calculating the Ratio of the Carrier Capture and Escape Times in Quantum-Well Lasers," *Appl. Phys. Lett.*, vol. 76, pp. 1504-1506 (2000)

[95]   T. Peng and J. Piprek, "Refractive Index of AlGaInN Alloys," *Electron. Lett.*, vol. 32, pp. 2285-2286, (1996)

[96]   J. Piprek, *Semiconductor Optoelectronic Devices: Introduction to Physics and Simulation*. San Diego, CA: Academic (2003)

[97]   J. Piprek and S. Li, GaN-based Light-Emitting Diodes. In: *Optoelectronic Devices: Advanced Simulation and Analysis*. New York, Springer Verlag (2005)

[98]   Y. K. Kuo, S. H. Yen, and J. R. Chen: Ultraviolet Light-Emitting Diodes. In: *Nitride Semiconductor Devices: Principles and Simulation*. WILEY-VCH Verlag GmbH & Co. KGaA (2007)

[99]   K. Domen, R. Soejima, A. Kuramata, and T. Tanahashi, "Electron Overflow to the AlGaN P-Cladding Layer in InGaN/GaN/AlGaN MQW Laser Diodes," *MRS Internet J. Nitride Semicond. Res.*, vol. 3, no. 2, pp 2-7 (1998)

[100] J. Y. Chang and Y. K. Kuo, "Simulation of Blue InGaN Quantum-Well Lasers," *J. Appl. Phys.*, vol. 93, pp. 4992-4998 (2003)

[101] J. Piprek, R. Farrell, S. DenBaars, and S. Nakamura, "Effects of Built-in Polarization on InGaN-GaN Vertical-Cavity Surface-Emitting Lasers," *IEEE Photon. Technol. Lett.*, vol. 18, pp. 7-9 (2006)

[102] S.-N. Lee, S. Y. Cho, H. Y. Ryu, J. K. Son, H. S. Paek, T. Sakong, T. Jang, K. K. Choi,

K. H. Ha, M. H. Yang, O. H. Nam, Y. Park, and E. Yoon, "High-Power GaN-Based Blue-Violet Laser Diodes with AlGaN/GaN Multiquantum Barriers," *Appl. Phys. Lett.*, vol. 88, pp. 111101,(2006)

[103] J. Piprek, P. Abraham, and J. E. Bowers, "Carrier Nonuniformity Effects on the Internal Efficiency of Multiquantum-Well Lasers," *Appl. Phys. Lett.*, vol. 74, pp. 489-491 (1999)

[104] J. D. Heber, C. Gmachl, H. M. Ng, and A. Y. Cho, "Comparative Study of Ultrafast Intersubband Electron Scattering Times at ~1.55 m Wavelength in GaN/AlGaN Heterostructures," *Appl. Phys. Lett.*, vol. 81, pp. 1237-1239 (2002)

[105] C.-K. Sun, S. Keller, T.-L. Chiu, G. Wang, M. S. Minsky, J. E. Bowers, and S. P. Denbaars, "Well-Width Dependent Studies of InGaÑGaN Single-Quantum Wells Using Time-Resolved Photoluminescence Techniques," *IEEE J. Select. Topics Quantum Electron.*, vol. 3, pp. 731-737 (1997)

[106] E. Berkowicz, D. Gershoni, G. Bahir, E. Lakin, D. Shilo, E. Zolotoyabko, A. C. Abare, S. P. Denbaars, and L. A. Coldren, "Measured and Calculated Radiative Lifetime and Optical Absorption of $In_xGa_{1-x}N$/GaN Quantum Structures," *Phys. Rev. B*, vol. 61, pp. 10994-11008 (2000)

[107] P. Waltereit, O. Brandt, M. Ramsteiner, R. Uecker, P. Reiche, and K. H. Ploog, "Growth of *M*-plane GaN($1\bar{1}00$) on γ-LiAlO$_2$(100)," *J. Crys. Grow.*, vol. 218, pp.143-147 (2000)

[108] M. D. Craven, S. H. Lim, F. Wu, J. S. Speck, and S. P. DenBaars, "Structural Characterization of Nonpolar ($11\bar{2}0$) a-Plane GaN Thin Films Grown on ($1\bar{1}0\,2$) γ-plane Sapphire," *Appl. Phys. Lett.*, vol. 81, pp. 469-471 (2002)

[109] S. Ko, T. C. Lu, T. C. Wang, M. H. Lo, J. R. Chen, R. C. Gao, H. C. Kuo, and S. C. Wang, "Optical Characteristics of a-Plane InGaN/GaN Multiple Quantum Wells with

Different Well Widths," *Appl. Phys. Lett.*, vol. 90, 181122 (2007)

[110] M. C. Schmidt, K. C. Kim, R. M. Farrell, D. F. Feezell, D. A. Cohen, M. Saito, K. Fujito, J. S. Speck, S. P.Denbaars, and S. Nakamura, "Demonstration of Nonpolar m-Plane InGaN/GaN Laser Diodes," *Jpn. J. Appl. Phys.*, vol. 46, pp. L190 (2007)

[111] K. Okamoto, H. Ohta, S. F. Chichibu, J. Ichihara, and H. Takasu, "Continuous-Wave Operation of m-Plane InGaN Multiple Quantum Well Laser Diodes," *Jpn. J. Appl. Phys.*, vol. 46, pp. L187 (2007)

[112] M. E. Aumer, S. F. LeBoeuf, and S. M. Bedairb, "Effects of Tensile and Compressive Strain on the Luminescence Properties of AlInGaN/InGaN Quantum Well Structures," *Appl. Phys. Lett.*, vol. 77, pp. 821-823 (2000)

[113] W. C. Lai, S. J. Chang, M. Yokoyam, J. K. Sheu, and J. F. Chen, "InGaN–AlInGaN Multiquantum-Well LEDs," *IEEE Photon. Technol. Lett.*, vol. 13, pp. 559-561 (2001)

[114] J. Lee, P. G. Eliseev, M. Osin´ski,D. S. Lee, D. I. Florescu, S. Guo, and M. Pophristic, "InGaN-Based Ultraviolet Emitting Heterostructures with Quaternary AlInGaN Barriers," *IEEE J. Sel. Top. Quantum. Electron.*, vol 9, pp. 1239-1245 (2003)

[115] S. H. Baek, J. O. Kim, M. K. Kwon, I. K. Park, S. I. Na, J. Y. Kim, B. Kim, and S. J. Park, "Enhanced Carrier Confinement in AlInGaN–InGaN Quantum Wells in Near Ultraviolet Light-Emitting Diodes," *IEEE Photon. Technol. Lett.*, vol 18, pp. 1276-1278 (2006)

[116] J. Minch, S. H. Park, T. Keating, and S. L. Chuang, "Theory and Experiment of $In_{1-x}Ga_xAs_yP_{1-y}$ and $In_{1-x-y}Ga_xAl_yAs$ Long-Wavelength Strained Quantum-Well Lasers," *IEEE J. Quantum Electron.*, vol 35, pp. 771-782 (1999)

[117] I. Vurgaftman, J. R. Meyer, and L. R. Ram-Mohan, "Band Parameters for III–V Compound Semiconductors and their Alloys," *J. Appl. Phys.*, vol 89, pp. 5815-5875 (2001)

[118] I. Vurgaftman and J. R. Meyer, "Band Parameters for Nitrogen-Containing

Semiconductors," *J. Appl. Phys.*, vol 94, pp. 3675-3696 (2003)

[119] V. Fiorentini, F. Bernardini, and O. Ambacher, "Evidence for Nonlinear Macroscopic Polarization in III–V Nitride Alloy Heterostructures," *Appl. Phys. Lett.*, vol 80, pp. 1204-1206 (2002)

[120] O. Ambacher, B. Foutz, J. Smart, J. R. Shealy, N. G. Weimann, K. Chu, M. Murphy, A. J. Sierakowski, W. J. Schaff, L. F. Eastman, R. Dimitrov, A. Mitchell, and M. Stutzmann, "Two Dimensional Electron Gases Induced by Spontaneous and Piezoelectric Polarization in Undoped and Doped AlGaN/GaN Heterostructures," *J. Appl. Phys.*, vol 87, pp. 334-344 (2000)

[121] J. P. Ibbetson, P. T. Fini, K. D. Ness, S. P. DenBaars, J. S. Speck, and U. K. Mishrab, "Polarization Effects, Surface States, and the Source of Electrons in AlGaN/GaN Heterostructure Field Effect Transistors," *Appl. Phys. Lett.*, vol 77, pp. 250-252 (2000)

[122] S. F. Chichibu, A. C. Abare, M. S. Minsky, S. Keller, S. B. Fleischer, J. E. Bowers, E. Hu, U. K. Mishra, L. A. Coldren, S. P. DenBaars, and T. Sota, "Effective Band Gap Inhomogeneity and Piezoelectric Field in InGaN/GaN Multiquantum Well Structures," *Appl. Phys. Lett.*, vol 73, pp. 2006-2008 (1998)

[123] H. Zhang, E. J. Miller, E. T. Yua, C. Poblenz, and J. S. Speck, "Measurement of Polarization Charge and Conduction-Band Offset at $In_xGa_{1-x}N$/GaN Heterojunction Interfaces," *Appl. Phys. Lett.*, vol 84, pp. 4644-4646 (2004)

[124] F. Renner, P. Kiesel, G. H. Do¨ hler, M. Kneissl, C. G. Van de Walle, and N.M. Johnson, "Quantitative Analysis of the Polarization Fields and Absorption Changes in InGaN/GaN Quantum Wells with Electroabsorption Spectroscopy," *Appl. Phys. Lett.*, vol 81, pp. 490-492 (2002)